University of Alberta

Argon-Assisted Glancing Angle Deposition

by

Jason Brian Sorge

A thesis submitted to the Faculty of Graduate Studies and Research
in partial fulfillment of the requirements for the degree of

Doctor of Philosophy

in

Microsystems and Nanodevices

Department of Electrical and Computer Engineering

Fall 2012

Edmonton, Alberta

To my wife Crystal, and my parents Brian and Lorrie.

Abstract

Glancing angle deposition (GLAD) is a physical vapour deposition (PVD) technique capable of fabricating highly porous thin films with controllable film morphology on the 10 nm length scale. The GLAD process is flexible and may be used on virtually any PVD-compatible material. This makes GLAD a useful technique in many applications including photovoltaics, humidity sensing, and photonic devices. Conventional, dense films grown at normal incidence concurrent with ion or energetic neutral bombardment have been reported to have higher film density than unbombarded films. In a similar sense, highly porous GLAD films grown with concurrent bombardment should generate films with new interesting properties and extend the versatility of the GLAD process.

The research presented in this thesis investigates the use of energetic neutral bombardment during GLAD film growth to produce new film morphologies. Here, with increasing bombardment, the column tilt increases, film density increases, and specific surface area decreases. A film simultaneously exhibiting high column tilt angle and film density is enabled by incorporating bombardment concurrent with GLAD film growth. This in turn results in films with larger principal refractive indices, but a smaller normalized in-

plane birefringence. Bombarded films were also found to be compatible with the phisweep process which helps decouple the column tilt angle from film density. Characterization of the bombardment-assisted growth process indicates that both sputtering and bombardment-induced diffusion play a role in the modification of film morphology.

The film property modifications which arise as a result of bombardment-assisted growth lead to device improvements in a number of applications. Bombardment was used to fabricate square spiral photonic crystal structures with increased column tilt which bear a closer resemblance to optimized simulated structures than conventionally-grown GLAD films. The increase in column tilt angle and film density were found to be beneficial in the fabrication of circular polarization filters, where bombarded films were found to exhibit larger selective circular behaviour than in unbombarded films. The morphology modification was also found to be beneficial in humidity sensing applications where the bombarded films demonstrated an increase in the capacitive response.

Acknowledgements

Thank you to Dr. Michael Brett for your supportive supervision and for equipping the lab with the resources and personnel which allowed me to remain focused on my research. I would also like to thank Michael Taschuk who could always provide day-to-day guidance and direction. Also, thank you to Jeremy Sit, Michael Fleischauer, Nicole Beckers, and Zhen Wang for their insightful questions and suggestions during our focus group meetings. The advice that all of you provided throughout my studies have significantly strengthened my research and is very much appreciated.

Thank you to Nick Wakefield, Andy van Popta, Mark Summers, and Joshua LaForge for your contributions to my research. Your assistance with equipment and general advice helped tremendously. Thank you to Mark Summers for providing me with the patterned substrates used in Chapter 4, and to Josh Siewert for squeezing in emergency samples into his SEM time at NINT. I would also like to thank George Braybrook and De-Ann Rollings for providing me with many of the SEM images used in this thesis.

Thanks to Allan Beaudry, Louis Bezuidenhout, Graeme Dice, Sumudu Fernando, James Gospodyn, Doug Gish, Ken Harris, Matthew Hawkeye, Graham Hunt, Steven Jim, Katie Krause, Jonathan Kwan, Abeed Lalany, Vik-

tor Leontyev, John Steele, Michael Thomas, Shufen Tsoi, Ryan Tucker, Jaron van Dijken for the discussions which were often productive, sometimes not so productive, but always appreciated. Also, thank you to Ben Bathgate for providing guidance and troubleshooting issues with the equipment in the lab.

I would like to acknowledge funding from the Natural Sciences and Engineering Research Council of Canada, Alberta Innovates Technology Futures, and the University of Alberta.

Finally, thank you to my wife and family for their amazing support.

Contents

List of Tables

List of Figures

Chapter 1

Introduction

1.1 Introduction

Over the last decade, annual global funding of nanotechnology has increased ten-fold [1]. Today, annual government spending on nanotechnology research and development internationally is approximately $10B and it is estimated that this number will grow by 20% in the next three years. By 2014, total government investment is expected to reach $100B. When corporate research and private funding are taken into account, global investment into nanotechnology research and development is estimated to approach $250B. These trends indicate a substantial, sustained financial commitment which provide vast opportunities for research and commercial development in the nanotechnology sector.

One of the central nanotechnological processes is the deposition of thin films. Modern thin film technology began more than a century ago, when physical vapour deposition (PVD) processes such as sputtering and thermal evaporation were invented [2, 3]. Since then, chemical vapour deposition

(CVD) processes have come online which improve the coverage through conformal coatings over substrate topography. Today, the state of the art in thin film technology provides atomic-level control over the thin film composition. This degree of control can be achieved with processes such as atomic layer deposition and molecular beam epitaxy.

Thin film technology can tailor material properties such as density, uniformity, adhesion, and durability for specific applications. These include optical interference filters, thermally insulating coatings, microelectronic devices, and chemical sensors. The usefulness of thin film technology in these applications is largely due to the significant amount of research focused on the understanding and improvement of existing fabrication processes and film growth mechanics. Thin film research has had a traditional focus on optimizing thin film properties by varying the deposition conditions. An alternative method is to tailor film properties via nanostructure.

Glancing angle deposition (GLAD) is a thin film deposition process that provides control over film nanostructure. It is a PVD technique that is based on deposition onto tilted substrates such that incident vapour flux arrives at the substrate at an angle α. It has been long known that thin film deposition onto tilted substrates leads to films with morphologies that differ from films that are deposited at normal incidence [4, 5]. The GLAD process, and its ability to provide control over film nanostructure, has been shown to be useful in a variety of applications [6–11]. For instance, by careful design and fabrication of the film structure, the refractive index can be tailored anywhere between bulk values and close to unity. However, there are still limitations on the film morphologies achievable through the GLAD process.

This thesis describes research on improving the versatility of the GLAD technique through energetic neutral argon bombardment during deposition. Discussion will begin with an overview of thin film deposition and describe the GLAD technique in detail, with an emphasis on morphological modification and control. The main characterization techniques used during this thesis research will then be briefly outlined. The second chapter will focus specifically on the argon-assisted GLAD deposition process with characterizations of the the system geometry and argon source. This chapter will also investigate the mechanisms inherent in the Ar-assisted GLAD deposition process which lead to additional film morphology modification possibilities. The film property modifications which arise as a result of the interplay between oblique angle film deposition and argon bombardment are discussed in chapter three. The remaining discussions after chapter three survey applications where these novel Ar-assisted structures show the most promise. The thesis concludes with a short summary and recommendations for future research.

1.2 Structured Thin Films and GLAD

The chamber pressure and source excitation requirements of GLAD can be satisfied for many PVD techniques, including thermal evaporation, electron-beam evaporation, sputtering, and pulsed laser deposition. These PVD techniques can be characterized by the method in which the source material flux is generated. In evaporative techniques, the source material is heated to the point where it either melts or sublimates. Evaporative techniques can be further broken down into how the source material is heated. The material can either be heated by passing a current through a wire that is in contact with the source material (thermal evaporation), by focusing an electron beam on

it (electron-beam evaporation), or by focusing a high intensity laser beam onto the source material (pulsed laser deposition). Sputtering is another PVD technique, but instead of heating, the process uses momentum transfer of energized ions to create source material flux. GLAD has been shown to be compatible with all of these PVD processes [12–14].

During evaporative processes, a portion of the source material is energized to generate a net material flux away from the material source inside a chamber held at vacuum pressures. When the temperature of the source material is sufficiently high, the flux leaving the material source becomes significant. At high chamber pressure, collision events between source material flux and ambient gas scatter the flux which decreases the deposition at the target substrate. At lower chamber pressures, scattering events can be reduced to the point where it is improbable that escaping source material molecules undergo collisions with ambient gas before reaching the chamber wall or substrate. An additional reason to use low chamber pressure is to minimize film contamination by background gases. The deposited film is formed when the material flux that collects on the substrate in its solid form.

1.2.1 Nucleation and Early Growth

In vapour-based PVD processes, film growth initiates with the condensation of vapour atoms in a nucleation process on the substrate surface. When an atom arrives on the substrate surface, it becomes an adatom and begins to diffuse on that surface until one of three events occurs: the adatom desorbs and escapes from the substrate surface, the adatom creates a nucleus on the substrate surface, or the adatom joins an already existing nucleus. Nucleus stability is determined by its size and the energetics of the system. Below a critical

nucleus size, it is more favourable for adatoms to re-evaporate. Once this critical nucleus size is reached, it becomes more favourable for the adatoms to remain attached to the nucleus. Once this occurs, the nuclei quickly grow and become the dominant locations for subsequent film growth.

The nucleation process occurs as one of three growth modes that are dependent on the substrate-adatom affinity [15–18]. When the binding between adatoms is stronger than that between an adatom and the substrate, the nuclei form 3D clusters. This is called Volmer-Weber or island growth. If the adatoms preferentially bind to the substrate rather than to each other, the nuclei more closely resemble 2D layers. This is known as Frank-van der Merwe or layer growth. The third possibility is a combination of the other two, which initiates as layer growth with subsequent islanding. This is called Stranski-Krastanov or layer plus island growth. The characteristic nucleation in most GLAD processes is Volmer-Weber growth.

1.2.2 Columnar Growth and Structure Zone Models

After the initial nucleation stage of film growth, the deposition process continues as incident vapour atoms deposit on the film surface and the nuclei begin to form columnar structures. The properties of these newly forming columns are largely determined by the available potential for surface diffusion, which is mainly governed by the substrate temperature T_S. Movchan and Demchishin first explained the effects of T_S with the introduction of a film growth model called the structure zone model (SZM) [19]. Here three distinct structural regimes were observed with transition substrate temperatures T_1 and T_2. These transition temperatures were found to be independent of the source material and occurred at $T_1/T_m \approx 0.3$ and $T_2/T_m \approx 0.5$, where

T_m is the source material melting point. In the first zone, where $T_S \leq T_1$, the limited adatom diffusion results in a film microstructure consisting of tapered columns separated by voids. In the second regime, where $T_1 \leq T_S \leq T_2$, the surface diffusion is larger, which leads to an increase in the column diameter and a reduction in column tapering. The third regime, where $T_2 \leq T_S$, there is enough available energy for significant bulk diffusion to occur, which leads to crystallization of the deposited material. Here, morphology consists of densely packed crystalline grains with minimal void space. While other film growth models have since been reported with additional zones and processing parameters such as chamber pressure [20–22], the basic three-zone model provides basic insight into understanding the GLAD process. Film architecture control by GLAD is most effective in the first temperature zone, where $T_S \leq T_1$.

1.2.3 Controlling Columnar Structure: GLAD

The GLAD process is capable of producing highly porous thin films with controllable film microstructure by combining self-shadowing and limited adatom diffusion. To achieve this, films grown with GLAD generally involve Volmer-Weber nucleation. The initial nuclei on the substrate create microscopic topography that casts shadows on the substrate at oblique angles of incidence. When this is combined with the directional nature of source material vapour in PVD processes, at oblique incidence these nuclei prevent deposition in the substrate regions directly behind them. This shadowing restricts subsequent film growth to the nuclei created in the initial film growth. Surface diffusion is a competing process of shadowing. This diffusion is minimized by enforcing low substrate temperatures such that T_S falls into the

first zone of Movchan and Demchishin's SZM.

Enforcing and controlling the shadowing effect with the GLAD process allows the inherent columnar structure to be tailored for specific applications. At non-normal deposition angles, α, ($\alpha \neq 0$), the developing columns grow inclined towards the vapour source at an angle β measured from substrate normal, where $\beta < \alpha$ [23–25]. These columns will continue to grow inclined towards the source indefinitely until the location of the source is changed. This is accomplished in a GLAD process by rotating the substrate in two different ways. First, changing the deposition angle α by tilting the substrate, changes the magnitude of the shadowing effect that governs film porosity can be controlled. Tait et al. derived an expression relating α to the normalized film density ρ by assuming hemispherical surface features, no material dependent properties, and limited surface diffusion [24].

$$\rho = \frac{2\cos\alpha}{1+\cos\alpha}. \tag{1.1}$$

This relation indicates that the film density can be controlled by the deposition angle. At low angles, the film will be quite dense and will have properties similar to a solid film. As the deposition angle is increased, the film becomes more porous with the characteristic isolated columns in GLAD films emerging at high angles.

The second degree of rotational control, φ, involves rotating the substrate about its normal axis, which is responsible for determining the column growth direction. A typical GLAD setup is shown in Fig. 1.1. The two rotation parameters are dynamically computer-controlled throughout the course of the

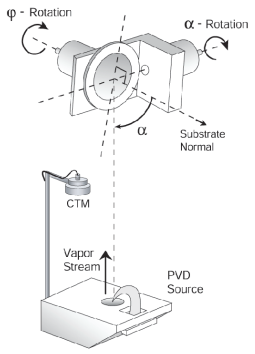

Figure 1.1. *The GLAD apparatus as it is typically implemented in a PVD system with deposition angle α and substrate rotation angle φ defined. Reproduced with permission from Steele* et al. *[26] ©2006 IEEE.*

deposition with feedback from a quartz crystal microbalance (QCM). This allows films to be produced with a wide variety of densities and shapes just by changing the substrate rotation algorithms. If a substrate is not rotated, the tilted columns will form as previously described. If the substrate is φ-rotated abruptly by π radians at set intervals, the column growth direction will be alternated and a zig-zag or chevronic structure will result. If the substrate is slowly φ-rotated at a constant rate, the film will adopt a helical structure. If this φ-rotation is increased relative to the film growth rate, the helical pitch will decrease. With a sufficient increase in φ-rotation, such that the helical pitch decreases to the same size as the column diameter, the helical columns will degenerate into vertical posts that grow in the substrate normal direction. These structures, shown in Fig. 1.2, are the basic building blocks found in all GLAD films.

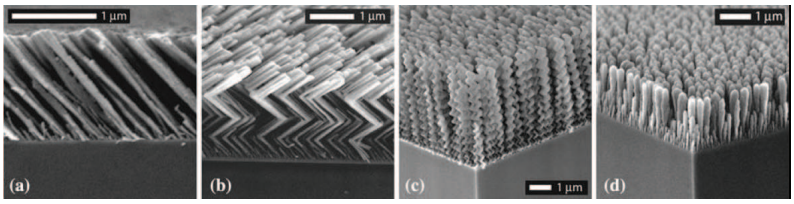

Figure 1.2. *SEM images of (a) slanted post, (b) chevron, (c) helical, and (d) vertical post GLAD films. Reproduced with permission from Steele and Brett [27].*

1.2.4 Advanced Substrate Motion

It has just been shown that the use of different simple substrate motion algorithms, such as no rotation or constant rotation, can have a large impact on film structure. However, further control over some film structures can be obtained from additional refinement of the substrate motion algorithm. One such refinement, which will be used extensively throughout the studies presented in this thesis, is the phisweep process [28]. The phisweep process uses periodic, symmetric oscillations in substrate φ rotation to fabricate slanted post structures. This substrate motion introduces shadowing outside of the traditional deposition plane of a slanted post film which minimizes column broadening. This effectively decouples the column growth direction from the flux arrival direction and can eliminate column competition and extinction [28], as well as provide optimal substrate shadowing conditions for growth on tetragonally patterned substrates [29]. This can be useful in photonic crystal and microfluidics applications [29,30].

The parameters which define the phisweep control algorithm are the offset sweep angle γ, and the dwell time at each of the rotation extremes corresponding to a characteristic film thickness, referred to as the sweep pitch. The sweep angle γ is defined as the angle between the sweep extreme and

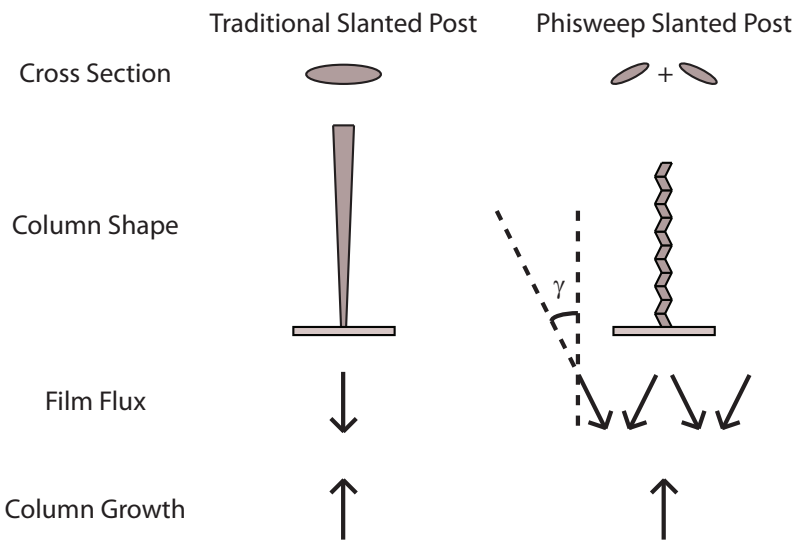

Figure 1.3. *Illustration comparing traditional and phisweep slanted post growth. In both cases, column growth direction is inclined towards the viewer. Details on phisweep column tilt angle are presented in Chapter 3.*

the central column growth axis, or as half of the full sweep between outer extremes. A sweep angle of $\gamma = 0°$ is simply a stationary substrate which corresponds to traditional slanted post growth. The use of the phisweep algorithm results in the slanted post structures being comprised of many smaller segments, rather than one continuous slanted arm, and the resulting overall column tilt will be a combination of the two fundamental phisweep column segments. As a result, as γ is increased, the resulting columnar growth will become more vertical. The basic principle of phisweep is illustrated in Fig. 1.3.

In the extreme limit where $\gamma = 90°$, vertical post films are formed. This algorithm is commonly referred to as serial bi-deposition and is used in optical applications [31–33]. The serial bi-deposition process is important in optical applications because it maximizes columnar anisotropy by preserving the

anisotropic broadening while eliminating competing effects from column tilt.

1.2.5 Ion-Assisted Deposition

In addition to the use of deposition angle and substrate rotation in modifying film growth, the use of ion bombardment has also been implemented. The first studies on ion beam deposition and ion beam assisted deposition (IBAD) were in the fabrication of diamondlike carbon coatings.

Diamondlike carbon coatings contain a large number of characteristics similar to carbon in the diamond form [34], which can all be achieved without requiring single crystal carbon. These include transparency, index of refraction greater than 2.0, electrically insulating, ability to scratch glass, resistance to hydrofluoric acid for long periods of time, at least partially crystalline and with a lattice constant similar to diamond, and a dielectric constant between about 8 and 14 (diamond is 16.5). Most commonly, diamondlike carbon coatings are used to reduce abrasive wear and are used for such purposes in tools and racing engines.

Ion beam deposition uses an accelerated ion beam of the deposition material to provide the required energy for film nucleation and growth [34]. In this deposition technique, the energy of the arriving ions is controlled through the substrate potential, allowing for high energies at low deposition pressures to be achieved. This method of deposition has been used to fabricate epitaxial silicon and carbon films on single-crystal silicon substrates [34, 35]. For example, diamondlike carbon films were fabricated at a substrate potential of $-40\ \mathrm{V}$ and a deposition rate of $5\ \mathrm{nm/s}$. One early study on the ion plating method aimed to determine why superior diamondlike coatings are

achievable with an ion plating process as opposed to a traditional vacuum deposition process [36]. Ion plating refers to a deposition process where the deposition material is evaporated in the presence of a plasma in a vacuum chamber at high pressure (approximately 25×10^{-3} Torr) and is collected on a negatively biased substrate [36]. It was found that the ambient gas present in the chamber during deposition is much more detrimental in a traditional vacuum deposition process because of the lower energy of the incident material flux. Three reasons for this were given. First, collisions between the energetic vapourized atoms and the ambient gas will reduce the average energy of the deposited atoms, which results in a reduction in film quality. Second, the presence of gas contamination on the surface limits film adhesion and surface diffusion. Third is the fact that the presence of excess ambient gas increases the collision rate between ambient gas atoms and deposition atoms which can result in the agglomeration of deposition material before arrival at the substrate. This third effect has the most serious impact on film quality. The use of high vacuum and ion plating during deposition can mostly eliminate these problems. The use of high vacuum reduces the rate of particle collisions and surface contamination. The use of ion plating increases the deposition material energy which improves surface diffusion. Finally, by implementing a negatively biased substrate during the ion plating process, the deposition of agglomerates can be eliminated since these neutral agglomerates become negatively charged in the plasma and get repelled by the negatively biased substrate.

In addition to ion beam deposition, ion beam assisted deposition has been used to fabricate diamondlike carbon coatings [37]. IBAD differs from ion beam deposition in that the functions of ion beam generation and material

flux generation are separate. This film material source can be any type of physical vapour deposition source [37–47], and an ion gun is used to generate an ion beam. With this separation of components, IBAD can achieve a much higher deposition rate and produce films over a much larger area than with ion beam deposition because there is no need to produce ions of the deposition material. IBAD improves diamondlike carbon film quality by providing extra kinetic energy for optimal surface diffusion while preferentially sputtering amorphous graphitic domains [35].

Other applications have also been developed with IBAD. Zhou *et al.* have shown that IBAD is useful in producing surface coatings on hard drive head sliders to reduce friction between the head and platter during operation [48]. Here it was found that amorphous carbon nitride coatings exhibited superior performance over sliders with sputtered carbon, titanium nitride, and boron nitride coatings. Optical coating applications have also been investigated using IBAD. Studies on magnesium fluoride have reported improvements in adhesion on glass substrates, as well as reduction in film stress and crystallite size when IBAD is used [49]. Studies on IBAD silicon film growth have shown control over stoichiometry [50]. Here, nitrogen bombardment was used to control film stoichiometry. By controlling the ratio of nitrogen ion flux to silicon film flux, the film composition was varied between pure silicon and stoichiometric silicon nitride. This was used to fabricate a silicon/silicon nitride near infrared rugate filter. IBAD has also been reported to be used in the industrial production of electric shaver heads [51]. Here IBAD is used to coat the cutting edge of shaving blades with titanium nitride and titanium carbon nitride to improve corrosion resistance.

The incorporation of ion bombardment to act as, or assist during deposition has been shown to modify numerous film properties which improve the effectiveness of thin films in many applications. While there have been many studies on ion-assisted deposition and potential applications, the vast majority have been on dense films grown at normal incidence and relatively few on highly porous films grown at high deposition angles. The study of bombardment during porous film growth will be the focus of this thesis. However, rather than ions, the bombarding species is energetic neutral argon and the process will be referred to as the argon-assisted or Ar-assisted process. In this thesis, the basic Ar-assisted process, its implementation in these studies, and the mechanisms responsible for property modification in porous Ar-assisted films will be discussed. In addition, significant focus will be placed on the various film property modifications observed in the fabrication of porous Ar-assisted films and how these modifications show potential in many applications. The thesis will then conclude with a summary of significant results and potential areas of future study.

1.3 Characterization

To measure film properties in these studies, a number of standard thin film characterization techniques are used. The following section will briefly outline these techniques.

1.3.1 Scanning Electron Microscopy

Scanning electron microscopy (SEM) is one of the most commonly used tools for characterizing GLAD films. SEM images are generated by rastering a focused electron beam across a film and collecting and detecting secondary

electrons which are generated from the interaction between the electron beam and the sample. The amount of secondary electrons that are generated and detected depends on the topography of the sample. When the rate of secondary electron generation is mapped to the primary electron beam location and recorded as an intensity plot, an image is generated which represents the structure and topography of the sample. This makes SEM imaging a useful method for measuring properties such as film thickness, column tilt angle, column width, and column spacing.

For these studies, the SEM is most commonly used for measuring film thickness and column tilt angle. Film thickness was measured from the SEM images by either taking a single measurement, or by averaging a few measurements from the images. Column tilt measurements were also extracted from the SEM images, but were taken as an average of ten measurements. The error in the column tilt measurements was taken as the standard deviation of the mean.

1.3.2 Variable Angle Spectroscopic Ellipsometry

In nearly all obliquely deposited thin films, the tilted columns contain a structural anisotropy, which arises from an anisotropy in the vapour flux shadowing. This column broadening makes obliquely deposited films ideal candidates for applications that require dichroic or birefringent material. In the most general case, obliquely deposited films are biaxial media. This requires that the dielectric constant ϵ be expressed as a rank-2 tensor with principle values ϵ_{11}, ϵ_{22}, and ϵ_{33} to account for the structural anisotropy. These principle values are defined by the structure of the tilted column. The largest of the three values is oriented along the column axis. The next largest value corre-

sponds to the column broadening direction and is oriented perpendicular to the column axis, but parallel to the substrate. The smallest of the three values is oriented orthogonally to the other two values. At normal incidence, these films will exhibit polarization dependent behaviour due to the biaxial nature of the film. An exception to this is the vertical post case where there is no structural anisotropy in the plane of the substrate and therefore is uniaxial.

With an understanding of the GLAD process and how the general biaxial nature of obliquely deposited films arises, the advantages of implementing obliquely deposited films as optical layers becomes apparent. It was stated earlier that the extent of vapour flux shadowing is determined by the deposition angle. This simultaneously influences two separate aspects of the film morphology that impact the resulting optical properties. First, the increased shadowing at higher deposition angles will result in a decrease in film density, which in turn will result in a lower average refractive index in the film. Additionally, this increase in shadowing at higher deposition angles will increase the index contrast between the indices oriented in the shadowing and broadening directions. As a result, tilted columnar thin films can be grown with control over the three principle refractive indices.

Variable angle spectroscopic ellipsometry (VASE) is an optical characterization method commonly used to analyze columnar thin films [52]. The VASE method is a versatile process which can measure columnar film properties such as film thickness, film density, refractive index and column orientation. By measuring changes in input linear *s*- and *p*-polarized light upon transmission through and reflection off of a sample, a general matrix which describes the specular interaction of light on the sample can be obtained. This

Mueller matrix (Eq. 1.2) is a 4×4 matrix which describes the relationship between incoming and outgoing light when it interacts with an optical element (Eq. 1.3). The polarization states of the incoming and outgoing light are described by four element Stokes vectors (Eq. 1.4. A Stokes vector defines the polarization state and intensity of the light represented with a basis containing linear and circular polarization states [53] and can describe polarized, partially-polarized, and unpolarized light. The Mueller matrix is a more generalized version of the Jones matrix and must be used in the treatment of partially-polarized and unpolarized light.

$$M = \begin{pmatrix} m_{11} & m_{12} & m_{13} & m_{14} \\ m_{21} & m_{22} & m_{23} & m_{24} \\ m_{31} & m_{32} & m_{33} & m_{34} \\ m_{41} & m_{42} & m_{43} & m_{44} \end{pmatrix}. \tag{1.2}$$

$$\vec{S_0} = M\vec{S_i}. \tag{1.3}$$

$$\vec{S} = \begin{pmatrix} S_0 \\ S_1 \\ S_2 \\ S_3 \end{pmatrix}. \tag{1.4}$$

Throughout this thesis, a V-VASE with autoretarder (J. A. Woollam Co., Inc.), operating in a rotating analyzer configuration is used for ellipsometric characterization. The autoretarder or compensator is a computer controlled magnesium fluoride Berek waveplate which can generate appropriate retardance values $0 - 90^{\circ}$ over a wide spectral range ($140 - 2500$ nm).

For anisotropic, depolarizing samples, a compensator is needed to effectively characterize the sample. This is because additional elements of the Mueller matrix need to be measured to obtain full characterization of the sample, and such elements require the use of a compensator.

Traditionally, ellipsometric analysis is performed near the Brewster angle because the best ellipsometric measurements occurred near this angle. However, with the incorporation of compensators, this has become less important. All ellipsometric characterizations preformed for this thesis were at incidence angles between 45° and 70° and wavelength between $400\ \mathrm{nm}$ and $1700\ \mathrm{nm}$.

1.3.3 Crystal Phase

Crystal phases in materials are commonly observed and characterized with x-ray crystallography. X-ray crystallography involves the elastic scattering of x-rays to determine the presence of crystalline planes within a material. For a crystalline sample, x-rays at specific angles of incidence will reflect off of adjacent crystal planes and constructively interfere. These angles are given by the well known Bragg relation:

$$\mathrm{n}\lambda = 2d\sin\theta. \tag{1.5}$$

This equation effectively states that for a given x-ray wavelength, crystalline plane spacing is directly linked with a specific angle of reflection. The locations and magnitudes of these reflection peaks act as a material fingerprint and can be used to determine material composition and purity. In addition to crystalline materials, which have a single periodic orientation, x-ray crystallography can be used to characterize materials with other crystalline

states. The different crystalline states are listed below and shown in Fig.1.4.

- Single Crystal - Exhibits a sharp peak in both directions (Fig. 1.4d).
- Textured - Material exhibits a sharp peak in the horizontal direction and a broad peak along an arc in the vertical direction (Fig. 1.4c), and contains crystallites having a preferred spatial orientation.
- Polycrystalline (Untextured) - Material exhibits a sharp peak in the horizontal direction and uniform intensity along an arc in the vertical direction (Fig. 1.4b), and contains crystallites having no preferred spatial orientation.
- Amorphous - Material contains no sharp peaks in either direction (Fig. 1.4a). However, both nanocrystalline and amorphous materials can exhibit broad peaks in the horizontal direction. Since, the x-ray crystallography experiments in this thesis were not designed to detect these broad peaks, in the context of this thesis, the term amorphous can refer to nanocrystalline or amorphous phases.

In Fig. 1.4, increasing x-ray incidence angle goes from right to left. Therefore, features which occur further left correspond to increasing crystalline planar spacing. Fig. 1.4a is representative of an amorphous material, showing no preference in x-ray incidence angle. Figs. 1.4b, c, and d are representative of different crystalline phases. Fig. 1.4b is representative of a polycrystalline material, showing multiple preferred x-ray incidence angles, but no preferred orientation. Figs. 1.4c and d are representative of textured and single crystalline materials respectively. These crystalline phases both have a single preferred x-ray incidence angle corresponding to a uniform crystalline

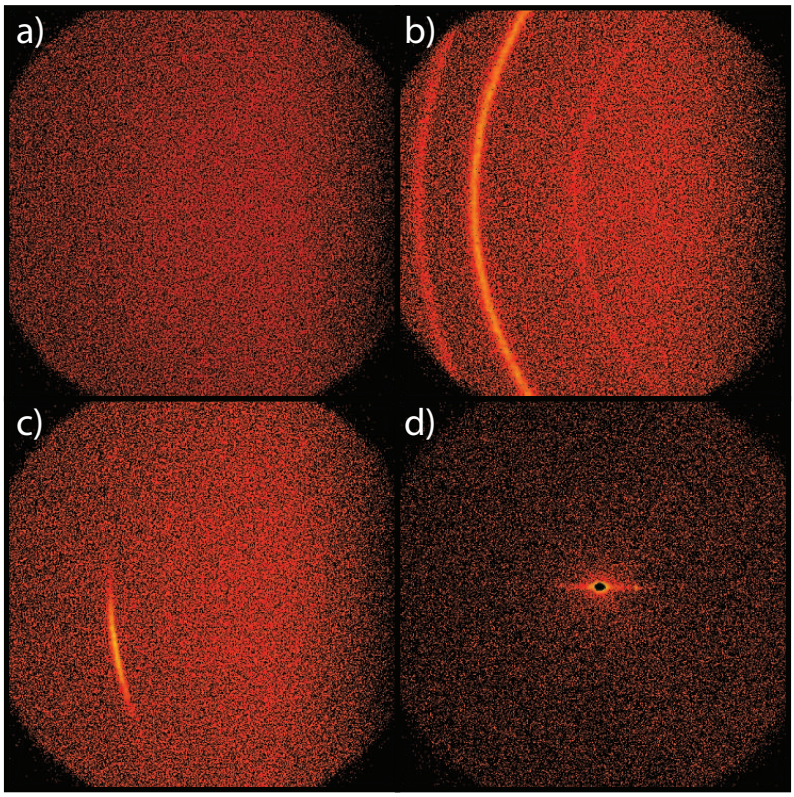

Figure 1.4. *X-ray crystallography images of a)amorphous, b)polycrystalline, c) textured, and d) crystalline materials.*

spacing, but different degrees of preferred orientations. The textured material in Fig. 1.4c shows some preferred crystalline orientation, whereas the single crystalline material in Fig. 1.4d shows a single preferred crystalline orientation. The spreading of the features along the horizontal axes in Figs. 1.4b, c, and d are a result of the thin film nature of the materials.

GLAD film crystalline properties were investigated using x-ray diffraction (XRD, Bruker D8 Discover). The goniometer was equipped with a copper x-ray tube with a 0.5 mm collimator and a Hi-Star area detector positioned 15 cm from the sample. A symmetric θ-2θ scan was used for data collection.

1.3.4 Surface Area

Thin film surface area measurements were obtained using the Brunauer, Emmett, Teller (BET) method [54]. The BET method, which describes multilayer adsorption, is an extension of Langmuir theory [55]. The Langmuir adsorption equation (Eq. 1.6) describes the coverage of gas molecules on a solid surface.

$$\theta = \frac{\alpha P}{1 + \alpha P}. \tag{1.6}$$

Here, P is the gas pressure and α is the Langmuir adsorption constant. The Langmuir adsorption constant increases with the binding energy of adsorption and decreases with temperature. The BET method is an extension of this theory with the following assumptions:

- The gas molecules physically adsorb onto a solid in layers infinitely
- There is no interaction between adsorbed layers
- The Langmuir theory can be applied to each layer individually

The BET equation is given by Eq. 1.7. This equation is linear in the range $0.05 < (P/P_0) < 0.35$ and can be used to extract the monolayer adsorbed gas quantity,υ_m (Eq. 1.8), and BET constant, c (Eq. 1.9), using the slope, m (Eq. 1.10), and the y-intercept, b (Eq. 1.11), of the linear region. In the BET equation, P refers to the equilibrium pressure and P_0 refers to the saturation pressure.

$$\frac{1}{v\left[\left(\frac{P_0}{P}\right)-1\right]} = \frac{c-1}{v_m c}\left(\frac{P}{P_0}\right) + \frac{1}{v_m c}. \tag{1.7}$$

$$v_m = \frac{1}{\mathrm{m}+\mathrm{b}}. \tag{1.8}$$

$$c = 1 + \frac{\mathrm{m}}{\mathrm{b}}. \tag{1.9}$$

$$\mathrm{m} = \frac{c-1}{v_m c}. \tag{1.10}$$

$$\mathrm{b} = \frac{1}{v_m c}. \tag{1.11}$$

With v_m, the total surface area can be obtained with Eq. 1.12. Here, N is Avogadro's number, s is the adsorption cross-section of the adsorbing species, and V is the molar volume of the adsorbate gas. The specific surface area can be found by dividing the total surface area S_{total} by the adsorbent mass.

$$S_{total} = \frac{v_m N s}{V}. \tag{1.12}$$

Most commonly, nitrogen is used as the adsorbate gas which permits accurate measurement of absolute surface areas as low as $0.5\ \mathrm{m}^2$. To reduce the required substrate size needed to obtain accurate surface area measurements, krypton gas was used instead of nitrogen for the surface area measurements presented in this thesis. The use of high-sensitivity krypton gas allows for reduction in the minimum required absolute surface area by a factor of 100 for accurate measurement [56,57]. Since krypton has a much lower saturation

pressure compared to nitrogen, the amount of gas remaining in the void volume will be much less when krypton is used rather than nitrogen. This will reduce the void volume error and allows for the analysis of samples with greatly reduced area. Since krypton allows for the analysis of a much smaller sample than with nitrogen, the use of krypton gas was much more compatible with measuring GLAD thin film samples. Details on the procedure used to measure the surface area of the samples presented in this thesis are outlined below.

To obtain data on specific surface area, substrates were measured with a Sartorius MC5 microbalance before and after each deposition to determine the film's deposited mass. After mass measurements and any post deposition oxidation, a sample with a total footprint area of $\sim 40\ \mathrm{cm}^2$ was cleaved into pieces ($\sim 1\ \mathrm{cm} \times 1\ \mathrm{cm}$) and put into a $12\ \mathrm{mm}$ diameter glass bulb (Quantachrome). Prior to adsorption testing, the glass holder containing the sample was outgassed at $150\ ^\circ\mathrm{C}$ for $2\ \mathrm{h} - 20\ \mathrm{h}$ under vacuum in a degassing station of the Quantachrome Autosorb-1MP. Krypton adsorption (Praxair, 99.999% pure) at liquid nitrogen temperature (77 K) was obtained for pressures from $0.05p_0$ to $0.5p_0$ where p_0 = 2.63 mmHg (the saturation pressure of the supercooled liquid). This adsorption data was used to perform a BET analysis, following the methodology of Krause *et al.*, to obtain sample surface area [57]. Film mass, thickness and footprint area were used to calculate specific surface area and surface area enhancement, SSA and SAE, respectively. SSA was found by dividing the total measured surface area by the total deposited film mass. SAE was found by dividing the total measured surface area by the film thickness (measured through SEM) and substrate footprint area. Substrate footprint area was obtained through image analysis of substrate photos with

ImageJ [58].

Chapter 2

Argon-Assisted Deposition

2.1 Ar-Assisted GLAD Process[1]

The focus of this chapter is to outline and characterize the Ar-assisted deposition process. Discussion will begin with a generalized system geometry and then address system specific parameters. Characterization of the argon source follows. Once the geometry and argon source profile are understood, the effects of substrate motion on film growth will be explored. Focus will then shift to discussing the roles of sputtering an increased surface diffusion in modifying film growth. Understanding these characteristic mechanisms will provide a solid foundation for evaluating film property modification with the Ar-assisted glancing angle deposition process.

2.1.1 System Geometry

Even though the traditional GLAD technique is reasonably well understood, the implementation of argon bombardment complicates the process. The ge-

[1]My contributions to the research presented in this thesis include all theoretical and experimental design and results unless otherwise noted.

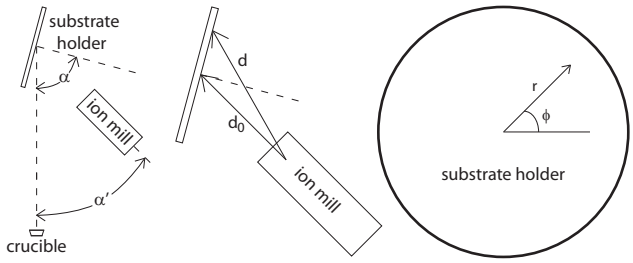

Figure 2.1. *Deposition setup illustrating the orientation of the argon source relative to the vapour source (left), the orientation of the argon source relative to the substrate holder (middle), and substrate holder positional parameters (right).*

ometry of the key components present in the Ar-assisted GLAD setup discussed in this thesis and the parameter definitions discussed in this section are shown in Fig. 2.1. The angular separation between the material and argon sources will be denoted as α'. In general, the argon incidence angle at the center of the substrate holder can be written as

$$\theta_0 = \alpha - \alpha'. \tag{2.1}$$

This adequately describes the incident argon angle at the center of the substrate holder, but other factors must be taken into account to generalize this to an arbitrary point on the substrate holder. The first step is determining the distance from the argon source to an arbitrary point on the substrate holder. By geometry, this distance relation d is

$$d = \sqrt{r^2 + d_0^2 + 2rd_0 \sin\phi \sin(\alpha - \alpha')}. \tag{2.2}$$

where r and ϕ are the polar coordinates on the substrate holder. Using similar geometry arguments, a relationship for θ, the incident argon angle at an

arbitrary point on the substrate, can be obtained

$$\theta = \arccos\left(\frac{d_0}{d}\cos(\alpha - \alpha')\right). \tag{2.3}$$

2.1.2 Beam Characterization

With the general Ar-assisted deposition geometry defined, the next step is to describe the basic operating principles of the argon source and calculate the parameters specific to the experimental setup.

The argon source used for the studies presented in this thesis is an Anatech IG-30 ion source. The ion source is comprised of three stages: the emitter stage, the anode stage and the accelerating stage. A simplified schematic of the ion source is shown in Fig. 2.2.

The main function of the emitter stage is to extract electrons from an emitting surface (1) via field emission with an applied potential (2). The electrons are extracted to a receiving port where they then travel into the anode stage. As the electrons arrive at the anode stage, they pass through a fixed magnetic field which bends the path of the electrons. This bending is done for two reasons. First, the lateral movement imparted by the magnet (3) increases the number of interactions between the electrons and the argon gas which improves the efficiency of argon ion generation. Second, the magnet also reduces heating of the screen (6) by axial electron impact.

The anode stage has two main functions. First, the anode stage is where the argon ions are generated in a glow discharge process through interactions with the energetic electrons arriving from the emitter stage. Second, the an-

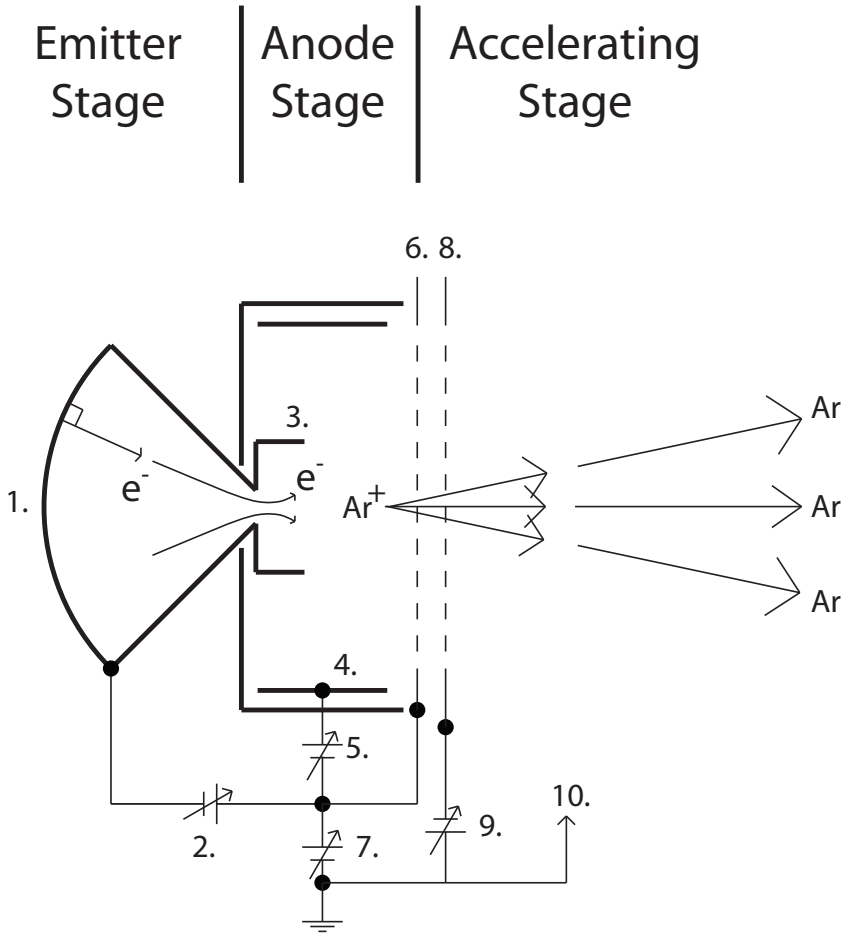

Figure 2.2. *Simplified schematic of the ion source. Reproduced from Barr [59].*

ode (4) in the anode stage is used to produce a potential (5, 7) between the anode and the screen which propels the argon ions out of the anode stage and into the accelerating stage. The accelerating stage consists of a grid (8) which is negatively biased (9) to further assist with ion extraction from the anode stage.

After the argon ions leave the accelerating stage, they pass through a neutralizer (10) which removes their electric charge. Neutralization occurs

through a charge exchange plasma, where the plasma provides an electrically conductive path from the ion beam to the grounded chamber walls. Alternative methods for achieving beam neutralization involve the use of external filaments to produce electrons.

Since the beam used in these studies is neutralized as it leaves the source, the resulting output of the argon source and, therefore, the bombarding species are neutral argon atoms, rather than ions. As a result, the bombardment-assisted process used in this thesis to modify film growth will be referred to as argon-assisted deposition.

Since both the material vapour source and argon source are locked down to specific ports in the vacuum chamber, they remain oriented at $\alpha' = 45^\circ$ angle relative to each other. The argon incidence angle θ (measured relative to substrate normal) is therefore directly related to α and any change in α necessarily means similar changes in θ.

The argon source output is a perforated aperture measuring 3 cm in diameter, which is positioned 20 cm from the center of the substrate holder. If the argon source were to be modeled as a point source having a Gaussian beam profile and a r^2 dependence, it would be inaccurate to define the source location at the output aperture. Instead, the true location of the source is inside the gun assembly, as illustrated in Fig. 2.1. To obtain an estimate of the exact location of the argon source, an experiment was designed to measure the projection of the Gaussian beam profile of the argon source onto the substrate holder. In this experiment, substrates were placed on the substrate holder and a slanted post Ar-assisted GLAD film of titanium dioxide was fabricated at $\alpha = 85^\circ$. A slanted post film was chosen because is used a static

substrate position during deposition. This ensures that measurements at specific points on the substrate will correspond to specific beam conditions. The film will undergo a densification that is proportional to the argon flux during fabrication when irradiated (see Chapter 3). It was assumed in this experiment that the densification would result in a decrease in film thickness that is linearly proportional to the argon flux. This allows for an estimate of the argon flux density to be obtained from the film thickness profile. The Ar-assisted film was then analyzed with a scanning electron microscope (SEM, JEOL field emission SEM) to determine film thickness at regular intervals throughout the film. Selected images are shown in Fig. 2.3. The analysis points were taken at the center of the substrate holder at regular locations all equally spaced along the direction normal to the deposition plane and along the diameter of the holder. These points were chosen because the resulting film thickness distribution would be symmetric in this direction, independent of deposition angle. Also, to minimize the impact of the underlying film thickness non-uniformities, we selected a $20\ \mathrm{cm}$ region at the center of the substrate holder and normal to the deposition plane. The work by Wakefield and Sit predicts an approximate 5% non-uniformity for a $10\ \mathrm{cm}$ region [60]. The resulting first-order approximation of the argon flux distribution and a Gaussian fit are shown in Fig. 2.4. This provides enough information to obtain an estimate on the argon source position.

To determine the argon source position, the divergence of the argon beam is modeled with a six-sigma approximation. In this method, the portion of the Gaussian beam distribution that lies outside of three standard deviations (three sigma) on either side of the mean is neglected. The standard deviation, σ, of the Gaussian fit was found to be 33.4 mm, making the three sigma value

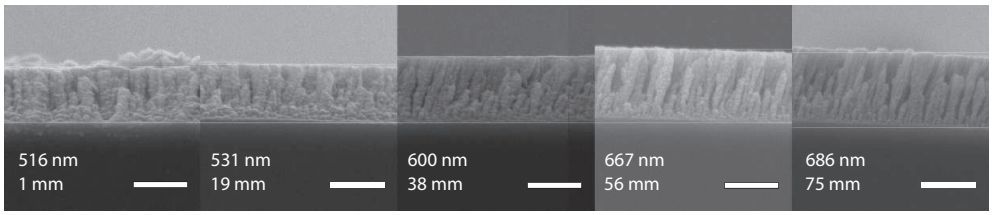

Figure 2.3. *SEM images of TiO_2 GLAD films grown with Ar-assisted deposition. Film thicknesses in nm, substrate position in mm. Scale bar corresponds to 500 nm.*

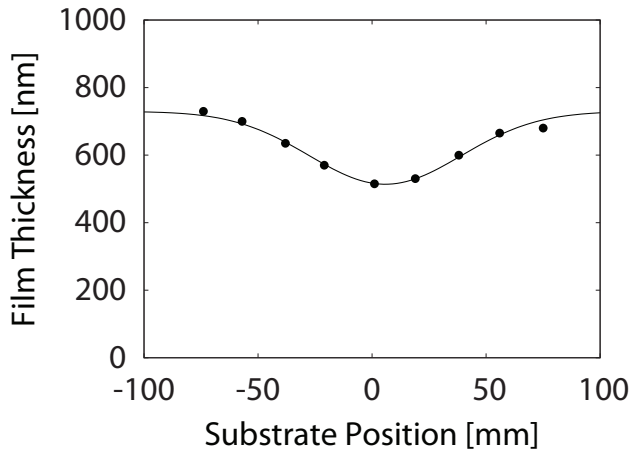

Figure 2.4. *Thickness profile in an Ar-assisted TiO_2 slanted post film.*

100 mm. It was also assumed that the aperture diameter was equal to the characteristic six-sigma width. Combining this information with the aperture to substrate holder center distance sets up a simple geometry that allows the source location to be estimated using similar triangles. These calculations are shown in Appendix A. Using this method, the minimum source-substrate holder distance d_0 was found to be 235 mm.

Now that the equipment-specific parameters have been calculated, the next step in the calibration process is to find the argon flux distribution across the substrate holder. Up to this point, only the effect of the flux distribution

on the film structure has been accounted for. However, since a linear relationship between film thickness and the argon flux is assumed, the two distributions are related by a scalar factor. The first step in determining this factor is to integrate the Gaussian film thickness distribution from Fig. 2.4 to find the total reduction in film volume due to the reduced thickness across the substrates.

$$\int_0^{2\pi} \int_0^{\infty} r e^{-\frac{r^2}{2(\sigma^2)}} \, dr \, d\phi. \tag{2.4}$$

It was assumed that the argon beam distribution is circularly symmetric and that the contribution from a non-uniform angle of argon incidence on the film thickness distribution can be neglected. The validity of these assumptions is addressed in the next chapter. The result of this integral gives a total volume reduction of $1.5 \times 10^6 \ \mathrm{nm \cdot mm^2}$. This value can be related to the final argon distribution $\Phi(r, d)$ through the film thickness distribution, the film deposition time, and the argon beam current. The final argon distribution with distance correction is shown in Eq. 2.5 and the normalized distribution is plotted in Fig. 2.5. These calculations, which are detailed in Appendix A, indicate a peak argon current density of $0.70 \ \mathrm{A/m^2}$ at the substrate holder center.

$$\Phi(r, d) = 0.70 \ \mathrm{A/m^2} \cdot e^{-\frac{r^2}{2(33^2)}} \left(\frac{d_0}{d} \right)^2. \tag{2.5}$$

The normalized flux distribution shown in Fig. 2.5 at normal incidence is non-uniform across the $20 \ \mathrm{cm}$ diameter substrate holder by approximately 99%. This requires extra care be taken to ensure that every sample is de-

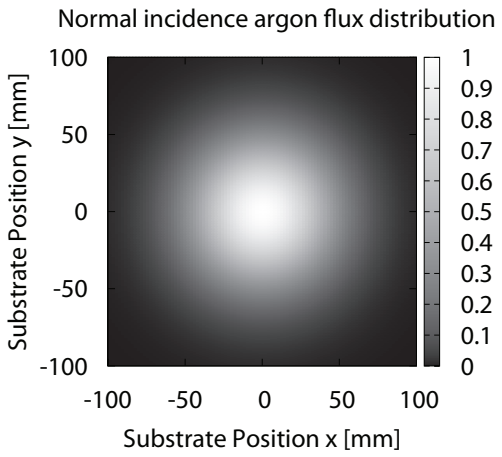

Figure 2.5. *Argon flux distribution at normal argon incidence normalized to peak argon flux.*

posited in the same position as the last and that all measurements be taken from the same location. An example showing the changes in the argon flux distribution when using an oblique deposition angle of 81° is shown in Fig. 2.6.

This result also implies that any Ar-assisted samples that require substrate rotation at $\alpha \neq \alpha'$ will see fluctuations in argon flux due to the changing position and argon incidence angle. The fluctuation in argon incidence angle at a deposition angle of 81° is shown in Fig. 2.7. Fig. 2.7a shows the substrate holder (bold circle) with samples at set radii, which traverse paths corresponding to helical or vertical post films, superimposed on the angular argon incidence distribution. Fig. 2.7b is a plot of the fluctuations these samples see when they traverse these paths. From Fig. 2.7b it is apparent that these samples can see a large fluctuation in argon incidence, as large as approximately 30° near the edge of the substrate holder. In light of these characteristics of the Ar-assisted process, all samples in these studies are analyzed

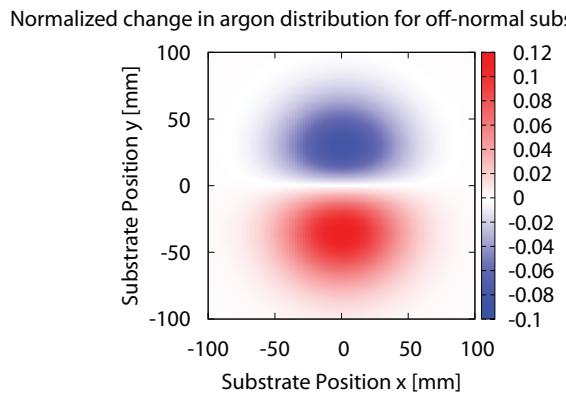

Figure 2.6. *Changes to the argon flux distribution when the argon incidence angle is non-normal ($\alpha = 81°$). Values are normalized to peak ion flux.*

at the substrate holder center unless otherwise noted.

2.2 Mechanisms[2]

With an understanding of the geometry and equipment used in the Ar-assisted deposition process, the underlying mechanisms responsible for the modification of film growth are considered. Here, two possibilities are considered: removal and redistribution of material through sputtering and increased surface diffusion through additional substrate heating.

Sputtering of bulk materials have been studied for more than a century, beginning with early reports on sputtering by Grove and Faraday [2,3]. Since then, sputtering has become the most commonly used and among the most widely studied physical vapor deposition process used for industrial thin film coatings. Since a great deal of effort has been focused on the industrial applications of sputtering, some aspects of sputtering have been exhaustively

[2]Portions of Sec. 2.2 have been published in [61]

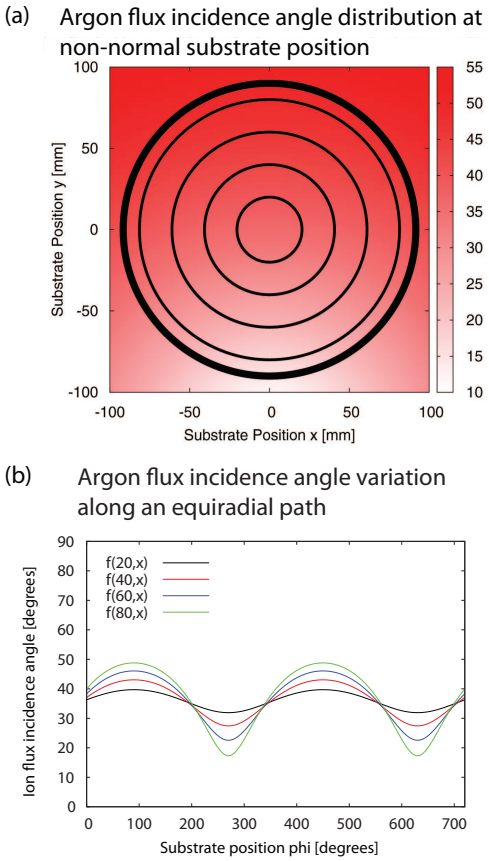

Figure 2.7. *Angular distribution of incident argon flux at non-normal substrate orientation.*

studied while reports in other areas are very scarce. Prior reports have shown metal-oxide compounds to have lower sputter yield than the pure base metals [62–64]. As a result, the general practice of growing metal-oxide films through sputtering generally involves reacting a pure sputtered metal within an oxygen atmosphere. Reported sputtering parameters are abundant for pure metals, but are largely unavailable for metal-oxide compounds. An exception is the recent report by Baer *et al.* [65], which discusses relative sputter rates for a number of metal oxides, but does not report absolute sputter

yields.

Studies on physical vapor deposition at normal incidence with simultaneous ion bombardment have been reported for nearly 30 years [66]. Most commonly this deposition process is referred to as ion-beam-assisted deposition (IBAD). Since IBAD was first reported, numerous reports have focused on film property modification [66–81], however, reports on ion beam modification of highly porous films during deposition are scarce. Since there is large potential for porous thin films grown by glancing angle deposition to be modified through bombardment, there is substantial motivation for further study into bombardment-assisted processes.

The following discussion will look at the different possible mechanisms influencing film growth in the Ar-assisted GLAD process. Sputtering will be discussed as well as increased diffusion through substrate heating and momentum transfer. This will provide insight as to why films grown with an Ar-assisted process differ from those grown unassisted.

2.2.1 Sputtering

First we consider the effect of sputtering in the Ar-assisted process. Unless otherwise noted, all Ar-assisted films grown in these studies were grown with an argon energy of $390\ \mathrm{V}$. At $390\ \mathrm{V}$, the argon energy ranges from 2 to 27 times the sputtering threshold proposed by Bohdansky *et al.* [82], which is dependent on material. An experiment investigating the sputter yield of TiO_2 was conducted. A dense TiO_2 film grown at $\alpha = 0°$ underwent a post-deposition ion mill (Ionfab 300 Plus) at normal incidence for $1\ \mathrm{h}$. A beam energy of $500\ \mathrm{V}$ and beam current of $120\ \mathrm{mA}$ was used. Samples were re-

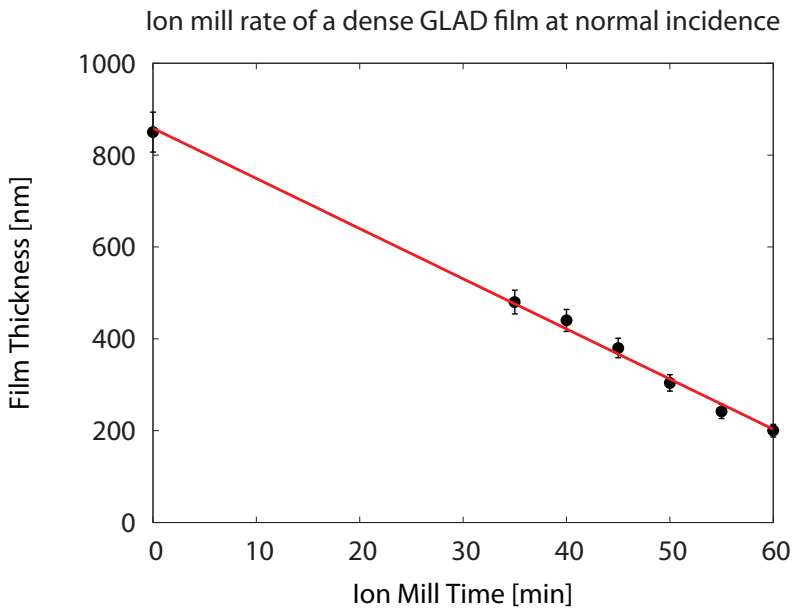

Figure 2.8. *Ion milling of a dense TiO_2 film grown at normal incidence.*

moved at various points during the ion mill to have their thickness measured with SEM. The results of this experiment are shown in Fig. 2.8.

From this data, the rate of thickness reduction was obtained. To find the total amount of material removed, this value was combined with the substrate area and material density to determine the total number of molecules sputtered during the milling process. The total ion dose during the milling process was found from the product of the mill time and ion current. By comparing the total number of molecules removed with the total ion dose, the sputter yield of TiO_2 at normal incidence was found to be 0.06 molecules per argon atom. This calculation assumes no redeposition of sputtered atoms.

The mass deposition rate of unassisted and Ar-assisted slanted post films grown at a deposition angle $\alpha = 85°$ for a number of materials was investi-

Table 2.1. *Source material purity and deposition conditions used in unassisted and Ar-assisted GLAD film deposition. ITO composition is 91:9 In_2O_3:SnO_2.*

Material	Purity	P_{Dep} 0 mA	P_{Dep} 5 mA
	%	Pa	Pa
Al_2O_3	99.99	2.0×10^{-3}	1.0×10^{-2}
CaF_2	99.95	2.4×10^{-3}	9.5×10^{-3}
ITO	99.99	1.1×10^{-2}	1.6×10^{-2}
MgF_2	99.9	2.0×10^{-4}	1.0×10^{-2}
Nb_2O_5	99.95	2.0×10^{-3}	1.1×10^{-2}
SiO	99.9	1.2×10^{-3}	9.3×10^{-3}
SiO_2	99.99	6.7×10^{-3}	8.7×10^{-3}
SnO_2	99.9	1.7×10^{-2}	2.5×10^{-2}
Ta_2O_5	99.95	4.3×10^{-3}	1.3×10^{-2}
TiO_2	99.9	6.7×10^{-3}	9.3×10^{-3}
Y_2O_3	99.9	3.3×10^{-3}	9.3×10^{-3}
ZrO_2	99.7	3.3×10^{-3}	1.5×10^{-2}

gated. Information on the purity and deposition pressures for these materials are shown in Table 2.1. The mass deposition rates for these materials are shown in Table 2.2, and were calculated by dividing the total deposited film mass by the deposition time. Film mass was obtained by weighing the substrates before and after deposition with a Sartorius MC5 microbalance. Since the deposition rates at the quartz crystal monitor were held constant for the unassisted and Ar-assisted films, the difference in mass deposition rates at the substrate should give some indication as to what degree sputtering plays a role in the Ar-assisted process. If sputtering is removing material, the mass deposition rate in the Ar-assisted films should be lower than in the unassisted films and Δ should be positive in Table 2.2. When the mass rates are compared in Table 2.2, there is no significant measureable difference between the sample sets.

To eliminate the possibility of differences in post deposition oxidation accounting for any measured mass change, the TiO_2 films underwent a post

Table 2.2. *Mass deposition rate at the substrate of unassisted and* $5\ \mathrm{mA}$ *assisted GLAD films. Error is estimated to be less than 5%.*

Material	$\alpha = 85^\circ, 0\ \mathrm{mA}$ [$\mathrm{mg\ min^{-1}}$]	$\alpha = 85^\circ, 5\ \mathrm{mA}$ [$\mathrm{mg\ min^{-1}}$]	$\Delta(\alpha = 85^\circ)$ [$\mathrm{mg\ min^{-1}}$]
Al_2O_3	0.20	0.22	-0.018
CaF_2	0.11	0.17	-0.057
ITO	0.44	0.41	0.031
MgF_2	0.14	0.17	-0.031
Nb_2O_5	0.19	0.20	-0.012
SiO	0.11	0.14	-0.029
SiO_2	0.14	0.11	0.030
SnO_2	0.53	0.47	0.061
Ta_2O_5	0.34	0.36	-0.014
TiO_2	0.14	0.13	0.015
Y_2O_3	0.36	0.28	0.080
ZrO_2	0.23	0.29	-0.067

deposition oxidation treatment in an oven open to atmosphere. The samples were oxidized for $24\ \mathrm{h}$ at $200\ ^\circ\mathrm{C}$ and were weighed before and after oxidation to determine the contribution of oxidation to the total deposited film mass. The oxidation was found to contribute less than 1% of the total film mass. Since this effect is small, oxidation alone cannot solely account for the measured difference in mass deposition rates seen between the unassisted and Ar-assisted films. It is concluded that sputtering (from argon bombardment) is not significant or is followed by redeposition of any sputtered film material. Such redeposition is caused by the porous nanostructure of the coatings, and follows the mechanism proposed by Fleischauer *et al*. [83]. This effect is shown in Fig. 2.9.

To determine the frequency of sputter events in the Ar-assisted process, the mass removal rate of TiO_2 from the post deposition milling experiment is scaled and compared with the mass deposition rate data from the Ar-assisted TiO_2 film. As a first estimate, the different beam energies of $500\ \mathrm{V}$ and $390\ \mathrm{V}$ from the two different processes were assumed to have the same

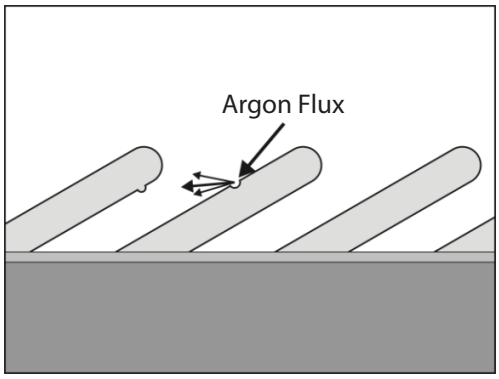

Figure 2.9. *Redeposition of sputtered material in a porous thin film.*

sputter yield. To scale from the $120\ \mathrm{mA}$ beam current in the post deposition milling experiment to the $5\ \mathrm{mA}$ beam current in the Ar-assisted experiments, the mass removal rate was scaled in direct proportion to the beam currents. Under these assumptions, it is estimated that 9 TiO_2 film molecules are deposited for every sputtered TiO_2 molecule.

In addition to TiO_2, the sputter yield was found for SiO_2. Film thickness of a thermal oxide was measured before and after milling in the Ar-assisted setup with a Filmetrics resist and dielectric thickness mapping system. The thickness reduction was measured to be $1.6\ \mathrm{nm\ min^{-1}}$. When this measurement is related to bulk SiO_2 properties and the argon dose, the sputter yield is found to be 0.13. The ratio of TiO_2 and SiO_2 sputter yields is 0.45, agreeing roughly with Baer *et al.* [65] who reported 0.54. Slight disagreement between the two values may be due to the higher ion energy used ($2\ \mathrm{kV}$) by Baer *et al*.

The relative contribution of sputtering in the Ar-assisted GLAD process is estimated next. The measured sputter yield for TiO_2 is applied to obtain an estimate of the thickness reduction in a porous TiO_2 film and compared to

the thickness reduction observed in Fig. 2.4.

If one assumes that sputtering from the argon beam removes film material, then the 0.06 sputter yield for TiO_2 should lead to a reduction in thickness of porous TiO_2 of $50\ \mathrm{nm}$ when the deposition rate and argon flux are taken into account. This simple calculation assumes that the sputtered material is removed and that no redeposition takes place, although redeposition is likely occurring due to the slanted post geometry. The observed thickness reduction at the substrate center in Fig. 2.4, is approximately $200\ \mathrm{nm}$. In this simplified analysis, where possible enhancement of sputter yield at oblique incidence is neglected, sputtering of the film accounts for only about one quarter of the reduction in film thickness and thus, the argon bombardment must be influencing the film growth in other manners.

2.2.2 Diffusion

To assess the possible contribution of surface diffusion to the Ar-assisted process, the different heating sources and how they contribute to the overall substrate temperature are investigated. Three sources are considered: heat of sublimation from the material collecting on the substrate, radiative heating from the material source, and heating from the argon source through momentum transfer. If increased surface diffusion is responsible for the property modification in the Ar-assisted GLAD process, argon source heating must play a significant heating role.

The impact of surface diffusion in the context of Ar-assisted GLAD depositions is considered. Mueller's simulations of 100 eV argon on nickel films predict two characteristic processes [84]. First, the argon bombardment pro-

vides additional energy for adatoms to diffuse along the column surface. This increase in diffusion results in column smoothing that decreases film surface area. This process and its relation to film density was also investigated by Ensinger [76]. Second, the momentum from the energetic argon neutrals can transfer to clusters of surface atoms, causing them to collapse into trapped voids beneath these clusters. These two processes may lead to an increase in film density. Surface area and film density measurements will be discussed in the next chapter; however, it is noted at this point that indeed surface area decreased and film density increased with argon-assistance.

The heating contribution from film deposition on the substrate is determined by deposited mass and each material's heat of sublimation. This, when combined with deposition time, allows an estimate of power imparted to the substrate. Here, a sample calculation of tantalum oxide is presented. Inghram *et al*. report a value of 152.2 kcal/mol for the heat of sublimation of tantalum oxide [85]. This is equal to $637\ \mathrm{kJ/mol}$. Using 16 mg for the deposited mass of a Ta_2O_5 on a 10 cm diameter silicon wafer, the total energy transferred to the substrate through condensation can be calculated.

$$Total\ energy = \frac{(637\ \mathrm{kJ/mol})(16\ \mathrm{mg})}{441.89\ \mathrm{g/mol}} = 23\ J. \tag{2.6}$$

Using the total energy obtained from Eq. 2.6, the power can be calculated using the deposition time.

$$Power = \frac{Total\ Energy}{Deposition\ Time} = \frac{23\ J}{45\ min} = 8.5\ mW. \tag{2.7}$$

The power density is then calculated by dividing the total power by the

Table 2.3. *Estimated characteristic power associated with Ar-assisted deposition. The substrate heating is dominated by the argon source.*

Material	Power			$P_{Argon}/(P_{Rad}+P_{Dep})$
	Condensation [$\mathrm{mW\ cm^{-2}}$]	Radiative [$\mathrm{mW\ cm^{-2}}$]	Argon [$\mathrm{mW\ cm^{-2}}$]	
Al_2O_3	0.4	4.9	16	3.1
CaF_2	0.1	1.2	18	14
ITO	-	1.9	13	7.1
MgF_2	-	0.4	19	47
Nb_2O_5	-	4.5	13	2.9
SiO	-	1.0	21	21
SiO_2	0.2	2.1	19	8.6
SnO_2	0.4	1.8	15	6.7
Ta_2O_5	0.1	5.1	12	2.4
TiO_2	0.3	4.9	18	3.4
Y_2O_3	-	10.1	14	1.4
ZrO_2	0.4	8.0	16	1.9

substrate area.

$$Power\ Density = \frac{Total\ Power}{Substrate\ Area} = \frac{8.5\ mW}{\pi(5\ cm)^2} = 0.1\ \mathrm{mW/cm^2}. \tag{2.8}$$

Heating of 0.1 - 0.4 $\mathrm{mW\ cm^{-2}}$ was calculated for material condensation. This data is presented as the deposition power in Table 2.3. Unfortunately, the dataset for substrate heating due to film deposition is limited because heat of sublimation values were not found for all materials used in this study [85–87]. However, it will be shown that the effect of film deposition on the overall substrate heating is small or negligible when compared to the other sources. Since it is expected that the heat of sublimation values will be of similar magnitude over the entire sample set, the difference in heat of sublimation between the materials studied does not contribute significantly to the total energy incident on the growing GLAD film.

To calculate radiative power from the material source, an upper bound calculation was made using the total power applied to the molten material by the electron beam. This value was then scaled down by the emissivity of each material to determine the power arriving at the substrate surface. Emissivity values for molten metal oxides were not found for all of the materials used here, but in general ranged between 0.4 and 0.6, with an estimate of 0.5 used for unknown emissivities. To determine the power absorbed by the growing film, an additional correction was made to account for power reflected off of the substrate. To determine the reflectance, the Fresnel equations for s- and p-polarized light were used (Eqs. 2.9 and 2.10). The power radiated from the source is unpolarized, so the average of Eqs. 2.9 and 2.10 was used to determine the total reflectance.

$$R_s = \left(\frac{n_1 \cos\theta_i - n_2 \sqrt{1 - \left(\frac{n_1}{n_2}\sin\theta_i\right)^2}}{n_1 \cos\theta_i + n_2 \sqrt{1 - \left(\frac{n_1}{n_2}\sin\theta_i\right)^2}} \right)^2 . \tag{2.9}$$

$$R_p = \left(\frac{n_1 \sqrt{1 - \left(\frac{n_1}{n_2}\sin\theta_i\right)^2} - n_2 \cos\theta_i}{n_1 \sqrt{1 - \left(\frac{n_1}{n_2}\sin\theta_i\right)^2} + n_2 \cos\theta_i} \right)^2 . \tag{2.10}$$

The reflection was calculated for a single vacuum-film interface. The refractive index, n_1, was 1.0 for vacuum while the film refractive indices, n_2, were obtained in the near-infrared wavelength range from VASE measurements on films grown at normal incidence. An angle of incidence of 85° was used for θ_i in the calculation since it describes the orientation of the substrate relative to the heat source during the deposition. These calculations yield material dependent values that range between 0.55 and 0.65. When the

power arriving at the film is scaled down by transmittance (0.35-0.45) of the air-film interface, and assuming that the all of the transmitted power is absorbed by the film, the radiative power absorbed is found to be 0.4 $\mathrm{mW\ cm^{-2}}$ - 10.1 $\mathrm{mW\ cm^{-2}}$ and is presented in Table 2.3. The calculation of the upper bound of radiative power from the source is approximately an order of magnitude higher than the power transferred through material sublimation, with the exception of MgF_2. However, the experimental geometry (10 cm diameter substrate, 40 cm from material source) will only intercept a small fraction of the total radiation. If a cosine distribution is assumed for the radiation profile, the contribution from radiative heating is significantly reduced when only the fraction of radiation that gets directly intercepted by the substrate is considered. When this effect is considered the radiative component is reduced by an order of magnitude, making it approximately equal in significance to the effects of material sublimation. However, this effect was not included in the upper bound calculation for radiative heating.

The heating contribution from the argon source in Ar-assisted GLAD is determined next. The argon flux distribution inferred from Fig. 2.4 was used to obtain the peak power density at the substrate center. To obtain this value, the distribution was integrated and compared with the 2 W argon source conditions. This value was then scaled down to account for the 40° incident angle of the argon neutrals on the substrate, yielding a value of approximately $22\ \mathrm{mW\ cm^{-2}}$. Other factors such as argon implantation and reflection need to be considered when calculating an equivalent power density at the substrate center. A report by Martin can be used to predict implantation of argon to play a significant role in the Ar-assisted process [68], reporting a trapping coefficient of approximately 0.5 for 400 eV argon ions on glass substrates. This

report also predicts an implant depth of 1.5 nm - 2.5 nm for O^+ in ZrO_2. Wolff *et al.* predict an implant depth of ∼5 nm for $4\ \mathrm{keV}$ argon into TiO_2 layers on Ti [88]. Since our experiments were at 400 eV, we expect our trapping coefficient to be similar to the 0.5 and the implant depth close to the 1.5 nm - 2.5 nm reported by Martin. Thus, for the power calculation a value of 0.5 was used for the trapping coefficient. An argon reflection coefficient was also estimated from the literature. Eckstein and Verbeek report reflection coefficients of 0.85 for $15\ \mathrm{eV}$ and 0.4 at $4\ \mathrm{keV}$ for He^+ on W [89]. This report also states the expected reflection coefficient of compound targets to be about a factor of 2 lower than elemental targets [68]. By interpolating the data in Martin's report and considering a compound target, a reflection coefficient of 0.3-0.4 is estimated. Yamamura estimates the reflection of $400\ \mathrm{eV}$ argon gas to be between 0.25 and 0.4 for W covered by nitrogen adsorbate layers [90], further confirming the estimate of 0.3 to 0.4. Bearing in mind that trapping plus reflection coefficients must sum to unity, to put a lower bound on the contribution to substrate heating from the argon source, a value of 0.5 was used for the reflection coefficient in the power calculation. Therefore, with trapping and reflection coefficients of 0.5, half of the total $22\ \mathrm{mW\ cm^{-2}}$ is coupled to the substrate through argon implantation and a fraction of the remaining power will be coupled through momentum transfer from argon reflection.

To obtain a lower bound calculation, the reflected argon neutrals were assumed to have a minimum deflection angle such that the momentum transfer is minimized. Since the argon incidence angle used in this study is $40°$, the minimum reflection angle is $50°$. This choice corresponds to argon neutrals reflecting along the substrate plane at a minimum angle to minimize the energy transfer to the film. Reflection was treated as a two-dimensional collision

with total power transfer being equal to the ratio between energy imparted on the film molecule through momentum transfer and initial argon energy multiplied by the 0.5 reflection coefficient and the 22 $\mathrm{mW\ cm^{-2}}$ total incident power. The two contributions from argon implantation and reflection were then summed to obtain the total power transferred to the substrate, presented as argon power in Table 2.3.

When the three sources of substrate heating present in the Ar-assisted GLAD process are compared, the contribution from the argon source is found to be the dominant source of energy. The ratio of power transfer to the substrate from the argon source with the two contributions from film deposition and material source radiation the argon source contribution is found to range from 1.4 to 47 times the sum of the other two heat sources. This suggests that substrate heating plays a significant role in modifying the film properties in the Ar-assisted GLAD process. When it is considered that an upper bound calculation was used for the radiative power and a lower bound was used for the argon power, this ratio is a conservative estimate.

The heating calculations presented in this section allow for an assessment on whether or not the heating is significant enough to increase the substrate temperature such that film deposition occurs in zone two ($0.3T_m \leq T_S \leq 0.5T_m$) rather than zone one ($T_S \leq 0.3T_m$). Assuming that the heating is dominated by the argon source, the calculated argon source power of 22 $\mathrm{mW\ cm^{-2}}$ was used for this analysis. If this power is assumed to be evenly distributed across a 10 cm diameter silicon wafer, the substrate temperature is calculated to increase by about 10 degrees over a 45 minute deposition. This is extremely small in comparison to the material melting points and therefore

is not likely changing the conditions such that the films are growing in the higher temperature zone.

2.3 Conclusion

In this chapter, the basic Ar-assisted GLAD process was studied through investigation of system geometry, beam profile and process mechanisms. At a highly oblique deposition angle, the argon flux incidence angle was shown to have large variations across the substrate holder and have large swings in argon incidence angle at fixed points on the substrate holder with substrate rotation. The argon flux distribution was shown to be Gaussian, which contributes to film non-uniformity across the substrate holder. Quantification of these factors will assist in design of future Ar-assisted experiments.

Two mechanisms were considered for Ar-assisted modification. Sputtering was investigated during deposition with an Ar-assisted process, and post-deposition with an ion milling process. Sputter yields were found for TiO_2 (0.06) and SiO_2 (0.13), with the ratio of these sputter yields agreeing closely with literature values. This study also produced an estimate of 9 TiO_2 film molecules deposited for every TiO_2 sputtered in a specific Ar-assisted film deposition. Despite significant sputtering, the mass deposition rates were observed to be unchanged between standard and argon-assisted deposition. Thus, it is concluded that the thickness changes with argon bombardment are caused by densification, consistent with the mechanism proposed by Fleischauer *et al*. [83].

The other mechanism considered for Ar-assisted modification was surface diffusion. The relative energies associated with three characteristic pro-

cesses were compared to determine the dominant source of heat in both unassisted and Ar-assisted GLAD. In unassisted GLAD, when all radiation from the material source is assumed to reach the substrate, the dominant source of substrate heating was found to be radiant heating from the material source. Here, radiation from the material source was found to be roughly an order of magnitude higher than the energy transferred to the substrate through film flux condensation. However, radiative-based heating was found to decrease in significance when large substrate-source distances are involved. In Ar-assisted GLAD, the dominant source of substrate heating was found to be from the argon source. Argon entrapment and momentum transfer through argon-film interactions were both determined to be significant factors, and led to an argon source contribution to substrate heating of 1.4 - 47 times larger (material dependent) than the sum of the unassisted substrate heating mechanisms. This indicates that heating of the substrate from the argon source should play a significant role in film modification with the Ar-assisted process. These results should enable explanation of film property modifications presented in the next chapter.

Chapter 3

Argon-Assisted Film Properties

3.1 Introduction[1]

Film property modification of dense thin films with IBAD has been studied for many years. The earliest studies focused on increasing film density with IBAD and other desirable film properties arising from the density modification. Increases in the film density were reported to reduce moisture absorption [66] and improve film robustness in harsh environments by improving resistance to chemical attack [67]. Shortly afterwards, optical studies reported increases in refractive index due to increases in film density [68, 70, 74]. Further studies have since investigated modification of adhesion and resistance to abrasion [68, 72], film stress [70, 74, 75], annealing temperature [74], crystallinity and surface smoothness [75].

Following the description of the Ar-assisted GLAD growth process in chapter 2, the modification of numerous properties such as column tilt angle, film density, optical properties such as the principal refractive indices

[1] Portions of this chapter have been published in [61, 91]

and birefringence, and surface area are discussed in this chapter. Film crystallinity is analyzed and used to explain trends in the data. Material independent general trends are discussed and explained with prior reports on ion beam assisted deposition of dense films and the study on the Ar-assisted GLAD process reported in the previous chapter.

3.2 Film Growth

For these studies, a selection of metal oxide and fluoride films were deposited by electron beam evaporation onto Schott B270 glass (S.I. Howard Glass) and silicon (single-polished, p-type $\langle 100 \rangle$, University Wafer) substrates. Deposition materials (Cerac, Inc.) were 99.7% pure or better. Indium tin oxide (ITO) composition was 91:9 In_2O_3:SnO_2. Films were grown unassisted (no argon bombardment) at α = 0° and α = 85° incidence and at $\alpha = 85^\circ$ with $5\ \mathrm{mA}$ argon assistance. At a deposition angle of 85°, the argon incidence angle is 40°. For the α = 0° films, the substrate underwent constant, rapid rotation (one full substrate rotation per $5\ \mathrm{nm}$ of film growth) to promote film uniformity. The α = 85° films were grown without any substrate rotation to produce slanted post structures. A full listing of film materials used and deposition conditions are shown in Table 2.1.

Additional SiO_2 and TiO_2 films were grown to determine the effects of various deposition parameters. Slanted post SiO_2 films were grown at α = 70° and 85° to determine the effects of deposition angle and the phisweep process. To study the effect of deposition angle, SiO_2 films were deposited at α = 70° and 85°, both unassisted and Ar-assisted with a $5\ \mathrm{mA}$ beam current. Ar-assisted SiO_2 phisweep films were also grown at these deposition

angles with phisweep angles of $0, 26.5, 45$ and 90° with an argon beam current of 5 mA. To investigate the effect of argon beam current, additional TiO_2 films were grown at α = 85° at beam currents of $0, 2, 4$ and 6 mA. Serial bi-deposited (phisweep angle = 90°) TiO_2 films were grown at α = 70° and 85° with argon currents of $0, 2, 3, 4$ and 5 mA.

All films in these studies were grown at a nominal deposition rate of 1.0 nm s^{-1}. The normal incidence deposition rate measured by the QCM ranged from $0.8 - 1.2$ nm s^{-1} and films were grown to a nominal thickness of 1.0 μm (with the exception of $\alpha = 0^\circ$ ITO, which was grown to a nominal thickness of 0.4 μm to preserve visual transparency and minimize absorption in the optical measurements). Except for ITO, all films grown at $\alpha = 0^\circ$ were grown over a 15 - 20 minute duration. The unassisted films at $\alpha = 85^\circ$ in Table 2.1 were grown in 25 minutes. All Ar-assisted films at $\alpha = 85^\circ$ in Table 2.1 were grown in 45 minutes except for SiO_2 (60 minutes), TiO_2 (40 minutes) and ZrO_2 (40 minutes). The mass deposition rates for the films grown at $\alpha = 85^\circ$ in Table 2.1 are presented in Table 2.2.

Commonly, oxygen is added to the vacuum chamber during titanium dioxide depositions to maintain stoichiometric film growth. However, for our experiments we added argon to enable argon source operation. To improve stoichiometric composition in the Ar-assisted titanium dioxide films, after deposition all samples were held at 200 °C in an oven open to atmosphere for 48 hours. Similarly, in order to achieve visual transparency for all the materials used in these studies, various post deposition oxidation procedures were used in the oven. These are outlined in Table 3.1.

In this chapter, the VASE method was used extensively to determine film

Table 3.1. *Oxidation parameters used in unassisted and Ar-assisted GLAD films. Samples were oxidized until visually transparent.*

Material	Oxidation $\alpha = 0°, 0$ mA	Oxidation $\alpha = 85°, 0$ mA	Oxidation $\alpha = 85°, 5$ mA
Al_2O_3	14 h at 200 °C	N/A	N/A
CaF_2	N/A	N/A	N/A
ITO	1.5 h at 500 °C	1.5 h at 500 °C	72 h at 500 °C
MgF_2	N/A	N/A	N/A
Nb_2O_5	24 h at 200 °C	24 h at 200 °C	24 h at 200 °C
SiO	120 h at 200 °C, 48 h at 300 °C, 48 h at 400 °C	N/A	N/A
SiO_2	N/A	N/A	N/A
SnO_2	120 h at 200 °C, 48 h at 300 °C, 48 h at 400 °C	24 h at 500 °C	26 h at 500 °C
Ta_2O_5	24 h at 200 °C	70 h at 200 °C	70 h at 200 °C
TiO_2	14 h at 200 °C	24 h at 200 °C	24 h at 200 °C
Y_2O_3	N/A	N/A	24 h at 500 °C
ZrO_2	N/A	N/A	N/A

density, and principle refractive indices[2]. Ellipsometric characterization on slanted post films were obtained in reflection mode and analysis was performed with the WVASE32 software supplied with the ellipsometer. To characterize solid films grown at α = 0°, a Cauchy model [92] was used for all materials except TiO_2 where a Gaussian oscillator model was used. The Gaussian oscillator model was used for TiO_2 due to significant adsorption in the optical region. For materials that could be modeled with a Cauchy relation, the refractive index n was directly obtained. To obtain n in the TiO_2 case, the Kramers-Kronig relation was applied to the extinction coefficient k, obtained from the VASE scan. Once these models were obtained, the porous films grown at $\alpha = 85°$ were modeled as biaxial Bruggeman effective medium mixtures of void and film material. Normalized film density results obtained through VASE analysis were estimated to have a 5% error. The error in the refractive indices obtained through VASE analysis are estimated to be 0.015. The calculation of the in-plane birefringence involves the subtraction of two

[2]VASE analysis was done in collaboration with N. Wakefield

refractive indices, each having an error of 0.015. Therefore, the error in the in-plane birefringence is found by adding, in quadrature, the individual errors in the planar refractive indices. This results in an error in the in-plane birefringence of 0.021.

3.3 Film Density

Prior studies on film growth modification with IBAD have shown that film density of conventional (ie: not GLAD) thin films can be increased by argon assistance for films grown at normal incidence [93–95]. In this work, the modification of density of porous GLAD films with Ar-assisted deposition was studied. Increases in film density in Ar-assisted GLAD films should result in larger refractive indices which can be valuable in the fabrication of optical devices.

Film density measurements (Table 3.2) were obtained by dividing sample mass by substrate area and film thickness. Sample mass was obtained by weighing the substrate before and after deposition with a Sartorius MC5 microbalance with 0.001 mg precision. ImageJ [58] was used to measure substrate area from post-deposition photographs. Thickness measurements were taken from SEM images at the substrate center. Since density measurements depend on thickness, the Ar-assisted results must be interpreted with caution since there will be some variation in film thickness across the substrate due to non-uniformities in argon flux. The film density measurements of unassisted films fabricated at normal incidence were normalized to bulk density.

The normalized densities of the films grown at $\alpha = 85^\circ$ are presented in Table 3.3. Here, the density values obtained both through VASE (where avail-

able) and mass measurement were normalized to the samples grown at α = 0°. For the unassisted samples, the values obtained from the two methods are in close agreement, whereas there are larger discrepancies between the two methods for the Ar-assisted samples. However, in nearly all cases, the normalized density is higher in the Ar-assisted samples than in the unassisted samples. This behaviour is consistent with IBAD densification observed for non-GLAD films [93–95]. The only exception to this trend is TiO_2, which shows an inconsistency between the VASE measurements (densification) and the mass measurement (density decrease). Thickness non-uniformity (discussed later) may be the source of this discrepancy.

Film crystallinity, as determined by XRD, is also shown in Table 3.2. The Ar-assisted process did not influence the film growth process to alter crystallinity for the materials studied here. An interesting link between the normalized film density ρ and film crystallinity was observed. Most materials were amorphous or polycrystalline, with the exception of CaF_2 which was textured. When ρ of the normal incidence films are compared to the crystallinity of the samples (Table 3.2), there is a trend where the amorphous samples have larger ρ than the polycrystalline and textured materials, with the exception of Al_2O_3. This is likely because the crystalline grain growth in the polycrystalline and textured films will produce voids in the film at the grain boundaries.

While the increase in film density can be useful in making desirable film property modifications, it can present challenges in obtaining accurate film models with the VASE method. When modeling porous columnar films with the VASE method, it is important that the column material density and com-

Table 3.2. *Bulk density of source material and density of GLAD films. ρ values are for $\alpha = 0^\circ$ films normalized to bulk density.*

Material	Crystallinity	Bulk Density	Film Density			
			$\alpha = 0^\circ$		$\alpha = 85^\circ$	
			0 mA	ρ	0 mA	5 mA
		[g cm^{-3}]	[g cm^{-3}]		[g cm^{-3}]	[g cm^{-3}]
Al_2O_3	Amorphous	3.95	2.80	0.71	0.77	1.15
CaF_2	Textured	3.18	1.62	0.51	0.19	0.35
ITO	Polycrystalline	7.17	4.27	0.60	1.94	2.11
MgF_2	Amorphous	3.15	2.87	0.91	0.66	1.20
Nb_2O_5	Amorphous	4.60	4.51	0.98	1.06	2.14
SiO	Amorphous	2.13	2.17	1.02	0.44	0.91
SiO_2	Amorphous	2.20	2.14	0.97	0.47	0.73
SnO_2	Polycrystalline	6.95	5.06	0.73	1.67	3.41
Ta_2O_5	Amorphous	8.20	7.46	0.91	1.57	3.33
TiO_2	Amorphous	4.23	3.73	0.88	1.34	1.10
Y_2O_3	Polycrystalline	5.01	3.58	0.71	0.82	1.62
ZrO_2	Polycrystalline	5.68	4.42	0.78	0.94	1.24

position matches the solid film grown at normal incidence. Since Ar-assisted deposition has been shown to increase film density, it may create complications in VASE modeling when the density of the normal incidence film, which is used to obtain the base material model, is significantly lower than the bulk material density. When this occurs, there is potential for larger modifications to the column material density through Ar-assisted deposition since there is greater void space for mobile surface atoms to fill. With the exception of Al_2O_3, in Table 3.2 the amorphous samples have a higher normalized density than the polycrystalline samples. This may contribute to the difficulty in modeling the polycrystalline results with the VASE. However, later discussion will suggest a different growth behavior for polycrystalline films, so there may be more than one factor responsible.

In the Ar-assisted samples, the non-uniformity in argon dose discussed in Chapter 2 leads to a thickness non-uniformity over the substrate. Since the film volume is required to obtain the mass-based film density measure-

Table 3.3. *Film density in GLAD films grown at* 85° *normalized to* $\alpha = 0^\circ$ *films. Errors in film density are expected to be less than 5%.*

Material	0 mA		5 mA	
	$\rho_{(VASE)}$	$\rho_{(Mass)}$	$\rho_{(VASE)}$	$\rho_{(Mass)}$
Al_2O_3	0.27	0.27	0.41	0.41
CaF_2	0.10	0.12	0.19	0.22
ITO	-	0.46	-	0.49
MgF_2	0.24	0.23	0.43	0.42
Nb_2O_5	0.22	0.23	0.40	0.47
SiO	0.16	0.20	0.30	0.42
SiO_2	0.20	0.22	0.51	0.34
SnO_2	-	0.33	-	0.67
Ta_2O_5	0.19	0.21	0.42	0.45
TiO_2	0.31	0.36	0.35	0.31
Y_2O_3	0.22	0.23	-	0.45
ZrO_2	0.20	0.21	-	0.28

ments, this thickness non-uniformity makes it difficult to obtain a characteristic film thickness to apply in the film density calculation. As a result, the mass-based film density values presented in Table 3.3 must be treated with caution. Suggestions for reducing the measurement error in future studies will be discussed later in this chapter.

Further experiments on Ar-assisted SiO_2 films were performed to investigate the effect of deposition angle on the modification of film density. Film density values of slanted post SiO_2 films were obtained from VASE measurements and are presented in Table 3.4. Here, film density values are normalized to a film deposited at normal vapour incidence. The data in Table 3.4 indicates an increase in ρ with increasing argon current, with a larger effect in the film grown at 85° than at 70°. This would imply that the more open void structure in the film grown at $\alpha = 85^\circ$ will enable better penetration of argon into the pores and enhance the redistribution of surface atoms by sputtering. This also supports the earlier argument that film materials which deposit as a more porous structure at normal incidence will undergo a larger change in

Table 3.4. *Normalized film density in Ar-assisted slanted post silicon dioxide films. In both the* 70° *and* 85° *cases, normalized film density increases with increasing argon current.*

	70°	85°
0 mA	0.56	0.20
5 mA	0.66	0.51

density with Ar-assistance and will be more prone to complications in VASE modeling.

3.4 Column Tilt Angle

The influence of Ar-assisted deposition on the column tilt angle β was also investigated. Prior studies have investigated column tilt angle in obliquely deposited films, focusing on the effect of surface diffusion. Lichter and Chen's model [96] predicts an increase in β with increasing diffusion. Fujiwara *et al.* also predicts an increase in β with increasing diffusion (substrate temperature) [97]. However, for iron films, they report an increase in β with increasing substrate temperature only between 500 K - 700 K. At higher temperatures, this trend saturates and no further increase in β is observed. At lower temperatures, from 300 K - 500 K, β decreases with increasing substrate temperature.

The modification of column tilt angle with argon bombardment was simulated with SIMBAD [24, 98]. SIMBAD is a two-dimensional thin film deposition simulator which incorporates variable adatom mobility and ion bombardment. Slanted post films were simulated with increasing bombardment. A periodically patterned substrate was used to achieve a more uniform and

measureable columnar structure. These simulations, presented in Fig. 3.1, show an column tilt angle increase from 61° to 65° with increasing bombardment.

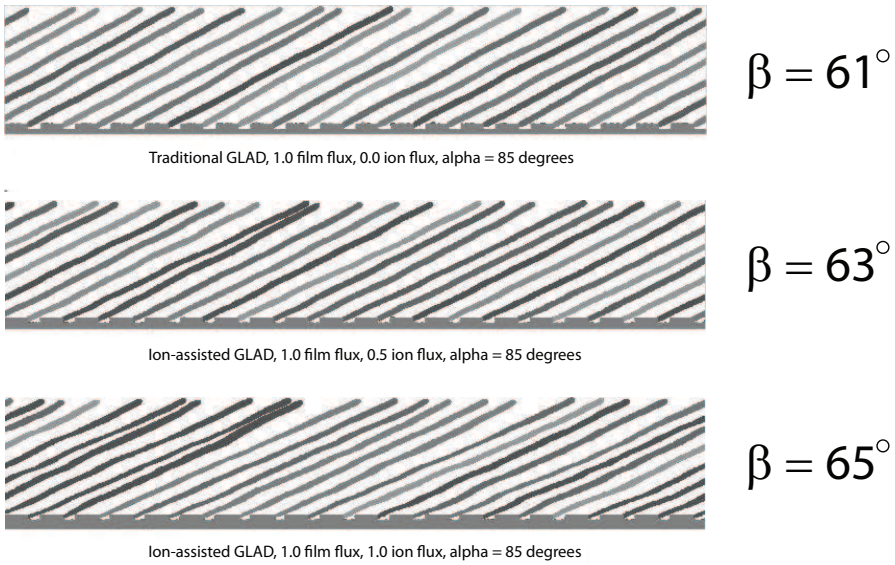

Figure 3.1. *SIMBAD simulations of slanted post GLAD films fabricated with varying degrees of ion flux.*

Modification of column tilt angle with Ar-assisted deposition is shown in Table 3.5. Here it is shown that for all materials studied, β increases with Ar-assistance, which agrees with the limited earlier work [99].

Selected SEM images illustrating column tilt angle modification in CaF_2 and SnO_2 films are shown in Fig. 3.2. The full set of SEM images can be found in Appendix C. CaF_2 was chosen because it was observed to have the lowest unassisted tilt angle and the largest normalized increase in tilt angle with Ar-assistance. SnO_2 was chosen because it was observed to have both the largest Ar-assisted tilt angle and the largest overall increase in tilt angle.

Table 3.5. *Column tilt angle β of unassisted and Ar-assisted GLAD films.*

Material	β		$\Delta\beta$
	0 mA	5 mA	
	[Degrees]	[Degrees]	[Degrees]
Al_2O_3	51.9 ± 0.3	62.3 ± 0.2	10.4±0.4
CaF_2	20.9 ± 0.6	35.0 ± 1.0	14.1±1.2
ITO	41.5 ± 0.6	44.9 ± 0.5	3.4±0.8
MgF_2	63.2 ± 0.4	68.9 ± 0.3	5.7±0.5
Nb_2O_5	56.3 ± 0.6	68.4 ± 0.6	12.1±0.8
SiO	45.4 ± 0.9	60.9 ± 0.4	15.5±1.0
SiO_2	44.1 ± 1.2	61.2 ± 0.3	17.1±1.2
SnO_2	48.4 ± 0.5	69.2 ± 0.6	20.8±0.8
Ta_2O_5	52.9 ± 0.6	68.7 ± 0.5	15.8±0.8
TiO_2	51.0 ± 0.3	67.7 ± 0.2	16.7±0.4
Y_2O_3	52.4 ± 0.4	65.5 ± 0.8	13.1±0.9
ZrO_2	57.0 ± 0.4	58.5 ± 0.3	1.5±0.5

The dependence of column tilt angle on argon flux was also investigated and is shown in Fig. 3.3. Here, β is shown to increase with Ar-assistance with a monotonically increasing dependence. It is also interesting to note that for the silicon data by Fleischauer *et al*. [83], the beam voltage has a negligible effect on β. This is likely due to a relatively constant sputter yield over the voltage range used. It should be noted here that the Si film data refers to films grown on periodically patterned substrates so the absolute values of β for these films may deviate from a film grown on an unpatterned substrate with otherwise equivalent deposition conditions.

Fig. 3.4 shows TiO_2 films grown at different material deposition rates with a variety of argon flux rates. The samples grown at $1.0\ \mathrm{nm/s}$ were all grown as separate films, whereas the sample set grown at $0.7\ \mathrm{nm/s}$ was grown as a single film deposition and were analyzed at different substrate locations. Here, the non-uniformity in the argon flux allows multiple argon to film flux ratios to be achieved in a single film deposition. Both film sets are observed to increase with increasing argon flux. The column tilt angle measurements

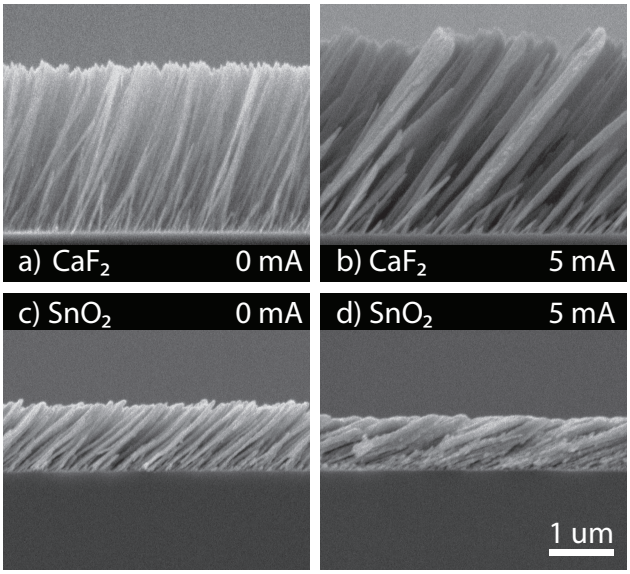

Figure 3.2. *SEM images of calcium fluoride and tin oxide slanted post films fabricated with the Ar-assisted GLAD process. Reproduced with permission from Sorge* et al. *[61].*

taken at different substrate locations in the $0.7\ \mathrm{nm/s}$ sample set follows a statistically highly significant (calculated P = 0.0001) [100] linear relationship. The data in Fig. 3.4 shows larger column tilt angles are achievable with larger film flux rates. For equivalent argon flux rates, this would imply that larger column tilt angle values are obtained when the ratio of film flux to argon flux is larger. If the sputter rate is assumed to be linear with argon dose, this finding would suggest that sputtering is not the dominant factor in modifying column tilt angle. However, it is difficult to completely rule out the influence of sputtering without further studies which completely isolate the effects of sputtering and surface diffusion from each other.

A relationship between $\Delta\beta$ and unassisted β is shown in Fig. 3.5. When the materials are grouped according to their crystallinity, material indepen-

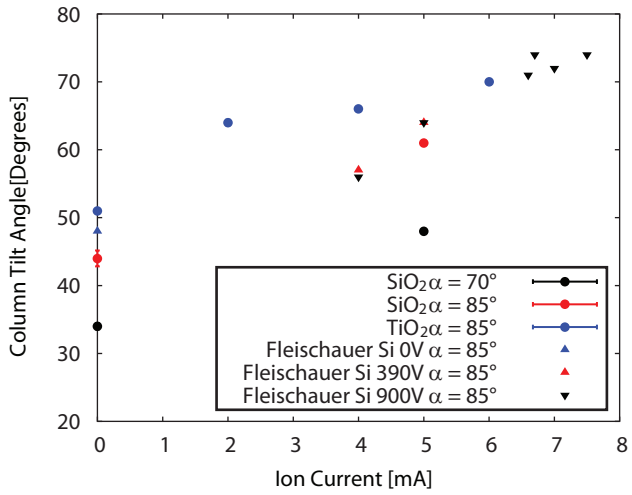

Figure 3.3. *Column tilt angle dependence in Ar-assisted slanted post films. Error bars are obstructed by the data points. Reproduced with permission from Sorge and Brett [91].*

dent trends begin to emerge. The amorphous samples show a statistically significant (P = 0.02) linear relationship between $\Delta\beta$ and unassisted β. The textured CaF_2 sample is within error of the amorphous trend. If the textured CaF_2 sample is included in the dataset, the linear relationship becomes statistically highly significant (P = 0.004, solid line). For polycrystalline samples, neglecting ITO, the remaining three data points also form a statistically significant linear trend (P = 0.03, dashed line). However, no firm conclusion may yet be drawn from the polycrystalline fit, as only 3 data exist. Moreover, the exclusion of ITO is based on SEM images that lead us to believe vapour phase condensation is occurring during deposition. Specifically, the material flux may be arriving at the substrate as agglomerations of material rather than individual molecules. If ITO is experiencing an atypical process, verifying a general trend from the polycrystalline data will require additional data.

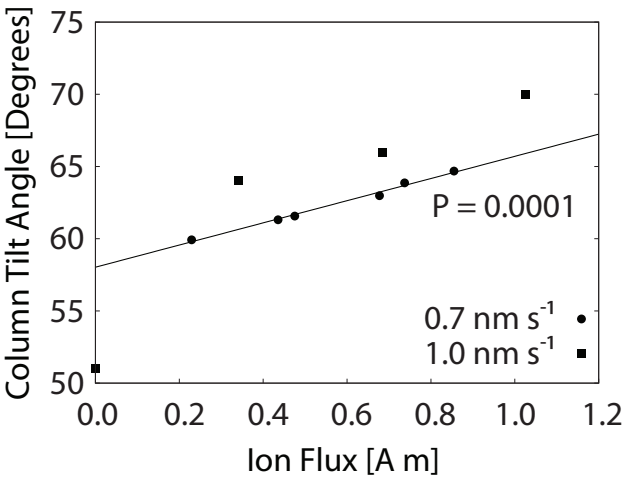

Figure 3.4. *Column tilt angle dependence in Ar-assisted slanted post TiO_2 films. Column tilt angle values are larger for films fabricated with larger deposition rates. Reproduced with permission from Sorge and Brett [91].*

3.4.1 Phisweep Substrate Motion

This section examines the effect of the phisweep advanced substrate motion used in conjunction with the Ar-assisted deposition process. Discussion will focus on modifications to column tilt angle and film density and comparisons with trends predicted for unassisted phisweep films.

In a prior study by Jensen *et al*. [28], the phisweep substrate motion algorithm has been shown to prevent column broadening. This has been useful in achieving high structural fidelity over large film thicknesses which is vital in the fabrication of thin film photonic bandgap materials. However, a consequence of using the phisweep algorithm is a reduction in column tilt angle which is dependent on the phisweep angle γ. Thus, for Ar-assisted phisweep GLAD, there exist competitive effects of increasing tilt (Ar-assistance) and decreasing tilt (phisweep). An expression for the effective column tilt angle β_{PS}

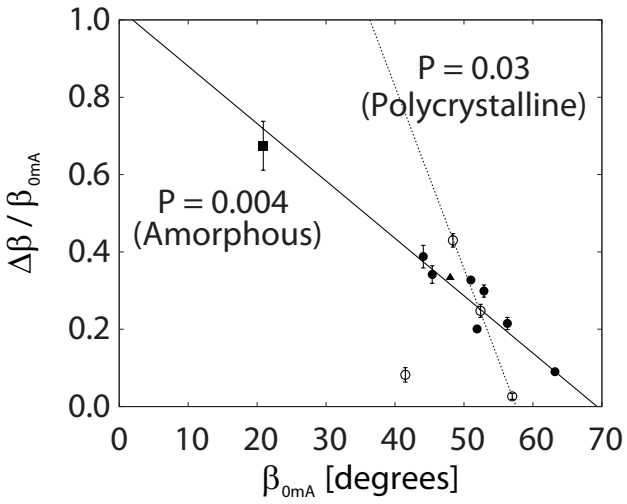

Figure 3.5. *Dependence of column angle increase ratio on unassisted column angle and sample crystallinity (Amorphous - solid circles, Amorphous Si from [83] - solid triangle, Textured - solid square, Polycrystalline - open circles).*

in an unassisted GLAD film, reported by Gish *et al*. [101], is given empirically in Eq. 3.1. β_{TG} corresponds to the column tilt angle of a film grown at a given deposition angle with zero substrate sweep.

$$\tan \beta_{PS} = \tan \beta_{TG} \cos \gamma. \tag{3.1}$$

Ar-assisted silicon dioxide films were grown with a $25\ \mathrm{nm}$ sweep pitch phisweep process to determine whether these films would follow a trend with sweep similar to the unassisted trend given in Eq. 3.1. Figs. 3.6 and 3.7 illustrate the effects of using different phisweep angles while maintaining constant argon bombardment of $5\ \mathrm{mA}$. The experimental results in Fig. 3.6 follow the modeling prediction of Gish *et al.* when β_{TG} is represented by the experimentally observed Ar-assisted column tilt angle at $\gamma = 0°$. Fig. 3.7 does not indicate any clear dependence of the film density on the phisweep angle

for fixed argon bombardment conditions. The effect of the phisweep angle on film density is expected to be small, but some deviation in film density is observed for the films grown at $85°$. This deviation in film density is expected to be due to variations in the argon conditions in each of the depositions rather than changes in the phisweep angle. These two figures suggest a similar influence of the phisweep motion on Ar-assisted films as with unassisted films. The findings enable predictions to be made on the resulting column tilt angle and film density of Ar-assisted phisweep films without requiring the development of any additional theory. Furthermore, they demonstrate that the combined use of phisweep and argon bombardment gives very precise control of column tilt over a wide range of values.

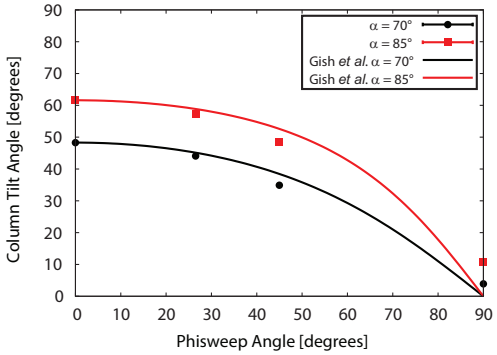

Figure 3.6. *Column tilt angle dependence in phisweep silicon dioxide* $5\ \mathrm{mA}$ *Ar-assisted slanted post films. Solid lines indicate predicted tilt angles. Error bars are obstructed by the data points.*

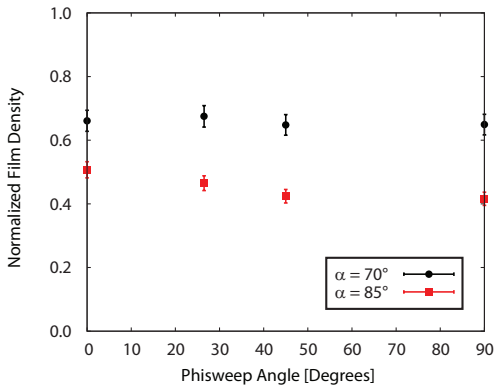

Figure 3.7. *Normalized film density dependence in phisweep silicon dioxide Ar-assisted slanted post films. Density remains relatively constant over the entire range of phisweep angles. Reproduced with permission from Sorge and Brett [91].*

3.5 Refractive Indices

3.5.1 Slanted Post Films

The Ar-assisted slanted post structures, like their unassisted counterparts, exhibit an anisotropy in column cross-section and thus are biaxial. This optical anisotropy is of interest in optical filtering applications [102–105]. Characterization of in-plane birefringence of Ar-assisted phisweep silicon dioxide samples obtained with VASE measurements is shown in Fig. 3.8. The in-plane birefringence is defined by Eq. 3.2 [106] with principal refractive indices defined in Fig. 3.9.

$$\Delta n = n_y - n_p = n_y - \left(\frac{\sin^2 \beta}{n_z^2} + \frac{\cos^2 \beta}{n_x^2} \right)^{-1/2} . \tag{3.2}$$

In a traditional inorganic slanted post GLAD film, the in-plane birefringence tends to be positive since the dominant planar refractive index corresponds to the index which is normal to the deposition plane (n_y). This domi-

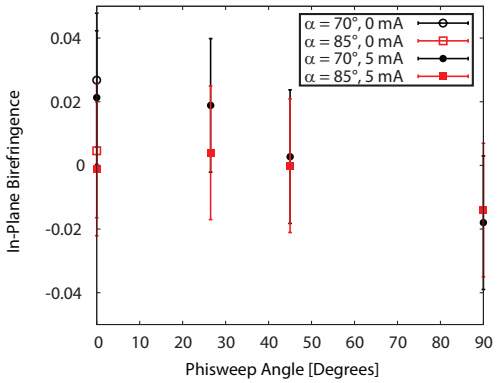

Figure 3.8. *In-plane birefringence dependence on phisweep angle in Ar-assisted silicon dioxide films. Reproduced with permission from Sorge and Brett [91].*

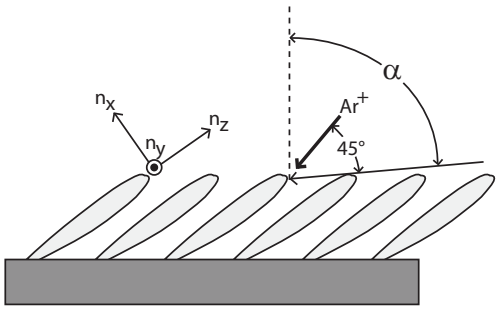

Figure 3.9. *Principal indices in obliquely deposited slanted post thin films.*

nant index is commonly designated to be oriented in the column broadening direction. When the column tilt angle is increased through argon assistance, the orthogonal planar refractive index n_p increases due to an increase in the planar cross-section of the column in that direction. This results in an overall decrease in the in-plane birefringence, as observed in Fig. 3.8 when Ar-assisted slanted post films are compared to unassisted slanted post films at $\gamma = 0°$. As the phisweep angle is increased, two different processes are occurring. First, the column tilt angle is decreasing according to Eq. 3.1, which reduces the contribution of n_z to the n_p planar index. Second, as the sweep

angle is increased, the effective column broadening direction evolves such that at $\gamma = 90^\circ$ the broadening direction is orthogonal to the original $\gamma = 0^\circ$ position. This results in a gradual shift of the in-plane birefringence from a positive to negative value as the phisweep angle is increased. However, at $\gamma = 90^\circ$, the magnitude of the in-plane birefringence is still smaller than that of an unassisted slanted post film. Thus, the phisweep films do not exhibit any increase in magnitude of the in-plane birefringence at the argon conditions studied.

The principle refractive indices and in-plane birefringences for many optical materials as measured by VASE (where available) are presented in Table 3.6. In all cases, the refractive indices are larger for the Ar-assisted samples. This is due to the Ar-assisted films' increased film density. The dependence of the change in the in-plane birefringence normalized to the bulk refractive index) on the change in column tilt angle for amorphous samples is shown in Fig. 3.10. The data in Fig. 3.10 shows a general trend of decreasing normalized in-plane birefringence with increasing change in column tilt angle. The in-plane birefringence changes polarity in Fig. 3.10 because the column tilt angle is increasing enough such that the planar refractive index which is governed by column tilt becomes larger than the planar index in the column broadening direction. This effect is illustrated in Fig. 3.11.

3.5.2 Serial Bi-Deposited Films

A set of titanium dioxide films were grown using a serial bi-deposition substrate motion algorithm with a $25\ \mathrm{nm}$ sweep pitch to determine how the degree of argon assistance affects the structural anisotropy. A serial bi-deposition

Table 3.6. *Principal refractive indices of unassisted and Ar-assisted GLAD films.*

Material	0 mA				5 mA				Crystallinity
	n_x	n_y	n_z	Δn	n_x	n_y	n_z	Δn	
Al_2O_3	1.12	1.16	1.20	-0.007	1.23	1.25	1.26	-0.003	Amorphous
CaF_2	1.02	1.02	1.03	-0.002	1.04	1.04	1.05	-0.002	Textured
ITO	-	-	-	-	-	-	-	-	Polycrystalline
MgF_2	1.07	1.09	1.10	-0.008	1.16	1.16	1.16	-0.002	Amorphous
Nb_2O_5	1.22	1.24	1.25	-0.003	1.41	1.45	1.59	-0.106	Amorphous
SiO	1.10	1.11	1.13	-0.0003	1.22	1.23	1.23	0.002	Amorphous
SiO_2	1.11	1.11	1.10	0.003	1.20	1.24	1.25	-0.003	Amorphous
SnO_2	-	-	-	-	-	-	-	-	Polycrystalline
Ta_2O_5	1.16	1.19	1.21	-0.001	1.30	1.49	1.59	-0.05	Amorphous
TiO_2	1.27	1.39	1.49	0.000	1.34	1.43	1.55	-0.083	Amorphous
Y_2O_3	1.13	1.15	1.17	-0.005	-	-	-	-	Polycrystalline
ZrO_2	1.13	1.18	1.23	-0.02	-	-	-	-	Polycrystalline

substrate motion algorithm was chosen to isolate the effects of changing film density since the resulting microstructures are vertical posts and the column tilt angle will not change. The dependence of the film density normalized to films grown at $\alpha = 0^\circ$ on the argon current is shown in Fig. 3.12. At deposition angles of 70° and 85° the normalized film density steadily increases with increasing argon current. This is consistent with the prior result on Ar-assisted slanted post films discussed earlier. The dependence of the three primary indices on the argon current at deposition angles of 70° and 85° is shown in Fig. 3.13. All three indices tend to increase with increasing argon current which is indicative of densification along all axes.

3.6 Surface Area

Surface area measurements were obtained for all samples in Table 2.1. Adsorption isotherms for unassisted and 5 mA Ar-assisted Al_2O_3, ITO, SiO_2, and TiO_2 films are shown in Fig. 3.14 as an example of the data collected. Isotherms of the other materials are shown in Appendix B. The lower vol-

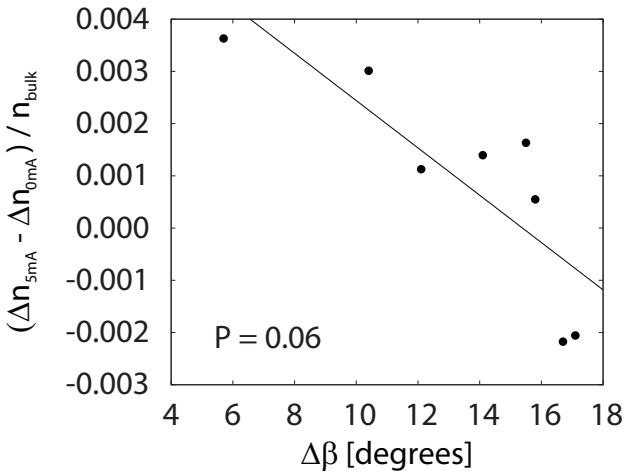

Figure 3.10. *Dependence of the change in normalized in-plane birefringence on increase in column angle for amorphous materials.*

ume of gas adsorbed by the $5\ \mathrm{mA}$ TiO_2 Ar-assisted film indicates a lower surface area than the unassisted TiO_2 film. Specific surface area (SSA, $\mathrm{m^2 g^{-1}}$) and surface area enhancement (SAE, $\mathrm{m^2 m^{-2} \mu m^{-1}}$) results are shown in Table 3.7. For the SAE measurement, the thickness used in the calculation was taken from the substrate center. In all cases, SSA is reduced by Ar-assisted deposition, whereas there is no clear trend in the case of SAE. The reduction in SSA with Ar-assisted deposition is likely due to smoothing of the column surfaces and densification of the film.

Reliable surface area measurements require high sensitivity krypton gas and large substrate areas. Thus, surface area values reported are averages over half of a $10\ \mathrm{cm}$ diameter silicon wafer, and film and argon beam nonuniformities become significant; first, the film growth rate varies across the substrate, and second, the argon flux distribution across the substrate is not uniform. The slanted post model from Wakefield and Sit [60] was used to determine the thickness error measurement to be less than 5%. Therefore, SSA

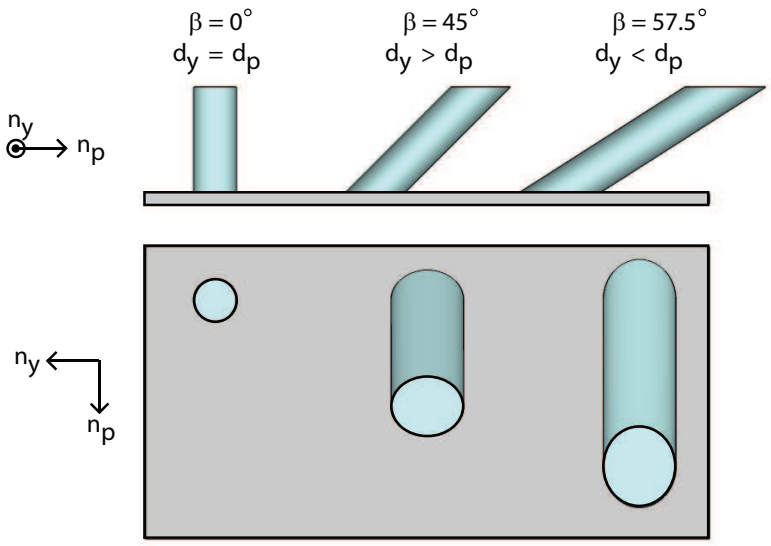

Figure 3.11. *In-plane column cross-section for slanted posts of different tilt angles.*

and SAE results for unassisted films are expected to be accurate. However, non-uniformity in argon flux distribution requires caution in interpreting the SSA and SAE results for the $5\ \mathrm{mA}$ Ar-assisted films.

Since the SSA measurements are calculated using the total material mass deposited as opposed to the film thickness, the SSA measurements presented are able to be interpreted as an average surface area value which accounts for the total argon dose present across the substrate in the Ar-assisted samples. Although the SSA cannot be obtained for specific points on the substrate in the Ar-assisted samples, the current SSA measurements allow for general comparisons to be made between the unassisted and Ar-assisted sample sets.

SAE measurements on the Ar-assisted samples are more problematic since the film thickness factors into the calculation. While it does not represent the average film thickness, the thicknesses used in the SAE measurements were

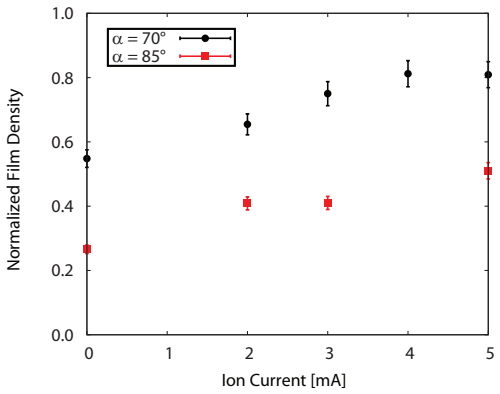

Figure 3.12. *Normalized film density in Ar-assisted serial bi-deposited titanium dioxide films. Reproduced with permission from Sorge and Brett [91].*

taken from substrate center for consistency. When the thickness profile from Chapter 2 and the predictions of Wakefield and Sit for slanted post films are taken into account, variation in film thickness across a silicon wafer can be as much as 50%. Without complete understanding of the full thickness profile in the Ar-assisted films, a reliable value which accurately represents the average film thickness remains elusive. This makes it difficult to state conclusive trends since many competing factors are present such as increased film density, reduction in film thickness and reduced column surface area. However, surface area measurements on Ar-assisted GLAD samples have not yet been reported, thus it is useful to include the Ar-assisted SAE results as a first order estimate.

The accuracy of thickness-based measurements can be improved by reducing the argon flux non-uniformity. Reducing this non-uniformity would result in thickness measurements which are more representative of the average film thickness. Improving film thickness uniformity can be accomplished in two ways. First, reducing the substrate size will result in a more uniform

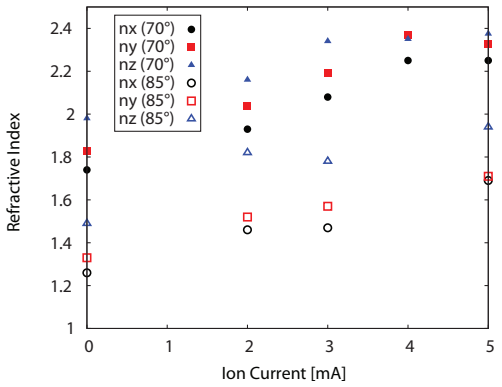

Figure 3.13. *Principle index values at 528 nm wavelength in serial bi-deposited Ar-assisted titanium dioxide thin films. Reproduced with permission from Sorge and Brett [91].*

film growth since less of the non-uniform argon flux will be intercepted. This method has the potential to substantially increase the utility of using a single thickness measurement as being representative of the thickness across the entire substrate. However, reducing the substrate area is a tradeoff since it would increase the error in measurement of substrate area and film mass.

To improve both SAE and mass-based film density measurements, larger argon throw distances can be used. This would effectively achieve the same reduction in argon flux non-uniformity, but allow for larger substrates to be used. However, increasing the argon throw distance would reduce the argon flux arriving at the substrate so the output of the argon source would need to be increased to compensate. This method would also necessitate the use of a larger vacuum chamber to accommodate the larger argon throw distance.

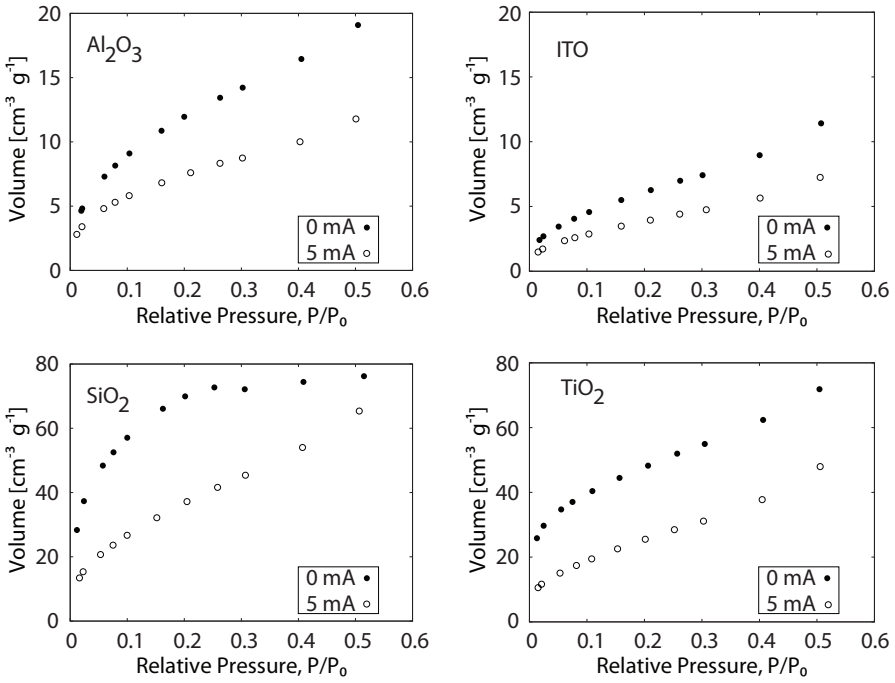

Figure 3.14. *Adsorption isotherms of aluminum oxide (Top-Left), indium tin oxide (Top-Right), silicon dioxide (Bottom-Left), and titanium dioxide (Bottom-Right) films grown unassisted and with 5 mA Ar-assistance.*

3.7 Conclusion

The results in this chapter demonstrate how Ar-assisted deposition can be used to produce film morphologies which are unique from unassisted obliquely deposited films. The incorporation of Ar-assistance during film growth was shown to influence numerous film properties.

Studies on film density indicate that Ar-assisted deposition causes film density to increase. This modification is more pronounced in films grown at higher deposition angles since unassisted films have higher porosity in this range. As a result, the material is less efficiently packed which allows for larger increases in film density when an Ar-assisted process is used. Addi-

Table 3.7. *Specific surface area (SSA) and surface area enhancement (SAE) of unassisted and Ar-assisted GLAD films.*

Material	SSA		SAE	
	0 mA	5 mA	0 mA	5 mA
	[m^2g^{-1}]	[m^2g^{-1}]	[$m^2m^{-2}\mu m^{-1}$]	[$m^2m^{-2}\mu m^{-1}$]
Al_2O_3	55	35	42	39
CaF_2	50	45	10	17
ITO	30	20	61	42
MgF_2	135	80	90	96
Nb_2O_5	80	60	85	127
SiO	250	130	108	117
SiO_2	225	185	107	135
SnO_2	15	13	24	45
Ta_2O_5	50	40	77	128
TiO_2	220	130	291	150
Y_2O_3	50	20	40	32
ZrO_2	115	85	106	103

tional studies on unassisted films grown at normal incidence indicate that in most cases, when normalized to bulk density, amorphous films deposit with higher density than polycrystalline films. This can cause complications in VASE modeling of polycrystalline Ar-assisted samples since the bulk material property in the films is more susceptible to densification from the Ar-assisted process.

In addition to modifying the film density, Ar-assistance can also modify the column tilt angle in slanted post films. Here, column tilt angle was observed to increase with Ar-assistance for all materials studied. In addition, the column tilt angle was observed to increase with argon dose whereas the argon energy was only observed to have a minor influence. The tilt angle was also observed to be dependent on the Ar-film flux ratio. However, the column tilt angle was observed to increase when the film flux was increased, making the total system energy higher, but the Ar-film flux ratio lower. This suggests that surface diffusion is the dominant mechanism in this case. A

material independent trend in amorphous films was observed where the Ar-assisted increase in column tilt, normalized to the unassisted column tilt, is linearly dependent on the unassisted column tilt angle.

Investigation of Ar-assisted deposition in conjunction with advanced substrate motion algorithms shows that the influence of substrate motion follows similar trends as observed in unassisted films. In Ar-assisted phisweep depositions, the column tilt angle was observed to decrease as the phisweep angle is increased and approaches zero column tilt when the substrate motion approaches the serial bi-deposition case (phisweep angle of 90°). Film density measurements indicate no significant change in density when the phisweep angle is altered. Instead, the film density is determined by the argon dose and incident deposition angle.

The changes observed in film density and column tilt angle result in changes in the optical properties observed in Ar-assisted films. Since Ar-assistance increases film density, the principal refractive indices are observed to increase. This was found in both slanted post films and serial bi-deposited films. Although the principal refractive indices were found to increase in Ar-assisted slanted post films, the in-plane birefringence was found to decrease and change polarity with increasing argon flux. This suggests that the in-plane column cross-section is changing with argon flux.

Modification of surface area with Ar-assisted deposition was also investigated. The specific surface area was observed to decrease with Ar-assistance for a number of materials. This is most likely due to column surface smoothing and film densification. However, the surface area enhancement showed no clear trend between unassisted and Ar-assisted films. This is likely due to

the difficulty in obtaining uniform Ar-assisted samples over large substrate areas. To alleviate this issue, future studies should incorporate larger argon throw distances to improve argon flux uniformity.

These results collectively show that the Ar-assisted process combined with the advanced substrate motion algorithms provide a good toolset for the fabrication of columnar films with morphologies that are unachievable with an unassisted process. These new morphologies will be utilized in the following chapters which focus on applications of the Ar-assisted process.

Chapter 4

Argon-Assisted Square Spiral Photonic Bandgap Materials

4.1 Introduction[1]

With the world's data consumption rapidly increasing, there is a global demand for improvements in data processing and data transfer. The incorporation of optical devices into these technologies is becoming more and more common. Photonic bandgap materials have the potential to vastly reduce the physical dimensions of these optical devices by providing extremely compact waveguiding capabilities, allowing them to be utilized in applications where device size is critical.

The optical properties and applications of one-dimensional periodic dielectric structures have been extensively studied for more than a century [108]. It would be approximately 90 years after this first report on periodic dielectric materials before materials with higher dimensional periodicities

[1] Portions of this chapter have been published in [107]

would be studied [109,110]. Subsequently, the work of Yablonovitch and John in 1987 [111,112] on three dimensional photonic crystals catalyzed enormous efforts on two and three dimensional periodic dielectric structures.

Today, commercial applications for periodic dielectric materials are varied and are dependent on the degree of periodicity in the material. One dimensional periodic dielectric materials are most commonly used in high reflectivity mirrors and reflectors and are used in virtually all modern optical experiments. The largest commercial applications of periodic dielectric materials with higher order periodicity is currently in photonic crystal fibres [113]. Traditional optical fibres use total internal reflection to confine electromagnetic waves to the fibre to provide waveguiding capabilities. In traditional optical fibres the two main constituents, the core and cladding, are unpatterned. In order to produce total internal reflection, the core has a higher refractive index than the cladding material. In photonic crystal fibres, the cladding is periodically patterned outward from the core to create a two-dimensional photonic bandgap which restricts light within that band from propagating inside the cladding, thus confining it to the core. By incorporating a cladding that is patterned in two dimensions, which extends outward from the core and runs along the entire fibre, the light confinement is based on reflection due to periodically structured boundaries and is no longer reliant on total internal reflection. This removes the requirement of a high refractive index core. As a result, the core in a photonic crystal fibre can be completely hollow [114]. Since more optical power can be sent through a hollow core than through glass, the use of a hollow core could increase the capacity of photonic waveguides by a factor of 100 when compared to conventional telecommunications fibres, as stated by Yablonovitch [115].

While many applications have been proposed for three dimensional photonic crystals, the significant challenge in fabricating such structures has limited their commercializability so far. As a result, significant effort has been invested into the fabrication of periodic materials with full three-dimensional photonic bandgaps. To date, there have been numerous proposed photonic crystal architectures which each have their advantages and disadvantages. Before these different architectures are discussed in depth, it is useful to quickly outline the numerous factors which require consideration when fabricating three-dimensional photonic crystal structures.

- Bandgap Size

  The bandgap size is the wavelength range that is restricted from propagating inside the periodically structured material. It is commonly defined as the relative bandgap, which is the actual bandgap width normalized to the central bandgap wavelength. The relative bandgap is a metric which is used to determine the information carrying capacity in a photonic crystal network.

  The bandgap size depends on two main factors. The first is the lattice type. In order to obtain a full three-dimensional photonic bandgap it is insufficient to have a bandgap in all directions. In addition, these bandgaps must all overlap at the same wavelength in order to establish a full bandgap at that wavelength. In order to maximize the overlap of the individual bandgaps to optimize the width of the full bandgap, the Brillouin zone of the three-dimensional crystal would ideally be spherical. However, no three dimensional crystal contains an ideal spherical Brillouin zone.

The Brillouin zone refers to the primitive cell of the reciprocal lattice. The reciprocal lattice is a representation of the direct lattice in momentum space, which is the Fourier transform of the spatial lattice. In general, the Brillouin zone of three dimensional crystals is a polygonal solid. This means that there is no perfect overlap between the individual bandgaps and that the bandgaps in different directions will occur at different frequencies. Of all the possible three-dimensional lattices, the Brillouin zone of the face-centered-cubic (FCC) lattice is the most spherical and is the most independent of the spatial direction [116]. This means that the FCC lattice will provide the best overlap of the individual bandgaps which will maximize the bandgap size. As a result, the vast majority of proposed photonic crystal architectures are based on an FCC lattice.

- Refractive Index Contrast

  Once an appropriate architecture is chosen to maximize the potential overlap of the individual bandgaps, a full bandgap can only be achieved with a sufficient refractive index contrast. By increasing the refractive index contrast, the width of the individual bandgaps increases. With an appropriate architecture chosen and a sufficiently large index contrast, the individual bandgap widths will be large enough to produce a full three-dimensional bandgap. Here it is important to note that even when the optimal FCC lattice is used, a full three-dimensional bandgap is not guaranteed. Since the Brillouin zone in the FCC lattice is not perfectly spherical, the individual bandgaps do not perfectly overlap and occur at different frequencies in different directions. If the refractive in-

dex contrast too small, the individual bandgap widths will not increase enough to compensate for this and will not overlap in all directions, which will result in only a partial bandgap.

Most commonly, three-dimensional photonic crystal periodicity is generated with only one material, and air is used as the low index medium. In order to generate large photonic bandgaps, a high index material is chosen to maximize this refractive index contrast. However, in order to produce an effective device, the materials used in fabrication must not absorb in the wavelength region of operation. At telecommunication wavelengths, silicon and gallium arsenide are most commonly used as the high index material. Since both of these materials heavily absorb in the visible wavelength range, they are not suitable candidates for visible wavelength photonic crystals. Since titanium dioxide is transparent in the visible range and has a high refractive index, it is most commonly used as the high index material in photonic crystals designed for use in the optical wavelength range.

- Ease of Fabrication

  Once an architecture with a full theoretical bandgap has been chosen, the next step is fabrication. A more complex fabrication process will increase the difficulty in achieving high yield, which will ultimately determine the unit cost of a device. When considering the commercializability of three-dimensional photonic crystals, the unit cost will be one of the central factors. This means that architectures with less complex fabrication processes will tend to be more attractive.

There have been many different three-dimensional photonic crystal structures reported in the literature, each with their own fabrication process. These have ranged from relatively simple processes like self-assembly and film deposition to extensive lithography processes. These will be discussed in more detail later.

- Defect Fabrication

  In photonic crystal devices, the vast majority of interesting properties arise from the controlled incorporation of defects within the photonic crystal bulk. The inclusion of defects within the photonic crystal presents its own fabrication challenges which also need to be taken into account to determine the overall manufacturability. Currently, nearly all defect engineering involves some sort of lithographic process, which makes it difficult to incorporate defects in architectures with fabrication processes that are not lithographically compatible. The complexity in defect engineering in three-dimensional photonic crystal structures is currently one of the largest hurdles which is preventing widespread application of three-dimensional photonic crystal devices.

- Robustness

  Related to the ease of fabrication, another factor which must be considered is the film robustness. Here, robustness can have two different meanings. First, robustness can refer to the structural strength of the photonic crystal and its resistance to damage from both physical and chemical means. Second, robustness can refer to the photonic bandgap and its tolerance of imperfections in the fabricated structure. An architecture that is more robust in this sense will can have lower manufac-

turing precision, which would improve the ease of fabrication.

With the main fabrication challenges and considerations taken into account, it is now appropriate to discuss some of the more common three-dimensional photonic crystal structures and each of their strengths and weaknesses.

- Yablonovite

  The first three-dimensional photonic crystal structure to be experimentally realized was Yablonovite in 1991 [117]. The Yablonovite structure is fabricated by creating columnar voids with precise orientation at specific locations in high index dielectric material. The first experimentally realized Yablonovite was fabricated with centimetre-long feature sizes which produced a bandgap in the microwave range. The feature size has since been scaled down with x-ray lithography in polymethylmethacrylate resist to $1.3\ \mu\mathrm{m}$ [118]. While this produces a bandgap at $2.5\ \mu\mathrm{m}$, the use of resist drastically reduces the index contrast. Improvements would require some form of templating process, but this would complicate the fabrication procedure.

  In theory, Yablonovite contains a large relative bandgap which is highly robust, but fabrication of the Yablonovite structure with micron length feature sizes and appreciable refractive index contrast continues to be challenging. If the fabrication challenges can be overcome, the Yablonovite structure has the potential to be one of the strongest performing three-dimensional photonic crystal structures.

- Woodpile

  The next three-dimensional photonic crystal structure to be experimentally realized was the woodpile structure in 1998 [119]. The fabrication of the woodpile structure involves extensive lithography steps to produce stacked, crisscrossing polycrystalline silicon structures. Like the Yablonovite structure, the woodpile structure has a large and robust bandgap. In addition, these structures have been fabricated in high refractive index silicon, achieving suitable index contrast. However, the challenge in fabricating the woodpile structure increases with each successive lithographically patterned layer since they need to be tightly aligned with the previously fabricated layers.

  While it is challenging to fabricate woodpile structures with significant thickness, if this can be overcome, the incorporation of defects within the structure would be straight-forward. Even with this fabrication challenges, lasing behaviour in woodpile-based devices which incorporate point defects have been reported in gallium arsenide [120].

- Inverse Opal

  In 2000, the inverse opal structure was the next three-dimensional photonic crystal structure to be experimentally realized [121]. The fabrication of the inverse opal structure involves self-assembly of silicon dioxide spheres into an FCC lattice, and infilling with silicon. The silicon dioxide spheres are then etched away leaving an inverse backbone made of silicon.

  As a general rule, self-assembly and simple patterning methods usu-

ally have low refractive index contrast so further steps such as backfilling and template removal are necessary to improve the index contrast. Another example is in structures fabricated with holographic lithography. Here, high quality three-dimensional periodic structures are relatively easy to fabricate in photoresist, but fabricating these structures in materials containing higher refractive indices can prove to be quite challenging.

While the inverse opal structure has a relatively small theoretical bandgap that is less robust than most other commonly studied three-dimensional photonic crystal structures, the fabrication utilizes a self-assembly process to generate large scale periodicity which may prove to be a huge benefit in future manufacturing efforts. In addition, defect incorporation inside the bulk of the photonic crystal structure has been reported with two-photon polymerization [122].

- Square Spiral

  The square spiral structure was first experimentally realized in 2002 [6]. In this study, a two-dimensional periodic array of silicon square spiral columns was fabricated with the GLAD process on a pre-patterned substrate. Using this method, the fabrication of long-range ordered structures is fairly straightforward and the use of silicon enables a high index contrast. In addition, two-dimensional defects can easily be fabricated by modifying the pre-patterned substrate prior to deposition. However, creating linear and point defects has proven to be a challenge with the GLAD method.

An alternative method for fabricating square spiral structures involves a three-dimensional laser direct write lithography process [123]. Here, the fabrication of ordered arrays of square spirals are achieved in SU-8 resist. Using this method, defect fabrication is fairly straightforward, but the refractive index of SU-8 is insufficient to provide adequate index contrast. As a result, additional fabrication steps or templating must be performed to improve the index contrast.

The square spiral architecture has a moderately large and robust theoretical bandgap. While the fabrication of the square spiral structure with adequate refractive index contrast is fairly straightforward with the GLAD process and lithography-based methods are well suited for defect implementation, using these processes, it is difficult to simultaneously achieve both without complication.

This work focuses on the square spiral architecture, since GLAD films have been reported as promising candidates for three-dimensional photonic bandgap materials [6, 28, 124–126]. Utilizing photonic simulations, Toader *et al*. [125] proposed optimal periodic silicon square spiral films with corners that map out a diamond lattice by connecting nearest neighbours. The structures are commonly identified by the nth nearest neighbour that is connected and are referred to as diamond:n structures. The two structures that are of most interest are the diamond:1 and diamond:5 structures, (shown in Fig. 4.1) however, they are interesting for different reasons. The diamond:5 structure is significant because it represents the optimal direct square spiral structure, whereas the diamond:1 structure is less optimal in terms of the width of its bandgap. However, the diamond:1 structure has simplified fabrication re-

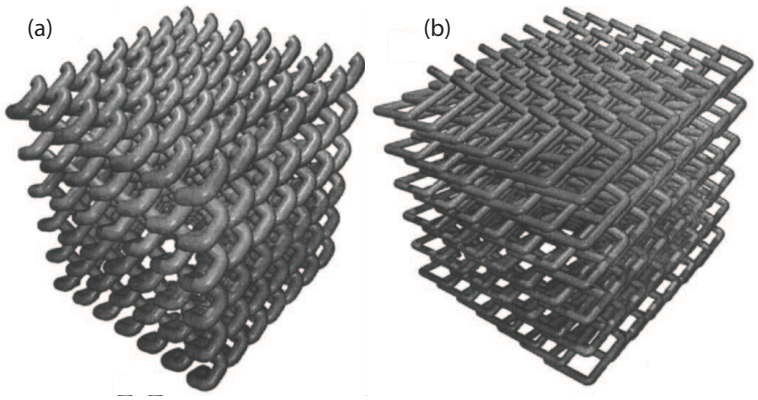

Figure 4.1. *Models of (a) diamond:1 and (b) diamond:5 structures. Reproduced with permission from Toader and John [125] ©2002 by the American Physical Society*

quirements due a lower arm angle, β (64° vs. 79°). The data in Table 3.5 indicated that at a deposition angle of 85°, most materials deposit with a column tilt angle that is less than the optimal value of $\beta = 64^\circ$ when an unassisted process is used. A silicon square spiral film grown with an unassisted GLAD process is shown in Fig. 4.2. The column tilt angle is 57°, 7° less than the optimal diamond:1 value of 64°. The results presented earlier on Ar-assisted film properties have shown that Ar-assisted deposition can be used to increase the column tilt angle for a number of materials. The focus of this chapter will be on the use of Ar-assisted deposition to fabricate three-dimensional square spiral photonic crystal structures with column tilt angles which match the optimal values predicted by theory.

4.2 Experimental Procedure

Full three-dimensional periodicity in the films presented in this chapter is achieved by substrate pre-patterning via electron beam lithography and pe-

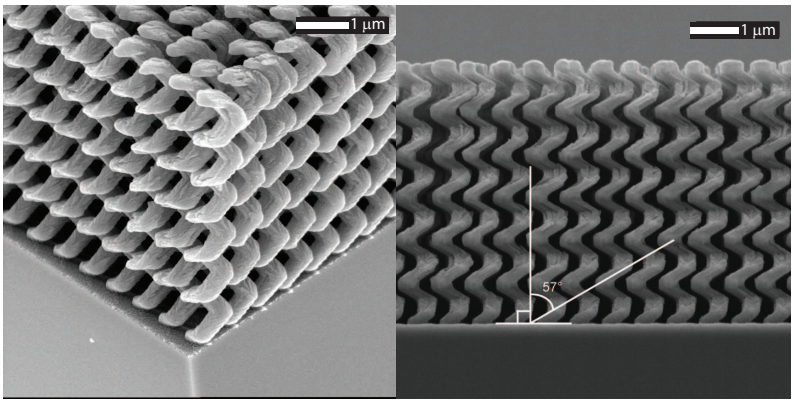

Figure 4.2. *SEM images of a square spiral film grown with an unassisted GLAD process. Reproduced with permission from Sorge et al. [107].*

riodic substrate motion and deposition provided by GLAD. The substrate topography created in the pre-patterning process enforces initial nucleation during film growth to occur on these elevated sites as opposed to random nucleation on a flat substrate. This additional processing step is solely responsible for enforcing the planar periodicity on the substrate, whereas the substrate motion on the GLAD process is responsible for the periodicity in the substrate normal direction.

Substrate pre-patterning was performed on double-polished silicon wafers by M. Summers. Fox-12 flowable oxide (Dow Corning) resist was spun at 2000 rpm to obtain a thickness of $175\ \mathrm{nm}$. The resist coated substrate was then exposed at $5\ \mathrm{kV}$ with a RAITH 150 EBL instrument (RAITH GmbH) to produce a periodic tetragonal array of seeds. In this pattern, the seed diameter was $500\ \mathrm{nm}$ and the center-to-center seed spacing is $750\ \mathrm{nm}$. An example of substrate patterning is shown in Fig. 4.3.

Films grown in this study were deposited by electron beam evaporation

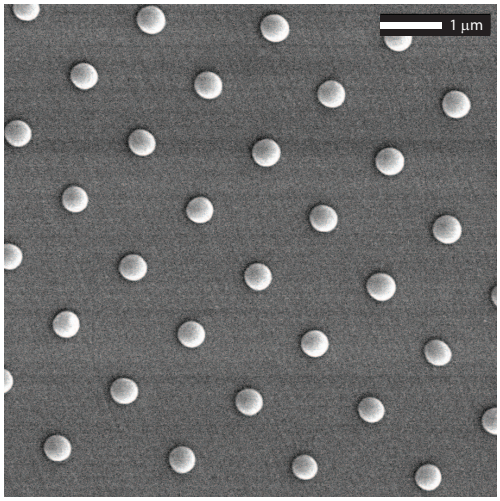

Figure 4.3. *SEM image of lithographically patterned substrate seed topography.*

from 99.99% silicon source material (Cerac Inc.) onto the periodically patterned silicon wafers described above. To begin the film deposition process a $50\ \mathrm{nm}$ vertical post seed enhancement layer was grown on the patterned substrates to enhance and improve substrate topography. Afterwards, square spiral films were grown with a $1000\ \mathrm{nm}$ spiral pitch unless otherwise noted. Each full spiral turn contained 4 slanted post sections, which were grown with the phisweep process. Phisweep parameters of 26.5° phisweep angle and $25\ \mathrm{nm}$ phisweep pitch were used to minimize the column broadening. To prevent column extinction and improve control over film growth at the square spiral corners, a $20\ \mathrm{nm}$ slow corner substrate motion algorithm was used [127]. Unassisted square spiral films were fabricated with a deposition pressure of $1.3 \times 10^{-5}\ \mathrm{Pa}$. Since the addition of argon was required to operate the argon source, the deposition pressure for the Ar-assisted films grown in this study was $4.0 \times 10^{-2}\ \mathrm{Pa}$.

Photonic simulations were performed by K. Tabunshchyk using the freely

available MIT Photonic Bands (MPB) package [128]. The MPB package obtains photonic band structures using the frequency-domain method by calculating the eigenmodes of an infinitely periodic dielectric structure, which are the electromagnetic waves that can propagate through the structure with a definite frequency.

4.3 Square Spiral Photonic Crystal Films

The film in Fig. 4.2 highlights the strengths and limitations of the traditional GLAD process. While a square spiral structure can be fabricated with high fidelity, at $\beta = 57^\circ$ the column tilt angle is substantially lower than the optimal value of 64° predicted by Toader and John [125]. When the simulated band diagram of this film is obtained, a full bandgap is not observed. This is shown in Fig. 4.4. Here, measurements of the column tilt angle and cross-section obtained from the SEM image in Fig. 4.4 were used in the simulation to produce an accurate model of the film structure. This simulation supports the fact that the column tilt angle in the square spiral films needs to match the theoretically predicted optimum values more closely than is possible with the unassisted deposition process.

Ar-assisted periodic square spiral films were fabricated with a $5\ \mathrm{mA}$ beam current to obtain a column tilt angle which more closely resembles the optimum theoretical value of 64°. Previous results from Fig. 3.3 show the potential of Ar-assisted deposition to fabricate slanted columns with β above 70°; more than sufficient range to achieve $\beta = 64^\circ$ in the diamond:1 case, but unfortunately insufficient to satisfy $\beta = 79^\circ$ in the diamond:5 case.

When the first Ar-assisted square spiral films were fabricated, significant

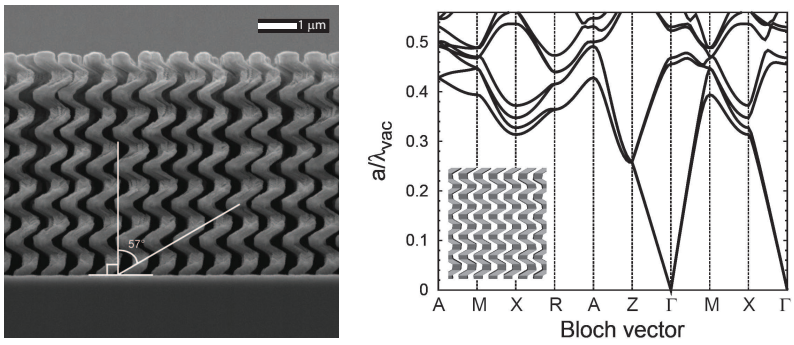

Figure 4.4. *Left: SEM image of an unassisted square spiral film. Right: Simulated photonic band diagram of the unassisted square spiral film with experimentally obtained column tilt and cross-section.*

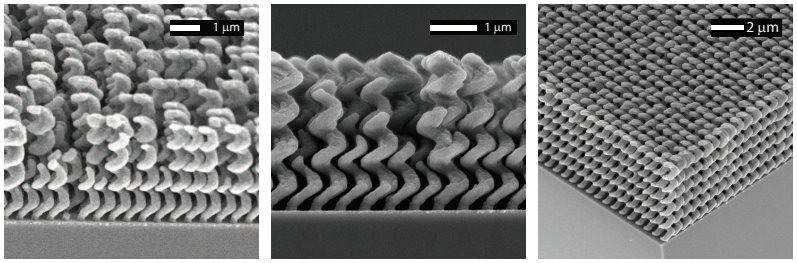

Figure 4.5. *Left, Middle: SEM images of Ar-assisted square spiral films with heavy column extinction. Right: Unassisted square spiral film without column extinction.*

column extinction was observed after one full column spiral was grown. This is shown in Fig. 4.5, with an unassisted square spiral film without column extinction for comparison. Here, a hypothesis was made that since the unassisted films do not suffer from significant column extinction, the high pressure and argon bombardment were responsible for the undesired growth behaviour seen in the Ar-assisted films. Higher pressures could broaden the incident flux angular distribution and affect the shadowing process.

To determine whether the detrimental film growth mechanisms were occurring in the slanted post segments or at the spiral corners, a half square spi-

ral film with $1\ \mu\mathrm{m}$ thick slanted post segments was fabricated and is shown in Fig. 4.6a. Note that at $1\ \mu\mathrm{m}$, these slanted post segments are much longer than the optimal column length. This was done to provide ample opportunity for column extinction to occur in the slanted post sections without the effects at the spiral corners interfering. In addition, to eliminate the possibility of column extinction occurring at the spiral corners, the argon source was turned off and the excess argon gas was pumped out of the system while the spiral corner was being fabricated. Argon was reintroduced and the argon source was turned on after the completion of the spiral corner and at the onset of growth of the subsequent slanted post segment. Fig. 4.6a indicates that this procedure was successful in heavily reducing the occurrences of column extinction and that a column tilt angle of approximately 65° is achieved with the argon conditions used.

Using this new procedure, a square spiral containing two full turns was fabricated. Side and oblique SEM images of this film presented in Fig. 4.6b and 4.6c respectively. These images show that this new strategy of briefly switching to unassisted deposition during the fabrication of the spiral corners is sufficiently effective at suppressing column extinction to enable the fabrication of thick square spiral films column tilt angles which are larger than observed in fully unassisted films. The column tilt angle in this new Ar-assisted square film was measured to be 61° during the first turn and 64° during the second turn. At 64°, this exactly matches the optimum theoretical value, but further study will need to examine how the column tilt angle scales with film thickness.

Photonic simulations were performed using the column cross-section ob-

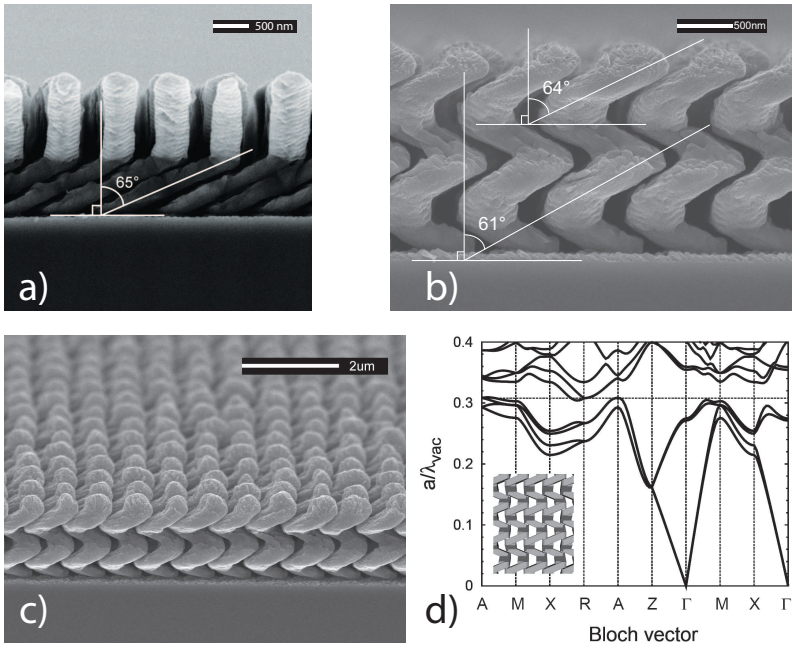

Figure 4.6. *a) Side view of a half-turn silicon square spiral film grown using an Ar-assisted GLAD process. b) Side and c) oblique views of a two-turn silicon square spiral film grown with an Ar-assisted GLAD process. d) Simulated photonic band diagram of Ar-assisted square spiral film with experimentally obtained cross-section, but optimized column tilt angle of* $68°$*.*

tained from Fig. 4.6b. This yielded a result which did not predict a full bandgap for a column tilt angle of $64°$. Using this cross-section, the optimal column tilt angle was found to be $68°$ which is shown in Fig. 4.6d, but this simulation still did not predict a full bandgap. However, this is closer to a full bandgap than what is predicted for unassisted films in Fig. 4.4.

Further simulations using a square column cross-section are shown in Fig. 4.7. Here, with an optimized square column cross-section, a structure with a column tilt angle of $57°$ representing the unassisted square spiral (Fig. 4.7a) is not predicted to have a full bandgap. This is due to the insufficient column tilt. Fig. 4.7b predicts a full bandgap with a square cross-section and a column

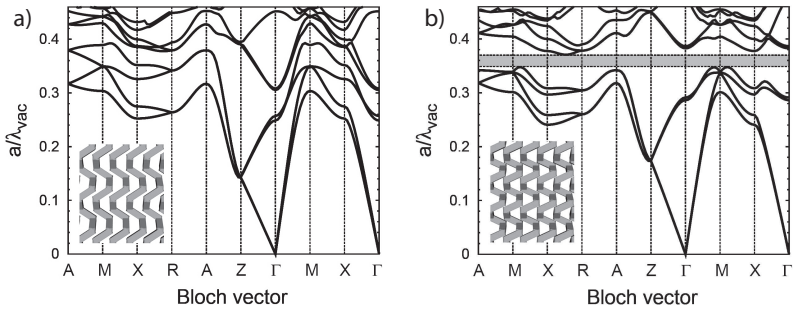

Figure 4.7. *Simulated band diagrams of square cross-section square spiral films with tilt angles of a)* 57° *and b)* 65°*. Reproduced with permission from Sorge et al. [107].*

tilt angle of 65°. These simulations suggest that obtaining a full three dimensional bandgap with the direct square spiral architecture using the GLAD process is only possible with modification to the column cross-section and with column tilt angles which are only obtainable with an Ar-assisted process. Future studies on GLAD square spiral photonic crystals should focus on improving the column cross-section. Refinement of the lithographically patterned substrates by modifying the seed shape should influence the shape of the column cross-section, as previous reports have shown the seed shape to have a large influence in silicon film structure [129].

Reflectance spectra were obtained with a Thermo Nicolet Nexus 670 Fourier transform infrared (FTIR) spectrometer for six turn unassisted and argon-assisted square spiral GLAD films (Fig. 4.8). These spectra are measured relative to an aluminum mirror reference (Thorlabs, PF10-03-F01). The photonic band structure presented in Fig. 4.6 predicts a near complete bandgap with an experimentally obtained column cross-section when the column spacing, a, is approximately a factor of 0.31 the size of the vacuum wavelength, λ_{vac}. Therefore, according to these simulations, the 750 nm column spacing used

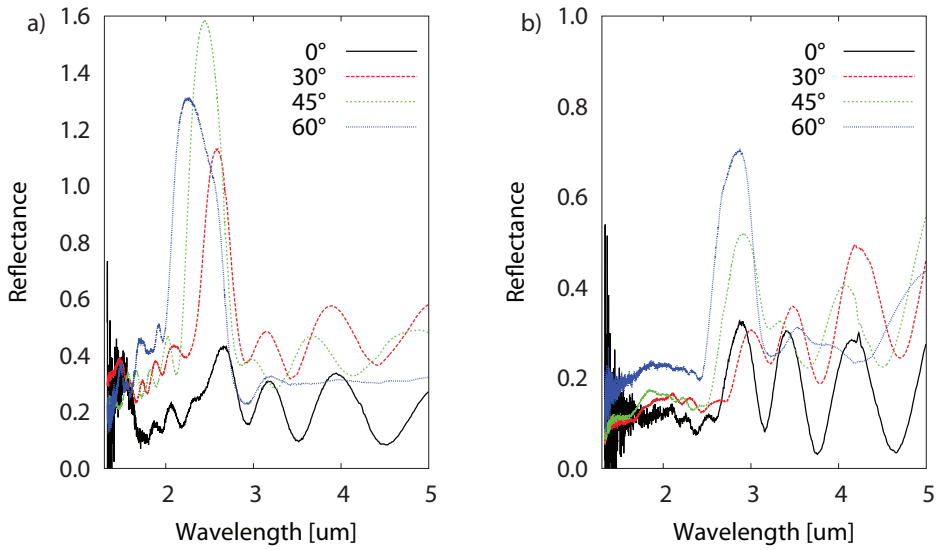

Figure 4.8. *Reflectance of six turn unassisted (left) and Ar-assisted (right) square spiral GLAD films relative to an aluminum mirror at various incidence angles.*

for these samples should produce a peak near $2.4\ \mu\text{m}$. In both samples, a reflectance peak is observed between $2\ \mu\text{m}$ and $3\ \mu\text{m}$, with larger peaks observed in the unassisted sample. The presence of these peaks suggest the existance of at least an indirect bandgap in both samples, but do not confirm a full bandgap in either sample. The reduced peak size in the argon-assisted spectra are most likely due to using substrate topographies and deposition angles which were optimized for unassisted square spiral deposition. The use of argon-assisted deposition is likely significantly increasing the film density to the point where the film fill fraction is larger than the optimal simulated value. The oscillations in the spectra are likely thin film optical interference.

The peaks near $3\ \mu\text{m}$ in the argon-assisted spectra are in better alignment than those observed in the unassisted spectra. This result motivates future argon-assisted square spiral work since better alignment of the re-

flectance peaks increases the likelihood of the presence of a complete photonic bandgap, which supports the findings of the photonic simulations. Future work should focus on optimizing the argon-assisted deposition parameters to improve the optical performance.

4.4 Conclusion

In this chapter, the effect of Ar-assistance on periodically structured porous thin films was investigated for potential application as three-dimensional thin film photonic crystals. Previously reported simulations of silicon square spiral photonic crystal structures predict optimal photonic properties for films with column tilt angles which exceed experimentally reported unassisted values. Since Ar-assisted deposition has been shown to increase column tilt angle in unpatterned films, studies of Ar-assisted deposition on patterned films to increase the column tilt were conducted with the goal of producing structures containing column tilt angles which closely match the optimal value predicated by simulation.

Unassisted square spiral films were grown first to demonstrate the current progress of square spiral photonic crystal fabrication and to provide experimental structures for photonic bandgap modeling. Here, full long-range three-dimensional periodicity was observed with negligible column deterioration throughout the entire thickness of the film. However, for these experimental structures, simulations confirm the absence of a full bandgap due to insufficient column tilt.

Ar-assisted square spiral films were then grown to attempt to increase the column tilt of the films. Initial attempts produced results where signif-

icant column extinction and loss of planar periodicity were observed. Further films were grown to identify where film structure deterioration was occurring, determining that the column extinction occurs during the growth of the spiral corners. To remedy this, Ar-assisted square spiral films were grown with unassisted spiral corners. This strategy eliminated the column extinction while maintaining the increased column tilt angle provided by Ar-assisted deposition.

Photonic bandgap simulations of these Ar-assisted films with experimentally measured column cross-sections were then performed. Simulations show an absence of a full bandgap in both unassisted and Ar-assisted films, even when optimum column tilt is considered. Further simulations using an optimized square column cross-section were then performed. These simulations predict a full bandgap in the Ar-assisted films, but not the unassisted film due to insufficient column tilt angle. Reflectance spectra of six turn unassisted and argon-assisted square spiral films show larger reflectance in the unassisted film, but superior peak overlap in the argon-assisted films. Since the fabrication of square spiral films with optimum column tilt angles has been demonstrated with Ar-assisted deposition, future study on Ar-assisted square spiral photonic crystal structures should focus on column cross-section improvement through the refinement of substrate patterning and optimization of the argon-assisted deposition parameters.

While a full bandgap was not experimentally demonstrated, significant progress has still been made in the development of square spiral photonic crystal fabrication. Simulations have shown that the increased column tilt provided by the Ar-assisted process is necessary to produce a full bandgap

and that unassisted square spiral films will only produce partial bandgaps. The experimental work here has addressed additional fabrication challenges present in the Ar-assisted deposition process and has demonstrated that the Ar-assisted process can be used to fabricate periodic square spiral structures with the theoretically optimum column tilt angles.

Chapter 5

Argon-Assisted Circular Polarization Filters

5.1 Introduction[1]

Optical activity was observed in obliquely deposited thin films by Young and Kowal who used physical vapour deposition (PVD) to fabricate obliquely deposited thin films ($< 70°$) on stepwise rotating substrates [5]. More recently, Motohiro and Taga used oblique angle deposition to create thin films with simple chevron microstructures. By abruptly rotating the substrate $180°$ halfway through each deposition [131], Motohiro and Taga were able to fabricate inorganic thin film waveplates with reduced positional homogeneity and film retardation anisotropy. In the years immediately after this milestone, theoretical studies on obliquely deposited films were performed by Azzam [132] as well as Lakhtakia and Weiglhofer [133]. Following these

[1]Portions of this chapter were done in collaboration with A. van Popta and have been published in [130]. My contributions in this chapter include all unassisted and argon-assisted experimental work and argon-assisted experimental design with shared contribution on the unassisted experimental design.

studies, Robbie *et al*. developed the glancing angle deposition (GLAD) technique [14, 134–136]. The high degree of control offered with this process generated large interest in utilizing it to engineer thin films for specific optical applications such as three-dimensional photonic crystals [6, 137, 138], gradient index optical filters [102, 103], broadband antireflection coatings [9], and linear polarizers [104].

Helical films are of interest due to their ability to differentiate states of circularly polarized light and are excellent candidates for circular polarization elements which are commonly found in auto-focus cameras. Porous helical films can be infiltrated with liquid crystals to enable switching behaviour [139] and have been proposed as a possible 3-D photonic crystal structure [140]. The circular Bragg behaviour exhibited in highly porous helical films can be harnessed to create humidity sensors, which have been experimentally demonstrated [141]. Even with numerous potential applications for obliquely deposited helical films, studies utilizing Ar-assistance have not been reported.

Research presented in the Ar-assisted film property modification chapter demonstrates the ability to significantly increase film density and the principal refractive indices. This makes Ar-assisted deposition potentially useful in improving the optical response of porous films deposited at high deposition angles. This chapter focuses on the use of Ar-assisted deposition to improve the performance of helical circular polarization filters. The performance and behaviour of unassisted helical films will be first examined to determine film growth regimes where Ar-assisted deposition could provide the most benefit. With a better understanding of the behaviour of unassisted films, studies on

Ar-assisted circular polarization filters will be presented.

5.2 Film Growth

The helical films grown for this study were fabricated by electron beam evaporation from 99.9% titanium dioxide source material (Cerac Inc.) to obtain a high refractive index and transparency in the optical wavelength regime, and were deposited onto glass substrates (Corning 7059). Fourteen unassisted helical films were grown, each at a unique deposition angle ranging from 30° to 87°. Selected scanning electron microscopy (SEM) images of these helical films are shown in Fig. 5.1. Helical films were fabricated with three right-handed helical turns and a helical pitch of 330 nm by applying three full clockwise substrate revolutions over the duration of the $1\ \mu\mathrm{m}$ deposition. To promote stoichiometry, the deposition pressure during the deposition of the unassisted helical films was kept constant at $7 \times 10^{-3}\ \mathrm{Pa}$ by adding $O_{2(g)}$ to the vacuum chamber. The normal incidence deposition rate ranged from $1.0\ \mathrm{nm\ s^{-1}}$ - $1.5\ \mathrm{nm\ s^{-1}}$ as measured by the CTM.

Ar-assisted helical titanium dioxide films were grown at 65° and 85° with a $5\ \mathrm{mA}$ beam current. Both samples were fabricated with three helical turns over a $1\ \mu\mathrm{m}$ film thickness. The deposition pressure was held constant at $1 \times 10^{-2}\ \mathrm{Pa}$ with the argon used to operate the argon source. During film growth, the deposition rate was measured to range from $1.0\ \mathrm{nm\ s^{-1}}$ - $1.1\ \mathrm{nm\ s^{-1}}$ by the CTM. To promote stoichiometry, post deposition oxidation was performed on the ar-assisted samples in an oven open to atmosphere. Samples were held in the oven for $24\ \mathrm{h}$ at $200\ ^\circ\mathrm{C}$.

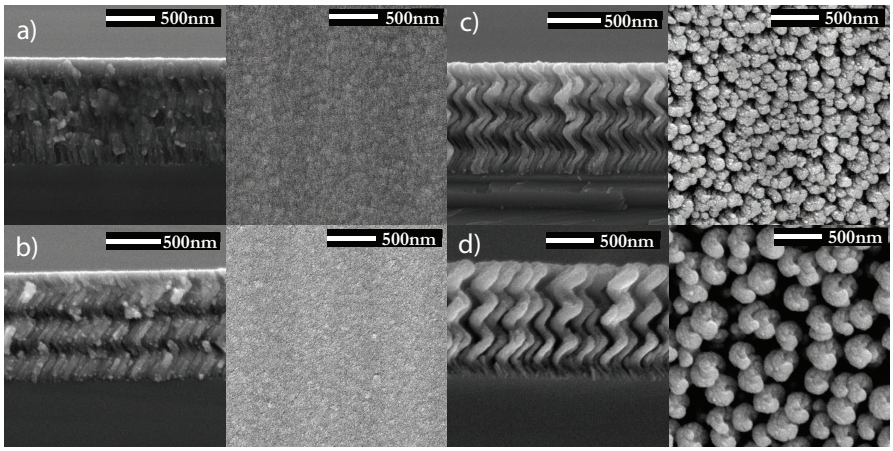

Figure 5.1. *SEM images of unassisted helical obliquely deposited films deposited at (a)* $30°$*, (b)* $65°$*, (c)* $80°$ *and (d)* $87°$ *illustrate the wide range of attainable film porosities. Side views are shown on the left, top-down views are shown on the right.*

5.3 Optical Characterization

Helically structured films exhibit circular Bragg effects and tend to reflect circularly polarized light of the same handedness while transmitting circularly polarized light of opposite handedness. The right-handed helical films fabricated for this study should preferentially transmit left circularly polarized (LCP) and reflect right circularly polarized light (RCP), whereas a left-handed film would behave in a reverse manner. The wavelength at which maximum circular Bragg reflectance occurs is proportional to both the average film index n and film pitch p ($\lambda \sim np$).

Optical measurements were taken in the visible to near infrared wavelength range. In general, films deposited at glancing angles are highly porous and will tend to diffusely scatter a significant amount of light. To determine the nature of the selective optical behaviour observed in unassisted helical films, both specular and diffuse optical measurements were made to char-

acterize the relationship between film porosity and the selective response to circular polarized light.

Variable angle spectroscopic ellipsometry (VASE) was used to measure selective specular transmittance, the difference between specularly transmitted left, $T(\text{LCP})_S$, and right, $T(\text{RCP})_S$, circularly polarized light. The Stokes vectors of left and right circularly polarized light are shown in Eqs. 5.1 and 5.2 respectively. The specular response was measured by performing a spectroscopic scan to obtain the m_{14} (1st row 4th column) Mueller matrix coefficient. Having obtained the transmittance Mueller matrix, the selective specular transmittance of circularly polarized light is calculated with Eq. 5.3. The VASE method was used to measure the selective response in both the unassisted and Ar-assisted samples.

$$\vec{S}_{LCP} = \begin{pmatrix} 1 \\ 0 \\ 0 \\ -1 \end{pmatrix}. \tag{5.1}$$

$$\vec{S}_{RCP} = \begin{pmatrix} 1 \\ 0 \\ 0 \\ 1 \end{pmatrix}. \tag{5.2}$$

$$T(\text{LCP})_S - T(\text{RCP})_S = -2m_{14}(\lambda). \tag{5.3}$$

Specular transmittance measurements in unassisted films were repeated using a Perkin Elmer Lambda 900 UV/VIS/NIR spectrophotometer. LCP and

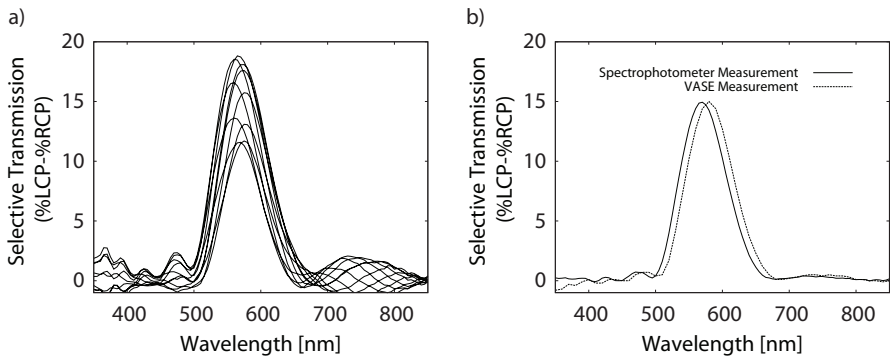

Figure 5.2. *(a) Selective specular transmission scans obtained with spectrophotometry for different azimuthal orientations of an unassisted helical film fabricated at* $65°$*. (b) Comparison of the average of the spectrophotometer measurements and the VASE measurement of selective specular transmittance for an unassisted helical film grown at* $65°$*.*

RCP light were generated by passing unpolarized light through a linear polarizer followed by an Oriel achromatic quarter wave plate with its fast axis oriented $\pm 45°$ relative to the transmission axis of the linear polarizer. The resulting circularly polarized light then propagated through the sample and into a detector, positioned far behind the sample to collect only the specularly transmitted light. The data obtained with the spectrophotometer was found to be highly dependent on the orientation of the substrate where different spectra would be obtained when the substrate was rotated about an axis that is normal to the substrate plane. This is shown in Fig. 5.2a. To alleviate this issue, multiple data sets were obtained in the spectrophotometer with different in-plane substrate rotations and averaged. The resulting average of the selective response from the individual runs was found to be in close agreement with the data obtained through ellipsometry. The two measurements are compared in Fig. 5.2b.

The helical films in this study that were deposited at glancing deposition

angles ($\alpha > 80°$) appeared hazy to the naked eye, suggesting significant diffuse scattering. To measure the contributions of diffusely scattered light to the circular Bragg response, the spectrophotometer setup described above was refitted with a broadband integrating sphere with a barium sulfate coating to capture the diffusely scattered light as it left the sample. A photomultiplier tube was placed on one of the ports of the integrating sphere to measure the response.

To measure diffuse transmittance, the sample was mounted on the integrating sphere's front port. With the exit port covered with a scattering surface of barium sulfate, this arrangement captures both the specular (T(LCP$_S$, T(RCP)$_S$) and diffusely (T(LCP)$_D$, T(RCP)$_D$) transmitted light. To separate the two contributions, the previously obtained specular transmittance results were subtracted:

$$T(\text{LCP})_D - T(\text{RCP})_D = T(\text{LCP}) - T(\text{RCP}) - [T(\text{LCP})_S - T(\text{RCP})_S]. \quad (5.4)$$

Diffuse reflectance was measured by mounting the sample against the exit port of the integrating sphere. In this arrangement, light that undergoes specular reflection escapes through the front port and only the diffusely reflected contribution is collected. A small portion of the scattered light that escapes through the front port of the integrating sphere and light that is scattered laterally in the plane of the substrate was unaccounted for. To reduce the effect of thin film interference on the diffuse response, the same methodology of averaging multiple measurements at different substrate orientations was used. However, diffuse data was unable to be obtained with the VASE method be-

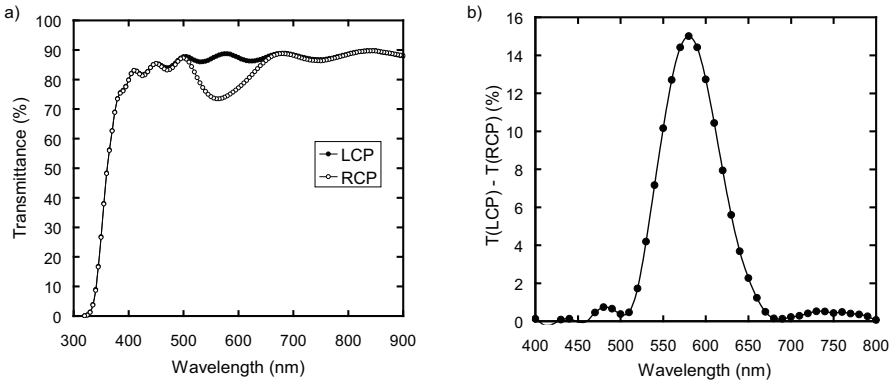

Figure 5.3. *Transmittance (a) and selective transmittance (b) spectra of an unassisted helical film deposited at $\alpha = 65°$. Reproduced with permission from Sorge et al. [130].*

cause the VASE apparatus is equipped to solely collect specular signals.

5.4 Selective Optical Behaviour

A characteristic specular transmittance spectrum taken with the spectrophotometer is shown in Fig. 5.3a. The selective transmittance is obtained by subtracting the LCP and RCP transmittance spectra from each other, and is shown in Fig. 5.3b. The two features of the response that are of interest are the magnitude and the wavelength at which the peak circular Bragg response occurs.

The magnitude of the response can be controlled by the number of turns in the film, ie: more turns increases the circular response. However, this effect begins to saturate as the film thicknesses continues to be increased. At highly oblique deposition angles, column competition during film growth results in column extinction, leading to broadening in the remaining columns so that constant film porosity can be maintained, which tends to cause TiO_2

helical films with more turns to lose structural definition at larger thicknesses [102]. This effect commonly is observed in sufficiently thick films deposited at highly oblique angles for a large number of film materials and structures. In particular, this had been a major hurdle in the fabrication of square spiral photonic crystals before the development of the phisweep process which can heavily suppress column broadening in straight slanted post film segments. Before the phisweep process alleviated these issues, the appreciable column broadening would result in substantial losses in structural fidelity and would severely limit the photonic properties of the films. In addition to the deterioration of structural definition in thick films, scattering is more prominent in thick films, so the usefulness of adding turns to helical films to increase their response is limited at large deposition angles. As a result, three helical turns were used for each sample to obtain appreciable circular Bragg effects while avoiding excessive scattering losses.

The dependence of the Bragg wavelength on the film deposition angle is shown in Fig. 5.4. The measurement error in the peak wavelength is $10\ \mathrm{nm}$. The peak wavelength blue-shifts with increasing deposition angle, which is due to the increasing porosity in the films, resulting in a reduced average refractive index in the film. The dependence of film porosity on the deposition angle, as well as porosity measurements of obliquely deposited films have been reported elsewhere [8, 26, 142].

The dependence of selective specular transmittance of circularly polarized light on the film deposition angle, obtained through spectroscopic ellipsometry, for unassisted films is shown in Fig. 5.5. Due to the unreliability of fabricating films at deposition angles $> 87^\circ$, the maximum film deposition

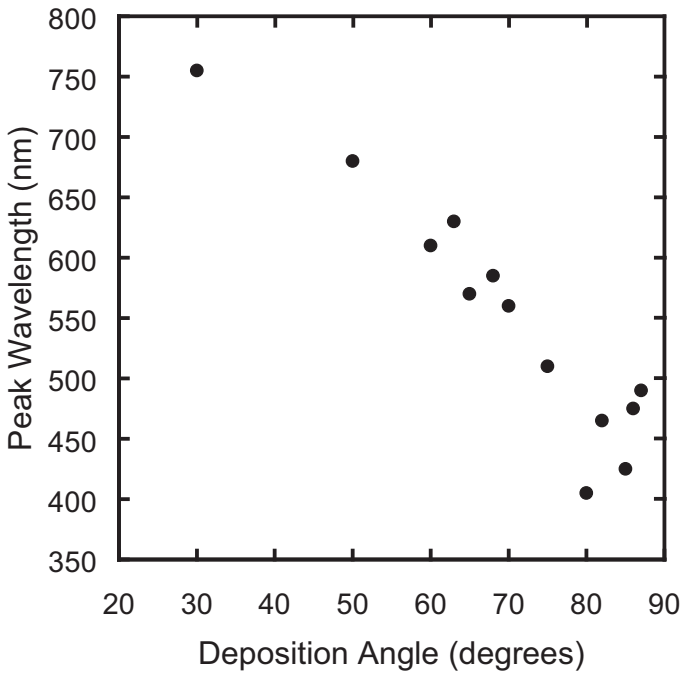

Figure 5.4. *Peak selective transmittance wavelength vs. deposition angle α in unassisted helical TiO_2 films. Reproduced with permission from Sorge et al. [130].*

angle that was studied was $87°$. Films deposited above $87°$ were attempted, but uncertainties in the deposition angle due to limitations in the deposition system prevented reliable film fabrication with sufficient precision at these high deposition angles. This causes the data to appear to have a maximum at $87°$, but it is uncertain as to whether the selective behaviour in unassisted films will continue to increase in films grown at higher deposition angles or the increasing porosity will dominate all other effects and reduce the selective response.

In the following discussion, it is useful to interpret a helical film as a material in which the orientation of a local linear birefringence rotates through the thickness of the film to produce a circular Bragg grating. The data in

Fig. 5.5 shows two regimes where the response is maximized. The first local maximum in the selective circular Bragg response occurs at a deposition angle of $65°$. In this regime, the deposition angle is not large enough to promote significant substrate shadowing and the resulting films are comprised of closely packed helical columns. The anisotropic nature of the film growth, which arises from column broadening, produces substantial form birefringence which is similar to that observed in the slanted post films studied in the property modification chapter. This effect is amplified as the deposition angle is increased. However, birefringence also scales with the refractive index of the film, which was found to decrease as the deposition angle is increased. Furthermore, the column tilt angle, measured from the substrate normal, increases from approximately $25°$ to $45°$ as the deposition angle increases from $50°$ to $87°$, which also lowers the in-plane form birefringence. These competing effects result in a maximum form birefringence in unassisted films that occurs at deposition angles ranging between $55°$ and $65°$ for most materials [143–145]. The maximum form birefringence produces a maximum circular birefringence, which is responsible for the stronger Bragg reflectance observed in the helical TiO_2 films deposited near $65°$.

The second local maximum in the selective response to circularly polarized light occurs at glancing deposition angles where substrate shadowing is significant and the films are highly porous (Fig. 5.1d). In this regime, the films are comprised of individual isolated helical structures as opposed to tightly packed columns. The isolated helices provide a large number of air/-film interfaces for light to scatter off of. The milky appearance of the helical films above $80°$ also suggests that significant scattering is occurring. Due to the chiral film structure, if the scattering that occurs is anisotropic, it can be

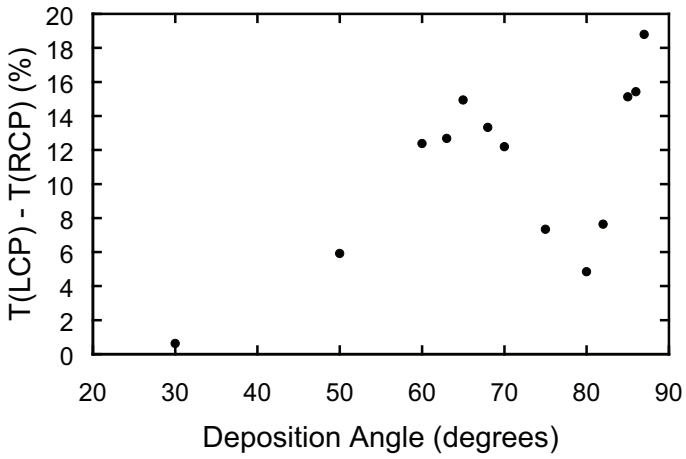

Figure 5.5. *Maximum selective specular transmittance of circularly polarized light in unassisted helical TiO_2 thin films. Reproduced with permission from Sorge et al. [130].*

expected that this scattering will contribute to the selective circular Bragg response.

Diffuse transmittance and reflectance data are shown in Fig. 5.6(a) and 5.6(b) respectively. As the deposition angle is increased beyond 80°, amplified substrate shadowing causes column separation, as observed in Fig. 5.1. This produces films with high porosity which exhibit increased anisotropic scattering. This suggests that the onset of scattering occurs when the helical structures transition from being densely packed to being isolated from one another. The contribution of anisotropic diffuse scattering was subtracted from the response shown in Fig. 5.5 and re-plotted in Fig. 5.7. As expected, the first local maximum, where the film is comprised of tightly packed columns, remains relatively unchanged, indicating a minimal contribution from scattering in this regime. However, the second maximum, where the film is comprised of isolated columns, the selective response is reduced sub-

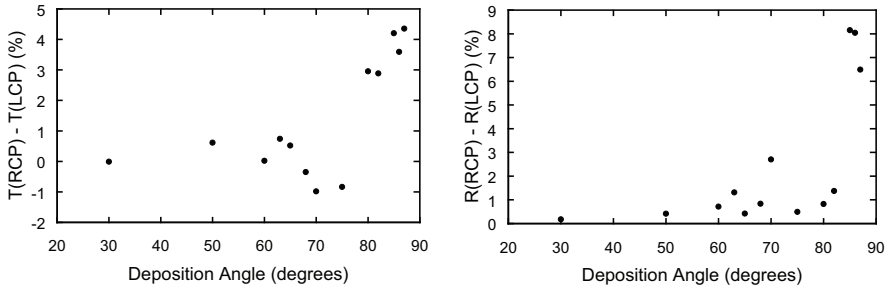

Figure 5.6. *(a) Maximum selective diffuse transmittance of circularly polarized light in helical TiO_2 thin films; (b) Maximum selective diffuse reflectance of circularly polarized light in helical TiO_2 thin films.*

stantially when the diffusely scattered components are removed, suggesting the anisotropic scattering, not form birefringence, is the dominant mechanism contributing to the selective response in these films.

The selective optical response can be summarized in the following manner: At deposition angles less than α = 65°, the selective response is dominated by the increase in column broadening due to increasing anisotropic shadowing in the film. As the deposition angle increases further such that $65^\circ \leq \alpha \leq 80^\circ$, the selective response decreases due to the decreasing average refractive index in the film. For $\alpha \geq 80^\circ$, scattering becomes the dominant mechanism and another peak in the selective response is observed at $\alpha = 87^\circ$.

With the selective optical response in unassisted obliquely deposited helical thin films understood, the potential benefits of implementing an Ar-assisted process can be evaluated. In the lower optimal regime, improvements in the selective optical behaviour are less likely to be realized. The dense nature of these films, when grown with the traditional GLAD process, result in a shortage of available void space for further densification from implementing an Ar-assisted process. This limits any potential benefit from an

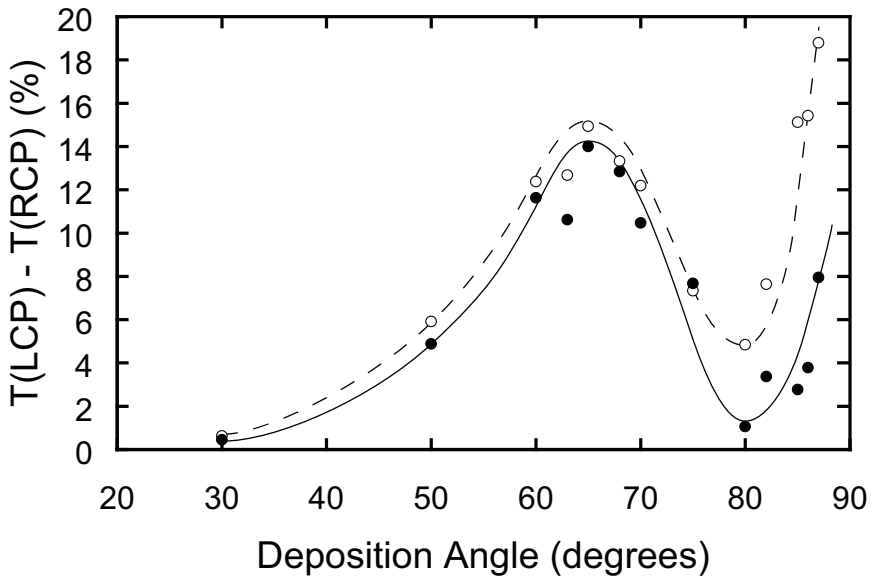

Figure 5.7. *Maximum selective specular transmittance of circularly polarized light in helical TiO_2 films (○ diffuse components included, ● diffuse components removed).*

increase in the average overall refractive index. However, since the selective response is largest in the highly porous regime and the Ar-assisted process has a large influence in this regime, Ar-assisted deposition may be able to produce significant improvements in the selective optical response here. Ar-assisted helical films fabricated in this regime would have larger β, higher density than unassisted films grown at the same deposition angle, and would result in films that have a higher average refractive index and are more robust. While the higher film density may decrease the scattering component of the selective response, the higher film index combined with a larger tilt angle may yield favourable behaviour.

5.5 Ar-Assisted Helical Films

To test whether incorporating Ar-assistance in helical film fabrication will improve the selective circular optical response observed in unassisted helical films, Ar-assisted helical films were grown at deposition angles corresponding to regions of significant selective circular optical behaviour in unassisted helical films. Here, Ar-assisted helical TiO_2 films were grown at $65°$ and $85°$ with a $390\ \mathrm{V}$ argon energy and $5\ \mathrm{mA}$ beam current.

The selective response to circularly polarized light in the Ar-assisted helical films was measured with VASE, and was compared to the response observed in the unassisted films as shown in Fig. 5.8. The data in Fig. 5.8 shows a significant increase in the selective circular behaviour in the Ar-assisted film grown at $85°$ and a substantial decrease in the Ar-assisted film grown at $65°$. Before discussing these results in more detail, it is helpful to review the different factors which can contribute to the selective behaviour and how these relate to film property modification with the Ar-assisted process.

- Form birefringence

  In helical films, the presence of a form birefringence which rotates throughout the film thickness is the main component that gives rise to the selective circular behaviour at low deposition angles where the helical columns are closely packed together. The form birefringence in obliquely deposited films is largely dependent on the in-plane column cross-section. As the deposition angle increases, both column broadening and column tilt increase. These two factors each have their own impact on the column cross-section. As column broadening increases, the in-plane col-

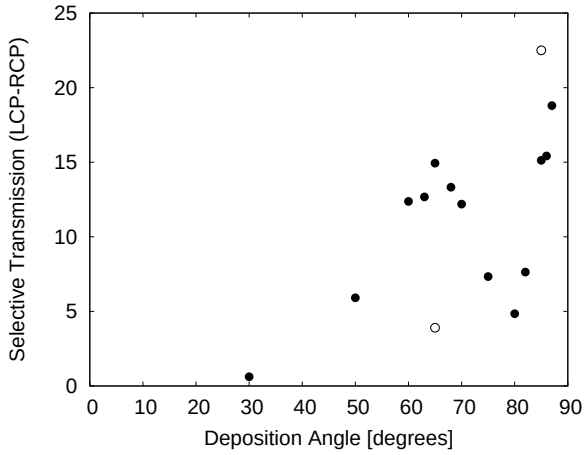

Figure 5.8. *Selective specular transmission of unassisted (●) and* $5\ \mathrm{mA}$ *Ar-assisted (○) helical* TiO_2 *films*

umn width increases in the direction normal to the deposition plane. When the column tilt angle increases, the in-plane column width also increases, but in the direction which is orthogonal to the column broadening direction. In unassisted helical films, at low deposition angles the column broadening dominates this relationship and significant form birefringences can be produced. At higher angles, the increasing column tilt may become a larger factor in determining the form birefringence.

In Ar-assisted films, the column tilt angle is larger than in unassisted films. This will have the effect of reducing the dominance of column broadening in generating the form birefringence. However, under appropriate conditions, Ar-assistance can be used to potentially increase the column tilt angle to the point where the column width in the broadening direction is the smaller of the two characteristic in-plane column

widths. At this point, further increases in column tilt will result in increases in form birefringence with a sign opposite to what is observed at lower column tilt angles.

- Refractive index

  Once a suitable column cross-section to create form birefringence is established, the average refractive index in the film needs to be considered. While the presence of form birefringence is necessary to generate selective circular behaviour in helical films, this selective behaviour scales with the average refractive index. Improving the selective circular response by increasing the average refractive index in the film can be achieved by either increasing the bulk refractive index of the film material or increasing the film density. Although using an Ar-assisted process to increase packing density of the bulk material to improve the refractive index may have a small benefit, increasing the bulk refractive index of the material is predominantly based on material selection. In chapter 3, the Ar-assisted process was shown to significantly increase the film density and refractive indices in slanted post films for a wide range of materials. This increase in film density can be of benefit in helical films to increase the average refractive index and therefore improve the selective circular optical response.

- Film porosity

  As discussed earlier, at high deposition angles films become comprised of isolated structures as opposed to tightly packed columns. In unassisted films deposited at these high angles, the isolated structures produce significant scattering. In helical films these structures anisotropi-

cally scatter circularly polarized light, which was shown earlier in this chapter to dominate the selective circular optical response at high deposition angles. By increasing film density with an Ar-assisted process, the helical structures would become more tightly packed which may reduce this anisotropic scattering and lower its contribution to the selective circular response.

At 65° the selective circular response decreases from 14.9 % selective specular transmission to 3.9 % selective specular transmission. The reasons for this decrease are twofold. First, since the unassisted helical film grown at 65° is already fairly dense and composed of tightly packed helical structures, there is less void space for film densification to occur with Ar-assisted deposition. This will minimize the potential to increase the average refractive index and thus minimize any increase in selective response.

The other reason why the selective response decreases in the Ar-assisted film deposited at 65° is related to the column tilt. At a deposition angle of 65° the column tilt angle in the unassisted helical film is approximately 32°, whereas in the 5 mA Ar-assisted helical film the tilt angle is approximately 38°. With these tilt angles, it is unlikely that the column tilt angle increase is sufficient to be in the structural regime where the form birefringence is dominated by the planar refractive index related to the column tilt. However, it is difficult to fully confirm this without a measurement of the columnar cross-section. Unfortunately, it is extremely difficult to analyze single helical structures in SEM images of films where the structures are not completely isolated. It is also difficult to extract out of plane columnar cross-sections with SEM images of the column tips because the curved helical structures

add significant complication in isolating the edge for cross-sectional analysis. Although SEM images can be used to measure the out of plane columnar cross-section in slanted post films, as demonstrated in in Appendix C, it is not clear how this would compare to helical columnar cross-sections. As a result, it is suspected that the increased column tilt angle in the Ar-assisted helical film grown at 65° causes a reduction in the selective response, but this was not confirmed experimentally.

At 85° the selective circular response increases from 15.1 % selective specular transmission to 22.5 % selective specular transmission. There are two main differences between the $\alpha = 65^\circ$ and the 85° cases that account for the changes in the selective response. These are the column tilt angle and film density which behave very differently in the two cases. Based on the SiO_2 slanted post results in Table 3.4 the film density of the 85° films is expected to increase by a larger amount with Ar-assistance than the 65° films would. This should increase the average refractive index in the film, much like the slanted post films in Table 3.6, and as a result, increase the selective circular response. This increase in film density is also expected to reduce scattering, which is desirable for most applications. The silicon dioxide slanted post films presented in Table 3.4 show an increase in normalized film density for an ar-assisted film grown at 85° (0.51) to nearly that of an unassisted film grown at 70° (0.56). If an equivalent increase in film density occurs in helical films, the Ar-assisted helical film grown at 85° should have nearly the equivalent density to an unassisted film grown at 70°. Fig. 5.6 shows that at 70°, there is minimal scattering for an unassisted helical film. Therefore, under the assumption that the argon-induced increase in density is similar for slanted post and helical films, there should be minimal scattering in the Ar-assisted

helical film grown at $85°$.

In addition to increased film density, while the trend in Fig. 3.5 predicts a smaller increase in tilt angle for the $85°$ case, it does predict an overall larger tilt angle that is significantly larger than in the $65°$ case. SEM images comparing the structure of an Ar-assisted helical film grown at $85°$ with an unassisted film grown at $87°$ is shown in Fig. 5.9. Here the difference in tilt angle is very noticeable. An unassisted helical film grown at $85°$ will have a tilt angle close to that of the unassisted $87°$ helical film in Fig. 5.9 which was measured to be approximately $45°$. The column tilt angle of the Ar-assisted helical film grown at $85°$ was measured to be approximately $57.5°$. This is much higher than in the unassisted case and may be high enough such that the large column tilt is dominant over column broadening effects. If this is the case, the increasing column tilt should result in an increase in form birefringence. However, as stated earlier, this is difficult to confirm without an accurate measurement of the column cross-section.

Another interesting observation was made when studying the column tilt angle in the Ar-assisted helical film grown at $85°$. Since the trend in Fig. 3.5 is for slanted posts fabricated at $85°$, a prediction of the column tilt of a helical film grown under otherwise similar conditions can be made. The column tilt angle modification trend in Fig. 3.5 predicts an Ar-assisted column tilt angle of $58.5°$ where the actual tilt angle measured was approximately $57.5°$. Even though the structures between the two cases aren't identical, the slanted post trend in Fig. 3.5 closely predicted the tilt angle observed in the Ar-assisted helical film.

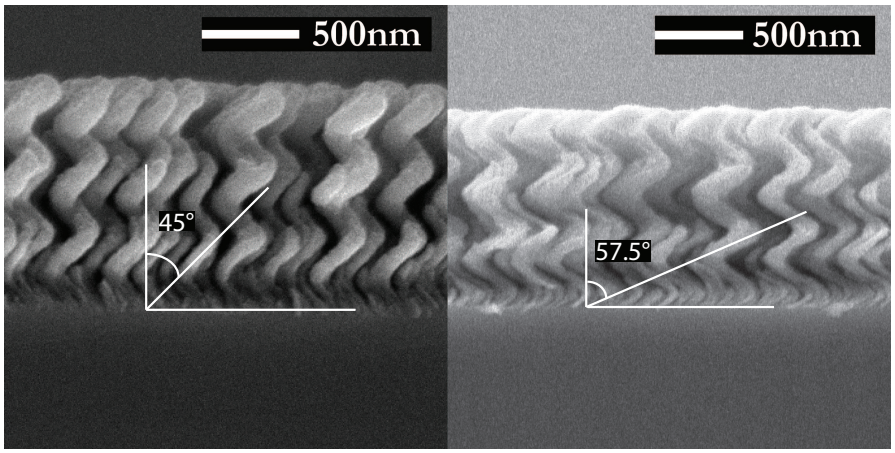

Figure 5.9. *SEM images of helical obliquely deposited films deposited at* $87°$ *(Unassisted, Left) and at* $85°$ *(Ar-assisted,* 5 mA*, Right).*

5.6 Conclusion

In this chapter, the ability of Ar-assisted deposition to modify the film density and column tilt angle was used to improve the selective optical response to circularly polarized light. First, a study on unassisted helical films was performed to determine film growth regimes where Ar-assisted deposition would have the most benefit.

In the unassisted helical film study, two optimal film growth regimes were found for generating a significant selective optical response to circularly polarized light. SEM analysis reveals a transition between structural morphologies at a deposition angle of approximately $80°$. Below this angle, films are comprised of closely packed helical columns and the selective response is dominated by an optimized form birefringence. In this region, a maximum in the selective response of 14.9 % was found at a deposition angle of $65°$. At deposition angles larger than $80°$, substrate shadowing becomes signifi-

cant enough to cause the helical structures to separate into isolated structures. Once this occurs, the proliferation of air/film interfaces results in significant anisotropic scattering which dominates the selective circular behaviour. In this region, a maximum in the selective response of 15.1 % was found at a deposition angle of $87°$.

Deposition angles of $65°$ and $85°$ were chosen to study the effects of Ar-assisted deposition on the selective behaviour in these two optimal unassisted film growth regimes. At $65°$, the selective response was observed to decrease from 14.9 % to 3.9 %. This decrease in selective behaviour may be due to reduced in-plane cross-sectional anisotropy, which results in a reduced form birefringence. However, this is difficult to confirm without a measurement of the columnar cross-section. A direct measurement of the in-plane column cross-section was unable to be made due to the significant complications involved with isolating a single helical column with SEM analysis of dense films.

At $85°$, the selective response increases from 15.1 % to 22.5 %, which is the largest selective behaviour of all of the films grown in the study. Here, both the column tilt angle and the film density significantly increase. The film density increase results in a higher average refractive index which boosts the selective response. In addition, the column tilt angle increases from approximately $45°$ to $57.5°$ which may increase the column anisotropy, enhancing the selective behaviour. Again, this is difficult to confirm without a measurement of the column cross-section.

The trend in column tilt angle modification of slanted post films with Ar-assistance from Chapter 3 was used to predict the column tilt angle of the Ar-

assisted helical film grown at $85°$. This trend predicts a column tilt angle of $58.5°$ in the Ar-assisted film. This is very close to the measured value of $57.5°$ and is especially interesting since two different film structures are involved.

These initial results on Ar-assisted helical films look promising and lay the groundwork for further development towards the fabrication of circular polarization filters with improved effectiveness. Future studies on Ar-assisted circular polarization filters should focus on optimizing the argon conditions and deposition angle to maximize the selective behaviour. These results also motivate a more thorough characterization of Ar-assisted helical film properties. Focus should be placed on comparisons on Ar-assisted property modification for different film structures. This will provide a better understanding of how the property modification in helical films effects the selective behaviour and also could provide additional insight into the growth of unassisted helical films.

Chapter 6

Humidity Sensing Using Argon-Assisted Films

6.1 Introduction[1]

A study was performed to explore the effects of argon bombardment on the response of thin film humidity sensors grown with the Ar-assisted GLAD deposition process. Here it will be shown that the capacitive response to humidity in devices grown with Ar-assisted deposition is distinct from humidity sensing devices grown with an unassisted process.

Humidity sensing studies with unassisted GLAD films have been reported for more than a decade. The first such studies by Wu *et al.* investigated the sensing behaviour of silicon monoxide films [147, 148]. The effects of deposition angle and column shape were reported, and ageing and hysteresis were discussed as well. Further studies by Harris *et al.* investigated perforated

[1] Portions of this chapter were performed in collaboration with M. Taschuk and have been published in [146]. My contributions in this chapter include all film fabrication with shared contribution on the experimental design.

photoresist films fabricated using GLAD template and the response time of both the direct GLAD and perforated structures [149,150]. Humidity sensing studies on planar interdigitated electrodes were then reported by Steele *et al.* [7,26,151,152]. These studies focused on optimizing the response with deposition angle, film density, electrode geometry, film material and thickness, and led to improvements in response time, response magnitude and sensitivity. Following the studies by Steele *et al.*, experiments on photocatalytic regeneration of titanium dioxide humidity sensors to reverse the effects of ageing and improve the overall response to changes in humidity were reported [153,154]. The effects of post-deposition reactive ion etch treatments on the response to humidity have also been reported [155]. While most studies have been on capacitive devices, optical humidity sensing devices such as gradient index [156], narrow band-pass [157] and chiral [158] filters have been fabricated with unassisted GLAD processes.

6.2 Sensor Characterization

Following the work of Steele [7,152,159], the sensors used in this study are based on a device geometry of an interdigitated gold electrode coated with a GLAD film. Changes in capacitance are produced when water adsorbs onto the surface of the porous film, and this behaviour can be modified by altering the pore size distribution, film density and geometry. Countersunk interdigitated electrodes were fabricated using a proprietary procedure by Micralyne Inc., in order to achieve a planar surface for subsequent GLAD film deposition. The total planar area covered by the two electrodes was $100\ \mathrm{mm}^2$ with an electrode digit width of $3\ \mu\mathrm{m}$, digit length of $10\ \mu\mathrm{m}$ and digit spacing of $5\ \mu\mathrm{m}$. The electrodes are shown in Fig. 6.1.

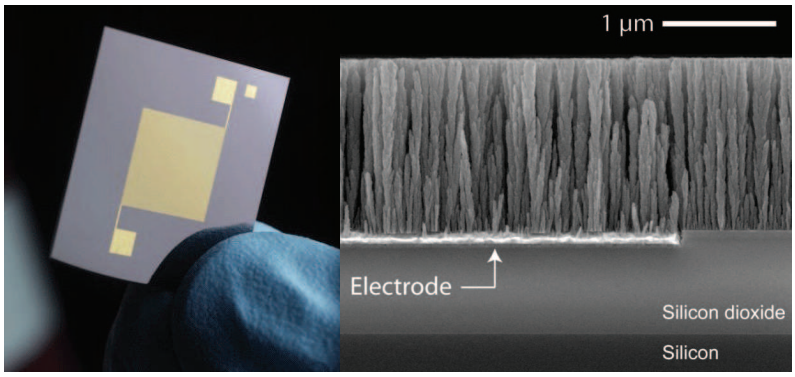

Figure 6.1. *Left: substrate used for GLAD-based humidity sensing. Right: IDE substrate coated with a vertical post GLAD film. Reproduced with permission from [7] ©2008 IEEE.*

The response to relative humidity (RH) was investigated using a custom-built humidity-sensing chamber developed in the laboratory by previous researchers [7]. The relative humidity in the chamber was continuously monitored with a commercial RH probe (Vaisala HMP100) calibrated using saturated salt solutions of lithium chloride, magnesium chloride, sodium chloride, and potassium sulfate (Fischer Scientific, laboratory grade salts) [160]. Full details on the calibration process can be found in [159]. These four salts were used to saturate a small amount of liquid water ($10 - 20$ mL). The saturated solution was then placed in a sealed chamber which was allowed to equilibrate with the surrounding environment (22 h). At a given temperature, each of the four salt solutions reach equilibrium at a different relative humidity [160]. These four salt solutions were then used to test the probe relative to the known RH of each solution. Using this method, an absolute error of less than 2% with a 95% confidence level was established across the entire humidity range.

The series capacitance C_S was measured using a LCR meter (QuadTech

1715 Digibridge) at $1\ \mathrm{kHz}$ and $1\ \mathrm{V_{rms}}$. The LCR meter was calibrated by measuring 86 resistors spanning across 8 orders of magnitude and 125 capacitors spanning across 7 orders of magnitude from multiple manufacturers. Using this method, an absolute error of 0.8% with a 95% confidence level was obtained for resistance measurements and an absolute error of 2.4% with a 95% confidence level was obtained for capacitance measurements. The sensor response was investigated by cycling the humidity between 1% RH to 90% RH in 5% RH steps. All RH data presented here is taken from the increasing half of the second full cycle.

In these experiments, the measurement of C_S includes the capacitance of the probe wires (No. 32 AWG solid) which were attached to the substrate. The capacitance due to the wires can was modelled as a pair of parallel wires. An expression for the capacitance of two parallel wires with length, l, radius, a, and separation, d, is given in Eq. 6.1. Using a wire length of 20 cm, wire radius of 0.1 mm, and a separation of 1 cm, the resulting capacitance calculated using Eq. 6.1 is 0.4 pF. When this is compared to the measured capacitance of 2 nF for a bare IDE substrate, it is concluded that the wire capacitance has a negligible contribution on the overall measured series capacitance.

$$C = \frac{\pi \epsilon l}{ln\left(\frac{d}{2a} + \sqrt{\frac{d^2}{4a^4} - 1}\right)}. \tag{6.1}$$

6.3 Film Growth

Vertical post films were grown by electron beam evaporation from 99.9% titanium dioxide source material (Cerac Inc.). Unassisted films were grown

at different deposition angles ranging from $60°$ to $85°$ to produce varying amounts of film porosity. To improve stoichiometry in the unassisted films, oxygen was added during deposition such that the deposition pressure was kept constant at 7×10^{-3} Pa. The unassisted films were grown to a 1.5 μm nominal thickness with a normal incidence deposition rate ranging from 1.0 nm s^{-1} to 1.5 nm s^{-1} as measured by QCM.

Two additional vertical post titanium dioxide films was grown with Ar-assisted deposition at a deposition angle of $81°$, with an argon incidence angle of $36°$. These films were grown to a nominal 1.5 μm thickness at a rate of approximately 0.7 nm/s. To obtain different film morphologies, a different argon current was used for each film, 0 mA and 7 mA. Argon was added during deposition, such that a pressure of approximately 1.3×10^{-2} Pa was maintained to operate the argon source. Since oxygen could not be added during deposition, improvements in film stoichiometry were achieved with 24 hour oxidations in an oven operating at 100 °C that was open to atmosphere. It should be noted that the 0 mA Ar-assisted film corresponds to a film which was fabricated in an argon atmosphere and underwent a similar post-deposition oxidation treatment to the other Ar-assisted film, but did not undergo any argon bombardment.

6.4 Ar-Assisted Humidity Measurement

SEM images of the Ar-assisted films grown at $81°$ are shown in Fig. 6.2. The deposition conditions, thicknesses and C_S at 30% RH and 70% RH are given in Table 6.1. The capacitive response of the Ar-assisted sensors is given in Fig. 6.3, and the response of the unassisted films is given in Fig. 6.4.

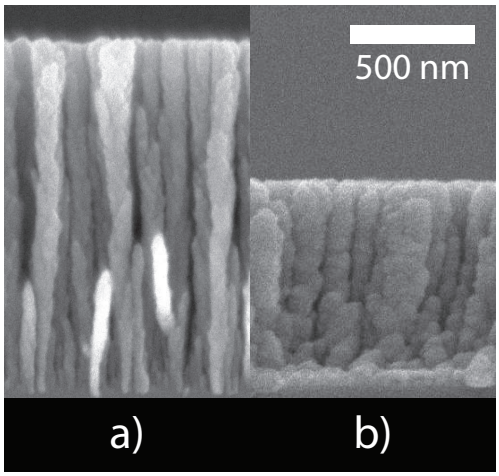

Figure 6.2. *Scanning electron microscope images for (a) standard and (b) 7 mA Ar-assisted GLAD RH films. Films were deposited at an incident vapour flux of* $81°$.

The SEM images in Fig. 6.2 show that film thickness and morphology are strongly dependent on argon current. As expected, the argon-assisted film appears more dense than the unassisted film. The capacitance values presented in Table 6.1 show that the capacitance of the RH sensors also vary with argon current, although these trends are less clear. It is observed that at 30% RH, C_S increases from $1.2\ \mathrm{nF}$ to $29\ \mathrm{nF}$ with argon current increasing from $0\ \mathrm{mA}$ to $7\ \mathrm{mA}$. The data in Fig. 6.3 shows that this trend holds for RH values below $\sim 50\%$. At RH values above 50%, Fig. 6.3 and Table 6.1 show

Table 6.1. *Deposition conditions, film thicknesses and capacitive response at 30% RH and 70% RH for Ar-assisted films*

Argon Current	Thickness	C_S @ 30% RH	C_S @ 70% RH
0 mA	1500 nm	1.2 nF	68 nF
7 mA	900 nm	29 nF	42 nF

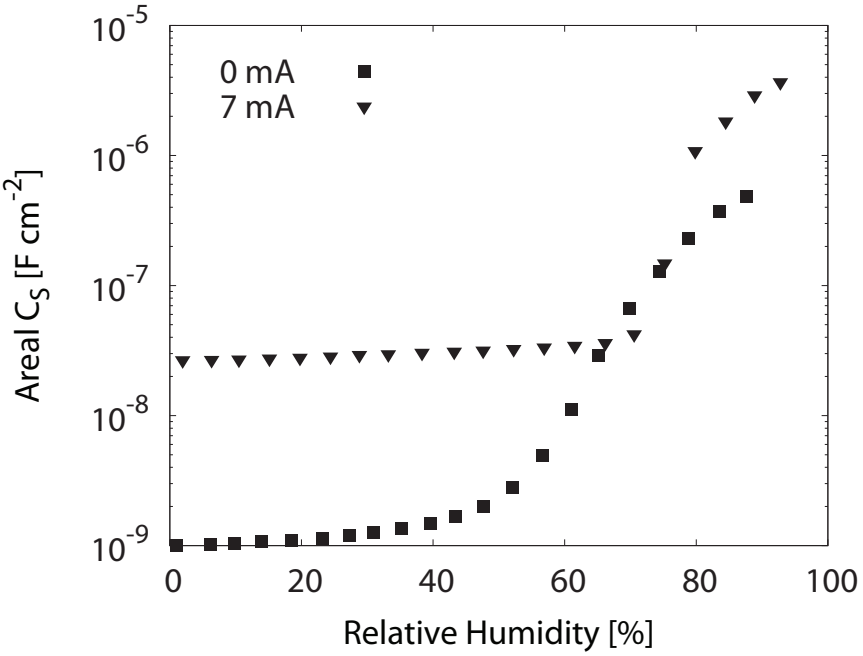

Figure 6.3. *Series capacitance of a standard GLAD RH sensor, and an Ar-assisted GLAD RH sensor using 7 mA argon current.*

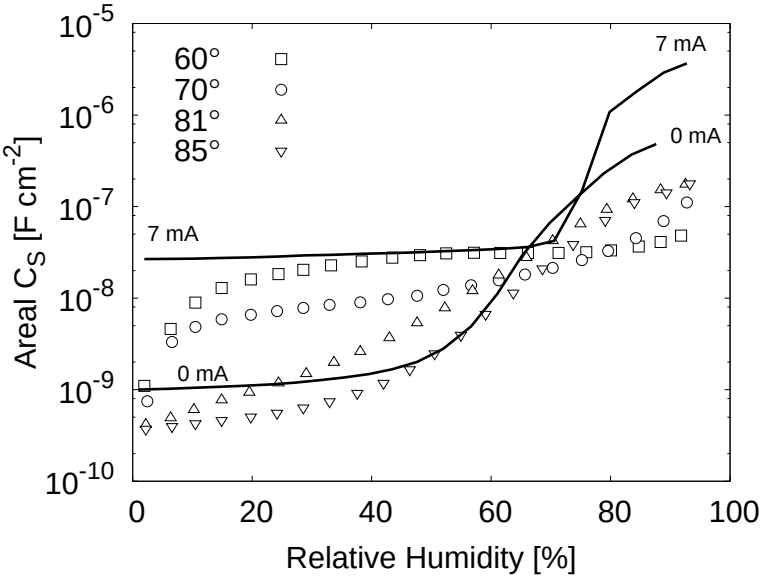

Figure 6.4. *Series capacitance of standard GLAD RH sensors deposited at different angles, compared with the 0 mA and 7 mA Ar-assisted GLAD RH sensors. Reproduced with permission from [146] ©2008 IEEE.*

that it no longer holds, which suggests that there may be competing processes occurring that influence the response in the high humidity regime.

An estimate of the average pore size in the $7\ \mathrm{mA}$ film was calculated using the Kelvin equation (Eq. 6.2) [161]. It is proposed that the sharp rises in the capacitive response is due to capillary condensation. For the $7\ \mathrm{mA}$ film, this occurs at a RH of approximately 70%. At this RH, the Kelvin equation predicts a characteristic water droplet diameter of approximately $6\ \mathrm{nm}$. This estimate of the droplet size is too small to suggest that capillary condensation is occuring between columns and instead implies that the condensation is occuring in pores on the column surface. This characteristic pore size is of a similar order of mangitude, but larger than those reported in unassisted films [162].

This result suggests that the argon-assisted process is increasing the average pore size in the film, likely by removing or filling in the smallest pores while having a lower effect on the larger pores. Future experiments exploring the pore size distribution of the argon-assisted films through porosimetry and FIB/TEM methods would be helpful in improving understanding on the effect of argon-assisted deposition on pore size and water adsorption in these films.

$$ln\left(\frac{P}{P_0}\right) = \frac{2\gamma V_m}{rRT}. \tag{6.2}$$

The field lines in an interdigitated electrode (IDE) sensor are largely confined to a thickness which is equal to one quarter of the electrode period, with 95% of field lines confined within a thickness of one half of the IDE period [163–165]. Therefore, the capacitive response should increase with film thickness up to approximately $2\ \mu\mathrm{m}$. However, the data in Table 6.1 in general shows a higher capacitive response in the films fabricated with argon currents, even though the film is less thick. This suggests that the larger capacitive responses in the sample fabricated with argon assist is caused by increases in film density which arise as a result of the Ar-assisted process. To determine the dependence of sensitivity on film height, an analytic model similar to the Igreja model was used [164]. This model performs a conformal mapping of the IDE, allowing for the prediction of areal capacitance in multi-layered systems such as those presented here. In the Igreja model, the IDE device is split along the plane of the IDE and each layer is treated separately, ie: the film and the substrate. The capacitance for each layer is given by Eq. 6.3, while the total capacitance is the sum of the capacitances of each

Table 6.2. *Equations used in the calculation of C'_I and C'_E for a finite layer.*

	Interior Electrodes	Exterior Electrodes
	$C'_I = L\frac{K(k_I)}{K(k'_I)}$	$C'_E = L\frac{K(k_E)}{K(k'_E)}$
Complete Elliptic Integral of the First Kind [166]	$K(k) = \int_0^{\frac{\pi}{2}} \frac{1}{\sqrt{1-k^2 sin^2\theta}}\,\mathrm{d}\theta$	$K(k) = \int_0^{\frac{\pi}{2}} \frac{1}{\sqrt{1-k^2 sin^2\theta}}\,\mathrm{d}\theta$
	$k'_I = \sqrt{1-{k_I}^2}$	$k'_E = \sqrt{1-{k_E}^2}$
	$k_I = t_2\sqrt{\frac{{t_4}^2-1}{{t_4}^2-{t_2}^2}}$	$k_E = \frac{1}{t_3}\sqrt{\frac{{t_4}^2-{t_3}^2}{{t_4}^2-1}}$
	$t_2 = sn(K(k)\eta, k)$	$t_3 = cosh\left(\frac{\pi(1-\eta)}{8r}\right)$
	$t_4 = \frac{1}{k}$	$t_4 = cosh\left(\frac{\pi(\eta+1)}{8r}\right)$
Metallization Coefficient	$\eta = \frac{W}{W+G}$	$\eta = \frac{W}{W+G}$
	$k = \left(\frac{v_2(0,q)}{v_3(0,q)}\right)^2$	
Jacobi Theta Function [166]	$v_2(0,q) = \sum_{n=-\infty}^{\infty} q^{\left(n+\frac{1}{2}\right)^2}$	
Jacobi Theta Function [166]	$v_3(0,q) = \sum_{n=-\infty}^{\infty} q^{n^2}$	
	$q = exp(-4\pi r)$	
	$r = \frac{h}{\lambda}$	
IDC Spatial Wavelength	$\lambda = 2(W+G)$	
Film/Substrate Thickness	h	
IDE Finger Width	W	W
IDE Finger Length	L	L
IDE Gap Width	G	G

individual layer.

$$C = \epsilon_0\epsilon_r\left[(N-3)\frac{C'_I}{2} + 2\frac{C'_I C'_E}{C'_I + C'_E}\right]. \tag{6.3}$$

Here, ϵ_0 is the vacuum dielectric constant, ϵ_r is the relative dielectric constant of the layer, N is the number of electrodes, C'_I and C'_E are slightly modified versions of the Igreja definitions [164], found in [7]. Expressions used in calculating the capacitance are given in Tables 6.2 and 6.3. This model has been used to reproduce the model output of Igreja and Dias, and has obtained reasonable agreement with the Igreja model for uncoated IDE substrates [7].

Table 6.3. *Equations used in the calculation of the Jacobi Elliptic Function $sn(u,m)$ [166].*

Equation
$sn(u,m) = \frac{2\pi}{m^{\frac{1}{2}}K}\sum_{n=0}^{\infty}\frac{q^{n+\frac{1}{2}}}{1-q^{2n+1}}sin(2n+1)v$
$q = exp(-\pi\frac{K'}{K})$
$K'(m_1) = K(m)$
$m + m_1 = 1$
$v = \frac{\pi u}{2K}$

To derive an expression for the IDE sensitivity as a function of height, the areal capacitance of an IDE substrate coated with solid TiO_2 films of varying thickness was calculated with the model. The films used in this calculation were modelled using Tait's density approximation (Eq. 1.1) for titanium dioxide grown at a deposition angle of $\alpha = 81°$. The results of this calculation are given in Fig. 6.5 with 1 of every 100 data points given. The gap in data between film thicknesses of 0 nm and 750 nm are due to numerical limitations from using a double precision float in the Igreja model. When the trend in areal capacitance with film thickness is fit, a 1-e length of 1.707 ± 0.001 μm is obtained.

An expression for the incremental change in capacitance ($I\Delta C$) was also determined from this fit. This expression is shown in Fig. 6.5, in units of % nm^{-1}.

$$I\Delta C = 0.0586exp(-x/1707)[\%nm^{-1}]. \tag{6.4}$$

Here, x is the location in space in units of nm. The results on the in-

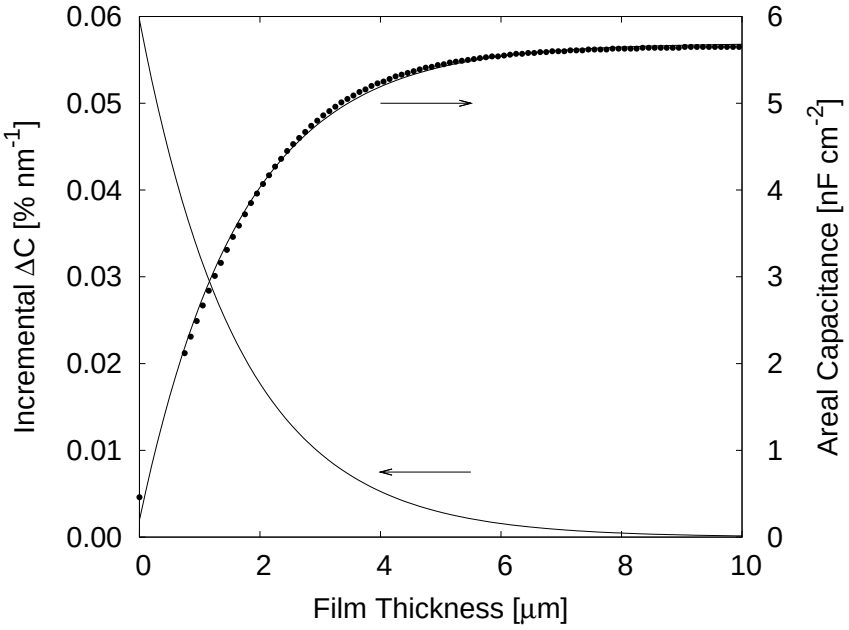

Figure 6.5. *Incremental change in capacitance ($I\Delta C$, Eq. 6.4) and areal capacitance as a function of film thickness.*

cremental capacitance presented in Fig. 6.5 confirm high sensitivity in the volume closest to the IDE electrodes. Since the use of argon bombardment increases the film density throughout the entire film thickness, the increase in dielectric constant near the IDE surface where the field lines are most concentrated leads to an increase in the sensor capacitance as observed in Figs. 6.3 and 6.4. This change in film morphology at the IDE interface is primarily responsible for the change in capacitive response in the Ar-assisted sensors.

GLAD film density can also increase with decreasing deposition angle [24,26]. When the unassisted film fabricated at 81° is compared with the unbombarded film fabricated in an argon environment at the same deposition angle, the capacitive responses are different. This would suggest that the variation in deposition gases and post-deposition treatments have an effect on the capacitive response to humidity. However, a much larger difference in the capacitive response is observed when the responses of the high density unassisted GLAD film grown at 60° and the $7\ \mathrm{mA}$ Ar-assisted GLAD film are compared in Fig. 6.4. This would suggest that in addition to the deposition gases and post-deposition treatments, the argon bombardment has an additional influence on the resulting capacitive response. Ar-assisted GLAD provides an additional degree of freedom in tuning the properties of thin film humidity sensors. While the use of Ar-assisted deposition was successful in improving the magnitude of the capacitive response over the entire humidity range, for RH below approximately 50% the unassisted sensors demonstrated higher sensitivity. As a result, future studies should look at improving the sensitivity in this regime through optimization of the deposition angle and argon conditions.

6.5 Conclusion

The Ar-assisted GLAD process was used to modify the film morphology in vertical post titanium dioxide humidity sensors. Here, the capacitive response was found to increase with argon assistance for relative humidity values below 50%, whereas above 50% the trend in the response was more complicated, suggesting that there are competing factors at play which influence the response in the high humidity regime. When film thickness was taken into account, the results suggest an increase in film density with argon assist, which is expected for argon assist.

When the effects of argon bombardment on the capacitive response are compared with the effects of deposition gas and post-deposition oxidation, argon bombardment is observed to have a larger impact. Argon bombardment was shown to increase the capacitive response by about one order of magnitude over most of the humidity range. In addition, the argon-assisted film was observed to have a response which is larger in magnitude than a dense unassisted film over the entire humidity range. An analytical model was used to provide insight as to why higher capacitive responses were seen in the Ar-assisted sensors. It was found that the capacitive sensor was most sensitive to changes in film morphology near the IDE interface, where the strongest electric field is found, and increases in film density due to argon bombardment lead to increases in capacitance. Also, while there were observable effects from varying the deposition gas and including a post-deposition oxidation treatment, these effects were more subtle than those observed with argon bombardment. Instead of large changes in overall magnitude, the shape of the response curve was modified, which indicates changing sen-

sitivities in different humidity ranges. It is proposed that the argon-assisted process is affecting the pore size distribution by increasing the average pore size. Future studies have been proposed to explore this further.

This preliminary study has demonstrated that Ar-assisted deposition can provide additional control over the capacitive response in thin film humidity sensors by modifying the film morphology, and that this process can be used to obtain responses to humidity that are different from those obtainable with unassisted thin films. Future optimization of Ar-assisted humidity sensing films may yield devices with performance enhancements over unassisted films.

Chapter 7

Conclusion

7.1 Summary

This thesis has described the extension of the glancing angle deposition process through bombardment with energetic neutrals. The unique film morphologies which arise as a result were studied, and various applications for this modified process were pursued. This research can be categorized into three different areas:

1. The Ar-assisted glancing angle deposition process, with focus on considerations arising from system geometry, and the mechanisms responsible for film morphology modification (Chapter 2).

2. The effect of changing bombardment conditions on numerous film properties (Chapter 3).

3. Applications which arise from the creation of unique film morphologies through energetic bombardment (Chapters 4-6).

In the first section, characterization of the Ar-assisted GLAD process was performed to provide insights into the modification of film morphology and lay the groundwork for understanding the observed changes in the properties of bombarded films. After an introductory chapter, which outlines the unassisted GLAD process and the various characterization processes used, a definition of the system geometry used for the Ar-assisted deposition process was discussed as well as a characterization of the beam of energetic argon neutrals. The energetic neutral dose non-uniformities arising from system geometry and beam shape, and their consequences, are outlined. In addition, the latter half of this section provides significant insight into the dominant mechanisms responsible for film morphology modification in the Ar-assisted process. Sputter yields were found which closely agree with those presented in the literature. Further calculation using these sputter yields gives a deposited to sputtered film molecule ratio of approximately 9 to 1. When this ratio is compared with observations of non-uniformities observed in Ar-assisted films, it is found that sputtering accounts for no more than 25% of the total non-uniformity, indicating that sputtering is a significant process, but not solely responsible for the observed film morphology modification. In addition to sputtering, bombardment-induced surface diffusion was also investigated and compared with sources of surface diffusion present in the unassisted GLAD process. In unassisted GLAD, the dominant source of surface diffusion was determined to be radiant heating from the material source, which was found to a approximately an order of magnitude larger than the contribution from film flux condensation on the substrate. In Ar-assisted GLAD, entrapment and momentum transfer through interactions of energetic neutrals with the film were both found to be significant factors. When these

two factors, which arise from the energetic argon source, are compared to the unassisted sources, they were found to be 1.4 - 47 times larger than the sum of the unassisted substrate heating mechanisms. This indicates that substrate heating from the energetic argon source is also significant.

In the second section, a number of film property modifications were investigated. Studies on film density in porous films indicate increases in film density with argon bombardment for a large number of materials with larger increases occurring at higher deposition angles. Film density studies on dense films indicate that in most cases, higher as-deposited film densities are observed in amorphous films than in polycrystalline films. Column tilt angle studies show an increase in tilt angle with increasing ion dose as well as film material deposition rate. In addition, amorphous films were found to obey a material-independent trend where larger increases in tilt angle are observed for materials which have smaller unassisted tilt angles. Ar-assisted films grown with the phisweep process were found to have trends in column tilt angle, film density, and in-plane birefringence which are consistent with those found in unassisted films for changing phisweep angles. In general, increases in film density and column tilt angle arising from energetic bombardment lead to increases in the principal refractive indices and a decrease in the normalized in-plane birefringence, respectively. Studies on thin film surface area indicate a reduction in the specific surface area with energetic bombardment, but no clear trends in surface area enhancement. These results collectively provide a significant foundation for targeting specific thin film applications.

In the third section, Ar-assisted GLAD films were studied as candidates in a number of applications. First, Ar-assisted square spiral films were fabricated with increased column tilt which more closely resemble optimal simulated values. This may lead to significant performance improvements which would increase the viability of GLAD-based photonic crystal devices. Second, argon bombardment during the growth of helical circular polarization filters was found to improve selective circular behaviour over unassisted filters. This allows Ar-assisted filters to be fabricated which have equivalent performance to thicker unassisted films. Lastly, studies on Ar-assisted humidity sensors have shown increases in the capacitive signal with argon bombardment. This may lead to devices with improved signal-to-noise ratio, which may permit the fabrication of devices with higher sensitivity.

7.2 Recommendations for Future Work

7.2.1 Substrate Temperature

Studies of substrate temperature would be quite useful in separating the effects of sputtering and surface diffusion in the Ar-assisted process. Substrate heating can be used to determine whether or not the unique film morphologies observed in Ar-assisted films can be duplicated without the need for bombardment. Further investigation in this area could explore the nucleation process under elevated substrate temperature and with bombardment. This would help address how much of an extent the nucleation process has on the resulting film morphology. These studies would probe fundamental questions on GLAD growth which could prove to be significant contributions to film growth theory.

7.2.2 Column Tilt Angle

The material independent trend found for column tilt angle modification in amorphous Ar-assisted films encourage significant further study. Determining how this trend changes with deposition angle and bombardment angle should provide additional insight into the Ar-assisted growth process and would be useful in determining appropriate candidate materials for the fabrication of inverse square spiral templates for GLAD-based photonic crystal structures. Other avenues of research in this area which remain to be investigated include determining whether a similar trend exists for polycrystalline films, amorphous materials with low unassisted column tilt angles, and for structures on seeded substrates. This latter topic is of particular importance with respect to photonic crystal structures.

7.2.3 Uniformity

While improving the uniformity isn't a particularly difficult problem to solve, doing so would allow for further studies into surface area enhancement in Ar-assisted films. Since a fairly large substrate area is needed for surface area measurement, improvements in film uniformity would provide the opportunity to obtain surface area enhancement measurements that are more characteristic of the entire film, which could prove to be useful in sensing applications.

7.2.4 Ar-Assisted Square Spiral Films

The Ar-assisted square spiral results presented here show promise since they can be fabricated with optimal column tilt angle, however, improvements in the column cross-section and film density need to be made before a full three-

dimensional bandgap can be fully realized. Modification of substrate seeding can most likely be used to improve column cross-section. Engineered substrate topographies have been shown to have a large impact on film morphology [129]. Careful design and implementation of anisotropic seed shapes should induce an in-plane column growth anisotropy which would translate into a more isotropic column cross-section in the effective column growth direction. Optimizing the film density will most likely need to be achieved through optimization of the deposition angle and the argon flux.

7.2.5 Helical Ar-Assisted Films

The Ar-assisted circular polarization filter results presented in this thesis show superior selective behaviour over optimized unassisted filters. The performance of these Ar-assisted filters may be further enhanced by optimization of the deposition and bombardment conditions. This includes optimization of the material deposition rate, energetic argon flux, and argon energy. Ar-assisted deposition may also be attempted with the growth of organic materials such as Alq_3, where Hrudey *et al.* have reported large selective behaviour in unassisted helical Alq_3 films [167].

7.2.6 Humidity Sensing

Currently, the understanding of the capacitive response curve shape is limited. Porosimetry measurements, which focus on the pore size distribution, would be valuable in improving the understanding of the device adsorption and desorption physics. This would in turn permit a more specialized design which can target specific applications. The recent development of the use of krypton gas for pore size analysis make such analysis on both Ar-assisted and

unassisted humidity sensors a high priority [162].

7.2.7 Ar-Assisted VLS-GLAD

It has been demonstrated that the use of GLAD in conjunction with vapour-liquid-solid (VLS) growth can provide substantial control over morphology in the growth of nanowhiskers [168]. In addition, VLS growth has been shown to be compatible with ion bombardment, which allows for VLS growth at lower substrate temperatures [169]. The use of Ar-assisted VLS-GLAD growth may reduce the substrate heating requirements while still providing the extensive control over nanowhisker morphology by GLAD, and may also enable additional options for controlling VLS-GLAD nanowhisker growth.

References

[1] T. Harper. Global funding of nanotechnologies and its impact. Technical report, Cientifica Ltd., 2011.

[2] M. Faraday. Experimental relations of gold (and other metals) to light. *Phil. Trans. Roy. Soc. London*, 147:145 – 181, 1857.

[3] W. R. Grove. On the electro-chemical polarity of gases. *Phil. Trans. Roy. Soc. London*, 142:87 – 101, 1852.

[4] L. Holland. The effect of vapor incidence on the structure of evaporated aluminum films. *J. Opt. Soc. Am.*, 43:376 – 380, 1953.

[5] N. Young and J. Kowal. Optically active fluorite films. *Nature*, 183:104 – 105, 1959.

[6] S. R. Kennedy, M. J. Brett, O. Toader, and S. John. Fabrication of tetragonal sqare spiral photonic crystals. *Nano Lett.*, 2:59 – 62, 2002.

[7] J. Steele, M. Taschuk, and M. Brett. Nanostructured metal oxide films for humidity sensors. *IEEE Sens. J.*, 8(8):1422 – 1429, 2008.

[8] K. D. Harris, D. Vick, E. J. Gonzalez, T. Smy, K. Robbie, and M. J. Brett. Porous thin films for thermal barrier coatings. *Surface and Coatings Technol.*, 138:185 – 191, 2001.

[9] S. R. Kennedy and M. J. Brett. Porous broadband antireflection coating by glancing angle deposition. *Applied Optics*, 42:4573 – 4579, 2003.

[10] J. Van Dijken, M. Fleischauer, and M. Brett. Controlled nanostructuring of cupc thin films via glancing angle deposition for idealized organic photovoltaic architectures. *J. Mat. Chem.*, 21(4):1013 – 1019, 2011.

[11] S. Chaney, S. Shanmukh, R. Dluhy, and Y-P. Zhao. Aligned silver nanorod arays produce high sensitivity surface-enhanced raman spectroscopy substrates. *Appl. Phys. Lett.*, 87:031908, 2005.

[12] D. Vick, Y. Y. Tsui, M. J. Brett, and R. Fedosejevs. Production of porous carbon thin films by pulsed laser deposition. *Thin Solid Films*, 350:49 – 52, 1999.

[13] J. Sit, D. Vick, and M. J. Brett. Thin film microstructure control using glancing angle deposition by sputtering. *J. Mater. Res.*, 14:1197 – 1199, 1999.

[14] K. Robbie and M. J. Brett. Sculptured thin films and glancing angle deposition: Growth mechanics and applications. *J. Vac. Sci. Technol. A*, A 15:1460 – 1465, 1997.

[15] R. W. Vook. Structure and growth of thin films. *Int. Met. Rev.*, 27:209 – 245, 1982.

[16] K. Reichelt. Nucleation and growth of thin films, 1988.

[17] J. A. Venables, G. D. T. Spiller, and M. Hanbucken. Nucleation and growth of thin films. *Rep. Prog. Phys.*, 47:399 – 459, 1984.

[18] J. A. Venables. Atomic processes in crystal growth. *Surf. Sci.*, 299-300:798 – 817, 1994.

[19] B. A. Movchan and A. V. Demchishin. Study of the structure and properties of thick vacuum condensates of nickel, titanium, tungsten, aluminum oxide and zirconium oxide. *Phys. Met. Metallogr.*, 28:83 – 90, 1969.

[20] H. T. G. Hentzell, C. R. M. Grovenor, and D. A. Smith. Grain-structure variation with temperature for evaporated metal films. *J. Vac. Sci. Tech. A*, 2:218 – 219, 1984.

[21] J. V. Sanders. Chemisorption and reactions on metal films. *Academic Press*, 1, 1971.

[22] J. A. Thornton. High-rate thick film growth. *Annu. Rev. Mater. Sci.*, 7:239 – 260, 1977.

[23] A. Dirks and H. Leamy. Columnar microstructure in vapor-deposited films. *Thin Solid Films*, 47:219 – 233, 1977.

[24] R.N. Tait, T. Smy, and M.J. Brett. Modelling and characterization of columnar growth in evaporated films. *Thin Solid Films*, 226:196 – 201, 1993.

[25] I. Hodgkinson, Q. Wu, and J. Hazel. Empirical equations for the principal refractive indices and column angle of obliquely deposited films of tantalum oxide, titanium oxide, and zirconium oxide. *Appl. Opt.*, 37:2653 – 2659, 1998.

[26] J. J. Steele, J. P. Gospodyn, J. C. Sit, and M. J. Brett. Impact of morphology on high-speed humidity sensor performance. *IEEE Sensors Journal*, 6:24 – 27, 2006.

[27] J. J. Steele and M. J. Brett. Nanostructure engineering in porous columnar thin films: recent advances. *J. Mater. Sci. Mater. Electron*, 18:367 – 369, 2007.

[28] M. Jensen and M. Brett. Porosity engineering in glancing angle deposition thin films. *Appl. Phys. A: Mater. Sci. Process.*, 80:763 – 768, 2005.

[29] M. Summers and M. Brett. Optimization of periodic column growth in glancing angle deposition for photonic crystal fabrication. *Nanotechnology*, 19:415203, 2008.

[30] G. Kiema, M. Jensen, and M. Brett. Glancing angle deposition thin film microstructures for microfluidics applications. *Chem. Mater.*, 17:4046 – 4048, 2005.

[31] I. Hodgkinson, Q. Wu, M. Brett, and K. Robbie. Vacuum deposition of biaxial films with surface-aligned principal axes and large birefringence dn. *Optical Interference Coatings*, 9:104 – 106, 1998.

[32] I. Hodgkinson and Q. Wu. Serial bideposition of anisotropic thin films with enhanced linear birefringence. *Appl. Opt.*, 38:3621 – 3625, 1999.

[33] A. van Popta, J. Cheng, J. Sit, and M. Brett. Birefringence enhancement in annealed tio2 thin films. *J. Appl. Phys.*, 102(013517):013517–013517–7, 2007.

[34] S. Aisenberg and R. Chabot. Ion beam deposition of diamondlike carbon. *J. Appl. Phys.*, 42:2953 – 2958, 1971.

[35] S. Aisenberg and F. Kimrock. Ion beam and ion-assisted deposition of diamond-like carbon films. *Mat. Sci. Forum*, 52-53(1):1 – 40, 1990.

[36] S. Aisenberg and R. Chabot. Physics of ion plating and ion beam deposition. *J. Vac. Sci. Technol.*, 10(1):104 – 107, 1973.

[37] G. Gautherin and C. Weissmantel. Some trands in preparing film structures by ion beam methods. *Thin Solid Films*, 50:135 – 144, 1978.

[38] C. Weissmantel, G. Reisse, H.-J. Erler, F. Henny, K. Bewilogua, U. Ebersbach, and C. Schurer. Preparation of hard coatings by ion beam methods. *Thin Solid Films*, 63:315 – 325, 1979.

[39] C. Weissmantel, k. Bewilogua, K. Breuer, D. Dietrich, U. Ebersbach, H.-J. Erler, B. Rau, and G. Reisse. Preparation and properties of hard i-c and i-bn coatings. *Thin Solid Films*, 96:31 – 44, 1982.

[40] S. Fujimori, T. Kasai, and T. Inamura. Carbon film formation by laser evaporation and ion beam sputtering. *Thin Solid Films*, 92:71 – 80, 1982.

[41] M. Kitabatake and K. Wasa. Growth of diamond at room temperature by an ion beam sputter deposition under hydrogen ion bombardment. *J. Appl. Phys.*, 58:1693 – 1695, 1985.

[42] N. Savvides and B. Window. Diamondlike amorphous carbon films prepared by magnetron sputtering of graphite. *J. Vac. Sci. Technol. A*, 3(6):2386 – 2390, 1985.

[43] N. Savvides. Fourfold to threefold transition in diamondlike amorphous carbon films: A study of optical and electrical properties. *J. Appl. Phys.*, 58:518 – 521, 1985.

[44] S. Pellicori, C. Peterson, and T. Henson. Transparent carbon films: Comparison of properties between ion and plasma deposition processes. *J. Vac. Sci. Technol. A*, 4:2350 – 2355, 1986.

[45] N. Savvides. Optical constants and associated functions of metastable diamondlike amorphous carbon films in the energy range 0.5-7.3 ev. *J. Appl. Phys.*, 59:4133 – 4145, 1986.

[46] K. Ogata, Y. Andoh, and E. Kamijo. Crystallization of carbon films by ion beam assist technology. *Nuc. Instrum. Phys. Res.*, B33:685 – 688, 1988.

[47] M. Kitabatake and K. Wasa. Diamond films by ion-assisted deposition at room temperature. *J. Vac. Sci. Technol. A*, 6(3):1793 – 1797, 1988.

[48] L. Zhou, K. Kato, N. Umehara, and Y. Miyake. Friction and wear properties of hard coating materials on textured hard disk sliders. *Wear*, 243:133 – 139, 2000.

[49] C. Kennemore and U. Gibson. Ion beam processing for coating mgf2 onto ambient temperature substrates. *Appl. Opt.*, 23(20):3608 – 3611, 1984.

[50] E. Donovan, D. van Vechten, A. Kahn, C. Carosella, and G. Hubler. Near infrared rugate filter fabrication by ion beam assisted deposition of si(1-x)nx films. *Appl. Opt.*, 28(14):2940 – 2944, 1989.

[51] T. Miyano and H. Kitamura. Coating on the cutting edge of an electric shaver by ion beam assisted deposition. *Surface Coatings and Technology*, 65:179 – 183, 1994.

[52] B. Johs, J. Woollam, C. Herzinger, J. Hilfiker, R. Synowicki, and C. Bungay. *Optical Metrology*, volume CR72 of *Proc. SPIE*, chapter Overview of variable-angle spectroscopic ellipsometry (VASE): II. Advanced applications, pages 29 – 58. SPIE, 1999.

[53] C. Borhen and D. Huffman. *Absoprtion and scattering of light by small particles*, pages 44 – 56. Wiley, 1983.

[54] S. Brunauer, P. Emmett, and E. Teller. Adsorption of gases in multimolecular layers. *J. Am. Chem. Soc.*, 60:309 – 319, 1938.

[55] I. Langmuir. The constitution and fundamental properties of solids and liquids. *J. Am. Chem. Soc.*, 138:2221 – 2295, 1916.

[56] S. Lowell, J. Shields, M. Thomas, and M. Thommes. *Characterization of porous solids and powders: surface area, pore size, and density*, chapter Vacuum volumetric measurements (manometry), pages 250 – 251. Kluwer Academic Publishers, 2004.

[57] K. Krause, M. Taschuk, K. Harris, D. Rider, N. Wakefield, J. Sit, J. Buriak, M. Thommes, and M. Brett. Surface area characterization of obliquely deposited metal oxide nanostructured thin films. *Langmuir*, 26:4368 – 4376, 2010.

[58] M. Abramoff, P. Magelhaes, and S. Ram. Image processing with imagej. *Biophotonics International*, 11(7):36 – 42, 2004.

[59] R. W. Barr. Dynamic electron emitter, 4 1988.

[60] N. Wakfield and J. Sit. On the uniformity of films fabricated by glancing angle deposition. *J. Appl. Phys.*, 109:084332, 2011.

[61] J. Sorge, M. Taschuk, N. Wakefield, J. Sit, and M. Brett. Metal oxide morphology in argon-assisted glancing angle deposition. *J. Vac. Sci. Technol. A*, 30:021507, 2012.

[62] L. Nghi and R. Kelly. Phnomnes de pulvrisation et de distribution en profondeur. partie iv. pulvrisation cathodique des oxydes nb2o5, ta2o5 et wo3. *Can. J. Phys.*, 48:137 – 145, 1970.

[63] A. Stirling and W. Westwood. Reactive sputtering of nickel, iron, and nickel ferrite. *Thin Solid Films*, 8:199 – 205, 1971.

[64] A. Elbern and P. Mioduszewski. Measurement of the sputtering yield of fe from an oxidized stainless steel target using a pulsed dye laser. *J. Vac. Sci. Technol.*, 16(6):2090 – 2092, 1979.

[65] Comparison of the sputter rates of oxide films relative to the sputter rate of sio2. *J. Vac. Sci. Technol. A*, 28(5):1060 – 1072, 2010.

[66] P. Martin, H. MacLeod, R. Netterfield, C. Pacey, and W. Sainty. Ion-beam-assisted deposition of thin films. *Appl. Opt.*, 21(1):178 – 184, 1983.

[67] W. Sainty, R. Netterfield, and P. Martin. Protective dielectric coatings produced by ion-assisted deposition. *Appl. Opt.*, 23(7):1116 – 1119, 1984.

[68] P. Martin. Ion-based methods for optical thin film deposition. *J. Mat. Sci.*, 21(1):1 – 25, 1986.

[69] P. Martin. Ion-assisted thin film deposition and applications. *Vacuum*, 36(10):585 – 590, 1986.

[70] S. Rossnagel and J. Cuomo. Ion beam bombardment deposition during film deposition. *Vacuum*, 38:73 – 81, 1988.

[71] U. Gibson. Ion beam processing of optical thin films. *Mater. Res. Soc. Symp. Proc.*, 152:105 – 114, 1989.

[72] T. Kyogoku, T. Suzuki, and M. Mino. Ion beam assisted deposition of a thin film coating on a gradient-index lens array. *Appl. Opt.*, 29(28):4071 – 4076, 1990.

[73] N. Sonnenberg, A. Longo, M. Cima, B. Chang, K. Ressler, P. McIntyre, and Y. Liu. Preparation of biaxially aligned cubic zirconia films on pyrex glass substrates using ion-beam assisted deposition. *J. Appl. Phys.*, 74(2):1027 – 1034, 1993.

[74] S. Mohan and M. Krishna. A review of ion beam assisted deposition of optical thin films. *Vacuum*, 46(7):645 – 659, 1995.

[75] H. Cho and C. Hwangbo. Optical inhomogeneity and microstructure of zro(2) thin films prepared by ion-assisted deposition. *Appl. Opt.*, 35(28):5545 – 5552, 1996.

[76] W. Ensinger. Low energy ion assist during deposition an effective tool for controlling thin film microstructure. *Nucl. Instrum. Meth. B*, 127-128(97):796 – 808, 1997.

[77] Q. Tang, K. Kikuchi, S. Ogura, and A. MacLeod. Mechanism of columnar microstructure growth in titanium oxide thin films deposited by ion-beam assisted deposition. *J. Vac. Sci. Technol. A*, 17(6):3379 – 3384, 1999.

[78] Y. Shimizu, S. Karino, Y. Takao, T. Hyodo, K. Baba, and M. Egashira. Improvement of long-term stability of thin film gas sensors by ion beam-assisted deposition. *J. Electrochem. Soc.*, 147(11):4379 – 4384, 2000.

[79] F. Gracia, J. Holgado, L. Contreras, T. Girardeau, and A. Gonzalez-Elipe. Optical and crystallisation behaviour of tio2 and v/tio2 thin films prepared by plasma and ion beam assisted methods. *Thin Solid Films*, 429(1-2):84 – 90, 2003.

[80] C. Ma, J. Huang, and H. Chen. Texture evolution of transition-metal nitride thin films by ion beam assisted deposition. *Thin Solid Films*, 446(2):184 – 193, 2004.

[81] H. Chen, C. Lee, C. Jaing, M. Shiao, C. Lu, and F. Shieu. Effects of temperature on columnar microstructure and recrystallization of tio2 film produced by ion-assisted deposition. *Appl. Opt.*, 45(9):1979 – 1984, 2006.

[82] J. Bohdansky, J. Roth, and H. Bay. An analytical formula and important parameters for low-energy ion sputtering. *J. Appl. Phys.*, 51(5):2861 – 2865, 1980.

[83] M. Fleischauer, J. Sorge, R. Joseph, and M. Brett. Enhanced control of porous thin film morphology via ion bombardment. In *Self Assembly of Nanostructures Aided by Ion- or Photon-Beam Irradiation: Fundamentals and Applications*, volume 960 of *Material Research Society Symposium Proceedings*, pages 0960–N01–03, 2007.

[84] K-H. Muller. Ion-beam-induced epitaxial vapor-phase growth: A molecular-dynamics study. *Phys. Rev. B*, 35(15):7906 – 7913, 1987.

[85] M. Inghram, W. Chupka, and J. Berkowitz. Thermodynamics of the ta-o system: The dissociation energies of tao and tao2. *J. Chem. Phys.*, 27(2):569 – 571, 1957.

[86] V. Urusov. Heats of sublimation and estimates of effective atomic charges in essentially ionic crystals. *Zhurnal Strukturnoi Khimii*, 7(3):439 – 444, 1966.

[87] R. Colin, J. Drowart, and G. Verhaegen. Mass-spectrometric study of the vaporization of tin oxides. *T. Faraday Soc.*, 61:1364 – 1371, 1965.

[88] M. Wolff, J. Schultze, and H-H. Strehblow. Low-energy implantation and sputtering of tio2 by nitrogen and argon and the electrochemical reoxidation. *Surface and Interface Analysis*, 17(10):726 – 736, 1991.

[89] W. Eckstein and H. Verbeek. *Data on light ion reflection*. IPP / Max-Planck-Institut für Plasmaphysik. 1979.

[90] Y. Yamamura. Particle reflection and its energy spectrum from solid surfaces with adsorbate atoms. *Nuclear Instruments and Methods in Physics Research Section B: Beam Interactions with Materials and Atoms*, 33(1-4):429 – 431, 1988.

[91] J. Sorge and M. Brett. Film morphology modification in ion-assisted glancing angle deposition. *Thin Solid Films*, 519(4):1356 – 1360, 2010.

[92] M. Born and E. Wolf. *Principles of Optics: Electromagnetic Theory of Propagation, Interference and Diffraction of Light (7th ed.)*. Cambridge University Press, 1999.

[93] P. Martin, R. Netterfield, and W. Sainty. Modification of the optical and structural properties of dielectric zro2 films by ionassisted deposition. *J. Appl. Phys.*, 55:235 – 241, 1984.

[94] M. Al-Robaee, M. Krishna, K. Rao, and S Mohan. Optical properties of ion assisted deposited ceo2 films. *J. Vac. Sci. Technol. A*, 9(6):3048 – 3053, 1991.

[95] I. Shimizu, Y. Setsuhara, S. Miyake, H. Saitou, and M. Kumagai. Effects of ion-beam irradiation on morphology and densification of ceo2 films prepared by ion-beam-assisted deposition. *Jpn. J. Appl. Phys.*, 39:4138 – 4142, 2000.

[96] S. Lichter and J. Chen. Model for columnar microstructure of thin solid films. *Phys. Rev. Lett.*, 56(13):1396 – 1399, 1986.

[97] H. Fujiwara, K. Hara, M. Kamiya, T. Hasimoto, and K. Okamoto. Comment on the tangent rule. *Thin Solid Films*, 163:387 – 391, 1988.

[98] R.N. Tait, T. Smy, and M.J. Brett. Simulation and measurement of density variation in mo films sputter deposited over oxide steps. *J. Vac. Sci. Technol. A*, 8(3):1593 – 1596, 1990.

[99] I. Hodgkinson and Q.H. Wu. Ion-Beam Control of Thin-Film Microstructural Columnar Angle. *Mod. Phys. Lett. B*, Vol. 15:1328 – 1331, 2001.

[100] J. Taylor. *An introduction to error analysis*, chapter Covariance and Correlation, pages 209 – 226. University Science Books, 1997.

[101] D. Gish, M. Summers, and M. Brett. Morphology of periodic nanostructures for photonic crystals grown by glancing angle deposition. *Photonics Nanostruct. Fundam. Appl.*, 4:23 – 29, 2006.

[102] A. van Popta, M. Hawkeye, J. Sit, and M. Brett. Gradient-index narrow bandpass filters fabricated with glancing-angle deposition. *Opt. Lett.*, 29:2545 – 2547, 2004.

[103] K. Kaminska, T. Brown, G. Beydaghyan, and K. Robbie. Vacuum evaporated porous silicon photonic interference filters. *Appl. Opt.*, 42:4212 – 4219, 2003.

[104] Q. Wu, L. De Silva, M. Arnold, I. Hodgkinson, and E. Takeuchi. All-silicon polarizing filters for near-infrared wavelengths. *J. Appl. Phys.*, 95:402 – 404, 2004.

[105] K. Robbie, M. Brett, and A. Lakhtakia. Chiral sculpted thin films. *Nature*, 384:616, 1996.

[106] R. Sprague, C. Hickey, and I. Hodgkinson. The influence of argon ion bombardment on form birefringence in thin films of titania. *J. Appl. Phys.*, 17:3201 – 3203, 1992.

[107] J. Sorge, M. Summers, M. Fleischauer, K. Tabunshchyk, A. Kovalenko, and M.J. Brett. Ion Beam Assisted Square Spiral Photonic Crystal Fabrication. *MRS Proceedings*, Vol. 1014-AA07-26, 2007.

[108] J. Rayleigh. On the remarkable phenomenon of crystalline reflexion described by prof. stokes. *Phil. Mag.*, 26(160):256 – 265, 1888.

[109] V. Bykov. Spontaneous emission from a medium with a band spectrum. *Kvant. Elektron.*, 1:1557 – 1577, 1974.

[110] K. Ohtaka. Energy band of photons and low-energy photon diffraction. *Phys. Rev. B*, 19(10):5057 – 5067, 1979.

[111] E. Yablonovitch. Inhibited spontaneous emission in solid-state physics and electronics. *Phys. Rev. Lett.*, 58(20):2059 – 2062, 1987.

[112] S. John. Strong localization of photons in certain disordered dielectric superlattices. *Phys. Rev. Lett.*, 58(23):2486 – 2489, 1987.

[113] J. Knight, T. Birks, P. Russell, and D. Atkin. All-silica single-mode optical fiber with photonic crystal cladding. *Opt. Lett.*, 21(19):1547 – 1549, 1996.

[114] J. Knight, J. Broeng, T. Birks, and P. Russell. Photonic band gap guidance in optical fibers. *Science*, 282:1476 – 1478, 1998.

[115] E. Yablonovitch. Photonic crystals: Semiconductors of light. *Scientific American*, 285(6):47 – 55, 2001.

[116] J. Joannopoulos. *Photonic crystals: Molding the flow of light*. Princeton University Press, 2008.

[117] E. Yablonovitch, T. Gmitter, and K. Leung. Photonic band structure: The face-centered-cubic case employing nonspherical atoms. *Phys. Rev. Lett.*, 67(17):2295 – 2298, 1991.

[118] C. Cuisin, A. Chelnokov, J. Lourtioz, D. Decanini, and Y. Chen. Submicrometer resolution yablonovite templates fabricated by x-ray lithography. *Appl. Phys. Lett.*, 77(6):770 – 772, 2000.

[119] S. Lin, J. Fleming, D. Hetherington, B. Smith, R. Biswas, K. Ho, M. Sigalas, W. Zubrzycki, S. Kurtz, and J. Bur. A three-dimensional photonic crystal operating at infrared wavelengths. *Nature*, 394:251 – 253, 1998.

[120] A. Tandaechanurat, S. Ishida, D. Guimard, M. Nomura, S. Iwamoto, and Y. Arakawa. Lasing oscillation in a three-dimensional photonic crystal nanocavity with a complete bandgap. *Nature Photonics*, 5:91 – 94, 2011.

[121] A. Blanco, E. Chomski, S. Grabtchak, M. Ibisate, S. John, S. Leonard, C. Lopez, F. Meseguer, H. Miguez, J. Mondia, G. Ozin, O. Toader, and H. van Driel. Large-scale synthesis of a silicon photonic crystal with a complete three-dimensional bandgap near 1.5 micrometres. *Nature*, 405:437 – 440, 2000.

[122] W. Lee, S. Pruzinsky, and P. Braun. Multi-photon polymerization of waveguide structures within three-dimensional photonic crystals. *Adv. Mater.*, 14(4):271 – 274, 2002.

[123] K. Seet, V. Mizeikis, S. Matsuo, S. Juodkazis, and H. Misawa. Three-dimensional spiral-architecture photonic crystals obtained by direct laser writing. *Adv. Mater.*, (17):541 – 545, 2005.

[124] O. Toader and S. John. Proposed square spiral microfabrication architecture for large three-dimensional photonic band gap crystals. *Science*, 292:1133 – 1135, 2001.

[125] O. Toader and S. John. Square spiral photonic crystals: Robust architecture for microfabrication of materials with large three-dimensional photonic band gaps. *Phys. Rev. E*, 66:016610, 2002.

[126] M. Summers, K. Tabunshchyk, A. Kovalenko, and M. Brett. Fabrication of 2d-3d photonic crystal heterostructures by glancing angle deposition. *Photonics and Nanostructures - Fundamentals and Applications*, 7:76 – 84, 2009.

[127] S. R. Kennedy and M. J. Brett. Advanced techniques for the fabrication of square spiral photonic crystals by glancing angle deposition. *J. Vac. Sci. Technol. B*, 22:1184 – 1190, 2004.

[128] S. Johnson and J. Joannopoulos. Block-iterative frequency-domain methods for maxwell's equations in a planewave basis. *Opt. Express*, 8:173 – 190, 2001.

[129] M. Summers, B. Djurfors, and M. Brett. Fabrication of silicon submicrometer ribbons by glancing angle deposition. *J. Microlith. Microfab. Microsyst.*, 4(3):033012–1 – 033012–5, 2005.

[130] J. Sorge, A. van Popta, J. Sit, and M. Brett. Circular birefringence dependence on chiral film morphology. *Optics Express*, 14:10550 – 10557, 2006.

[131] T. Motohiro and Y. Taga. Thin film retardation plate by oblique deposition. *Appl. Opt.*, 28:2466 – 2482, 1989.

[132] R. Azzam. Chiral thin solid films: method of deposition and applications. *Appl. Phys. Lett.*, 61:3118 – 3120, 1992.

[133] A. Lakhtakia and W. Weiglhofer. On light propagation in helicoidal bianisotropic mediums. volume 448 of *P. Roy. Soc. Lond. A*, pages 419 – 437, 1995.

[134] K. Robbie and M. Brett. Method of depositing shadow sculpted thin films, 02 1999.

[135] K. Robbie and M. Brett. Shadow sculpted thin films, 06 2001.

[136] K. Robbie and M. Brett. Glancing andgle deposiiton of thin films, 03 2001.

[137] S. R. Kennedy, M. J. Brett, H. Miguez, O. Toader, and S. John. Optical properties of a three-dimensional silicon square spiral photonic crystal. *Photonics Nanostruct.*, 1:37 – 42, 2003.

[138] Y. Zhao, D. Ye, P. Wang, G. Wang, and T. Lu. Fabrication of si nanocolumns and si square spirals of self-assembled monolayer colloid substrates. *Int. J. Nanosci.Ser.*, 1:87 – 97, 2002.

[139] S. Kennedy, J. Sit, D. Broer, and M. Brett. Optical activity of chiral thin film and liquid crystal hybrids. *Liq. Cryst.*, 28:1799 – 1803, 2001.

[140] A. Chutinan and S. Noda. Spiral three-dimensional photonic-band-gap structure. *Phys. Rev. B*, 57:2006 – 2008, 1998.

[141] A. Lakhtakia, M. McCall, J. Sherwin, Q. Wu, and I. Hodgkinson. Sculpted-thin-film spectral holes for optical sensing of fluids. *Opt. Commun.*, 194:33 – 46, 2001.

[142] J. Broughton and M. Brett. Electrochemical capacitance in manganese thin films with chevron microstructure. *Electronchem. Solid-State Lett.*, 5(12):A279 – A282, 2002.

[143] I. Hodgkinson, Q. Wu, and S. Collett. Dispersion equations for vacuum-deposited tilted-columnar biaxial media. *Appl. Opt.*, 40:452 – 457, 2001.

[144] G. Beydaghyan, K. Kaminska, T. Brown, and K. Robbie. Enhanced birefringence in vacuum evaporated silicon thin films. *Appl. Opt.*, 43:5343 – 5349, 2004.

[145] A. van Popta, J. Sit, and M. Brett. Optical properties of porous helical thin films. *Appl. Opt.*, 43:3632 – 3639, 2004.

[146] M. Taschuk, J. Sorge, J. Steele, and M. Brett. Ion-beam assisted glancing angle deposition for relative humidity sensors. *IEEE Sens. J.*, 8:1521 – 1522, 2008.

[147] A. Wu, M. Seto, and M. Brett. Capacitive humidity sensors with novel microstructures. *Sens. Mater.*, 11(8):493 – 505, 1999.

[148] A. Wu and M. Brett. Sensing humidity using nanostructured sio posts: mechanism and optimization. *Sens. Mater.*, 13(7):399 – 431, 2001.

[149] K. Harris, K. Westra, and M. Brett. Fabrication of perforated thin films with helical and chevron pore shapes. *Electrochem. Solid-State Lett.*, 4(6):C39 – C42, 2001.

[150] K. D. Harris, A. Huizinga, and M. J. Brett. High-speed porous thin film humidity sensors. *Electrochem. Solid-State Lett.*, 5:H27 – H29, 2002.

[151] J.J. Steele, G.A. Fitzpatrick, and M.J. Brett. Capacitive humidity sensors with high sensitivity and subsecond response times. *IEEE Sens. J.*, 7(6):955–956, June 2007.

[152] J. Steele, M. Taschuk, and M. Brett. Response time of nanostructured relative humidity sensors. *Sensors and Actuators B*, 140:610 – 615, 2009.

[153] M. Taschuk, J. Steele, A. van Popta, and M. Brett. Photocatalytic regeneration of interdigitated capacitor relative humidity sensors fabricated by glancing angle deposition. *Sensors and Actuators B*, 134:666 – 671, 2008.

[154] D. Smetaniuk, M. Taschuk, and M. Brett. Photocatalytic titanium dioxide nanostructures for self-regenerating relative humidity sensors. *IEEE Sens. J.*, 11(8):1713 – 1719, 2011.

[155] M. Kupsta, M. Taschuk, M. Brett, and J. Sit. Reactive ion etching of columnar nanostructured tio2 thin films for modified relative humidity sensor response time. *IEEE Sens. J.*, 9(12):1979 – 1986, 2009.

[156] John J. Steele, Andy C. van Popta, Matthew M. Hawkeye, Jeremy C. Sit, and Michael J. Brett. Nanostructured gradient index optical filter for high-speed humidity sensing. *Sensors and Actuators B*, 120(1):213–219, December 2006.

[157] D-H. Chang, Y. Park, and C. Hwangbo. Optical humidity sensor using a narrow band-pass filter prepared by glancing angle deposition. *J. Korean Physical Society*, 53(5):2700 – 2704, 2008.

[158] Y. Liu, J. Shi, F. Zhang, H. Liang, J. Xu, A. Lakhtakia, S. Fonash, and T. Huang. High-speed optical humidity sensors based on chiral sculptured thin films. *Sensors and Actuators B*, 156:593 – 598, 2011.

[159] J. Steele. *Nanostructured thin films for humidity sensing*. PhD thesis, University of Alberta, 2007.

[160] Lewis Greenspan. Humidity fixed points of binary saturated aqueous solutions. *J. Res. Nation. Bur. Stand. A*, 81(1):89–96, January-February 1977.

[161] J. Rouquerol, F. Rouquerol, and K. Sing. *Adsorption by Powders and Amorphous Solids*, chapter Assessment of Mesoporosity, page 193. Academic Press, 1998.

[162] K. Krause, M. Thommes, and M. Brett. Pore analysis of obliquely deposited nanostructures by krypton gas adsorption at 87 k. *Microporous and Mesoporous Materials*, 143:166 – 173, 2011.

[163] P. Van Gerwen, W. Laureyn, W. Laureys, G. Huyberechts, M. Op De Beeck, K. Baert, J. Suls, W. Sansen, P. Jacobs, L. Hermans, and R. Mertens. Nanoscaled interdigitated electrode arrays for biochemical sensors. *Sens. Actuators B*, Vol. 1998:73 – 80, 1998.

[164] R. Igreja, C.J. Dias. Analytical evaluation of the interdigital electrodes capacitance for a multi-layered structure. *Sens. Actuators A*, 112:291 – 301, 2004.

[165] A. Kummer and A. Hierlemann. Configurable electrodes for capacitive-type sensors and chemical sensors. *IEEE Sens. J.*, 6(1):3 – 10, 2006.

[166] M Abramowitz and I. Stegun. *Handbook of Mathematical Funtions with Formulas, Graphs and Mathematical Tables*. U.S. Department of Commerce, 1972.

[167] P. Hrudey and K. Westra and M. Brett. Highly Ordered Organic Alq3 Chiral Luminescent This Films Fabricated by Glancing-Angle Deposition. *Ad. Mat.*, 18:224 – 228, 2006.

[168] A. Beaudry, R. Tucker, J. LaForge, M. Taschuk, and M. Brett. Indium tin oxide nanowhisker morphology control by vapourliquidsolid glancing angle deposition. *Nanotechnology*, 23:105608, 2012.

[169] M. Bettge, S. MacLeod, S. Burdin, J-G Wen, D. Abraham, I. Petrov, and E. Sammann. Low-temperature vapourliquidsolid (vls) growth of vertically aligned silicon oxide nanowires using concurrent ion bombardment. *Nanotechnology*, 20:115607, 2009.

Appendix A

Argon Flux Calculations

A.1 Calculation of Argon Source Position

As stated in Chapter 2, the argon source is positioned $20\ \mathrm{cm}$ from the substrate holder and has a $3\ \mathrm{cm}$ diameter output aperture. To calculate the source effective source position, d_0, similar triangles are used which describe the geometry (Fig. A.1). Fig. A.1a represents the actual geometry with the top side representing the three sigma value of the Gaussian fit of the beam profile. Fig. A.1b is a reduced, similar triangle which is obtained by subtracting the aperture dimension from the three sigma value. An expression for d_0 is given in Eq. A.1.

$$d_0 = 200 + \delta. \tag{A.1}$$

From Fig. A.1 and Eq. A.1, an expression to find δ can be obtained.

$$\frac{15}{\delta} = \frac{85.2}{200}. \tag{A.2}$$

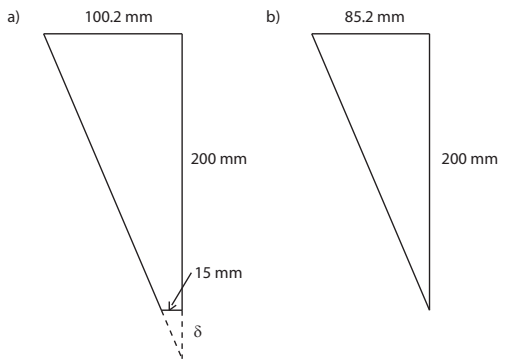

Figure A.1. *Geometry of the Ar-assisted setup, used to calculate the effective argon source position.*

From this, a value of 35 mm is obtained for δ, and a value of 235 mm is obtained for d_0.

A.2 Calculation of Peak Argon Flux

First, the total argon dose is calculated with the deposition time and beam current.

$$Argon\ dose = 35\ \mathrm{min} \cdot 60\ \mathrm{s/min} \cdot 5 \times 10^{-3}\ \mathrm{C/s} = 10.5\ \mathrm{C}. \tag{A.3}$$

Next, the total volume reduction and argon dose can be used to find the thickness reduction per argon flux.

$$\frac{Thickness\ reduction}{Argon\ dose} = \frac{1.5 \times 10^6\ \mathrm{nm \cdot mm^2}}{10.5\ \mathrm{C}} = \frac{1.5 \times 10^6\ \mathrm{nm}}{10.5\ \mathrm{C/mm^2}} = 1.4 \times 10^5\ \mathrm{nm/(C/mm^2)}. \tag{A.4}$$

Now, this result is divided by the thickness reduction taken from Fig. 2.4 and deposition time to convert back to flux.

$$Peak\ argon\ flux = \frac{215\ \mathrm{nm}}{1.4 \times 10^5\ \mathrm{nm/(C/mm^2)} \cdot 35\ \mathrm{min} \cdot 60\ \mathrm{s/min}} = 0.70\ \mathrm{A/m^2} \tag{A.5}$$

Appendix B

Surface Area Adsorption Isotherms

B.1 Surface Area Adsorption Isotherms

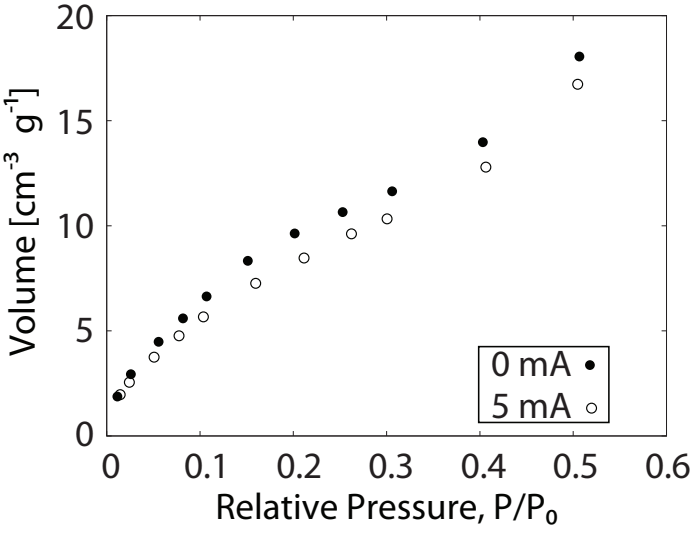

Figure B.1. *Adsorption isotherms of calcium fluoride films grown unassisted and with 5 mA Ar-assistance.*

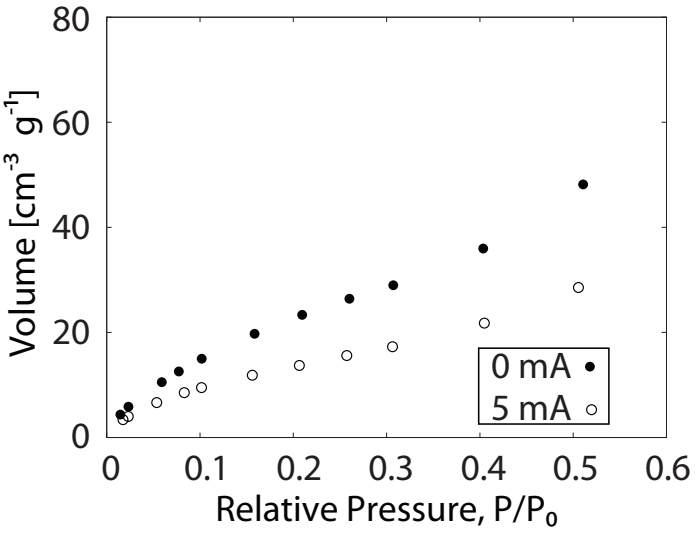

Figure B.2. *Adsorption isotherms of magnesium fluoride films grown unassisted and with 5 mA Ar-assistance.*

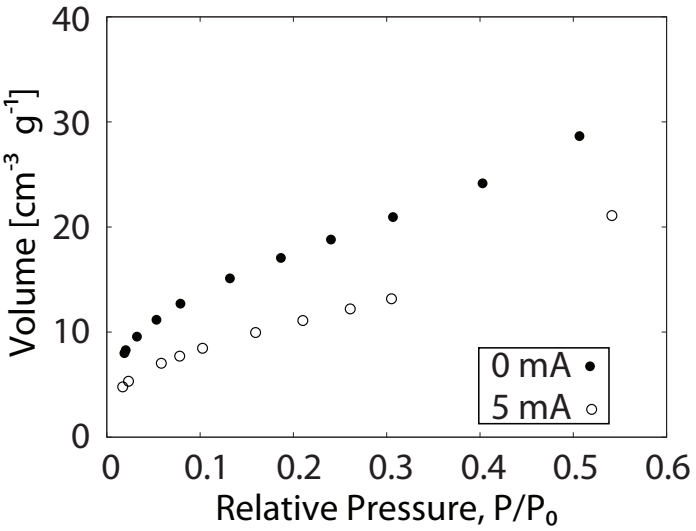

Figure B.3. *Adsorption isotherms of niobium oxide films grown unassisted and with 5 mA Ar-assistance.*

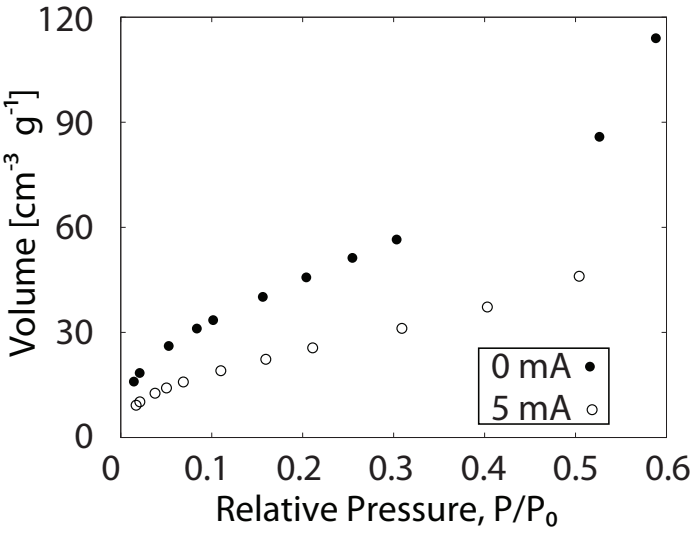

Figure B.4. *Adsorption isotherms of silicon monoxide films grown unassisted and with 5 mA Ar-assistance.*

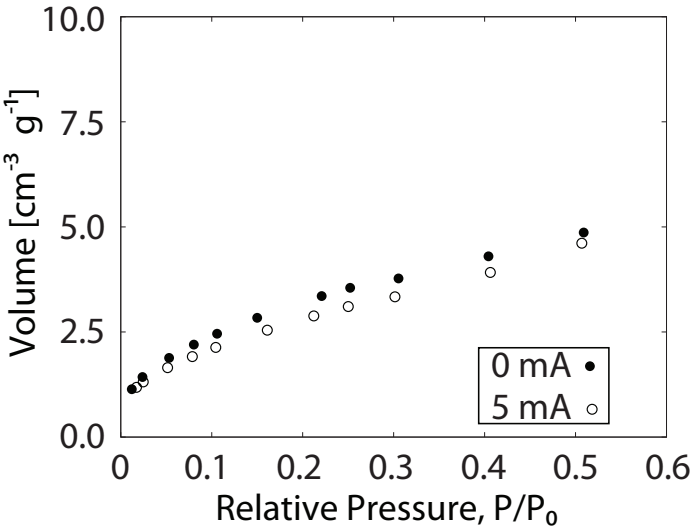

Figure B.5. *Adsorption isotherms of tin oxide films grown unassisted and with 5 mA Ar-assistance.*

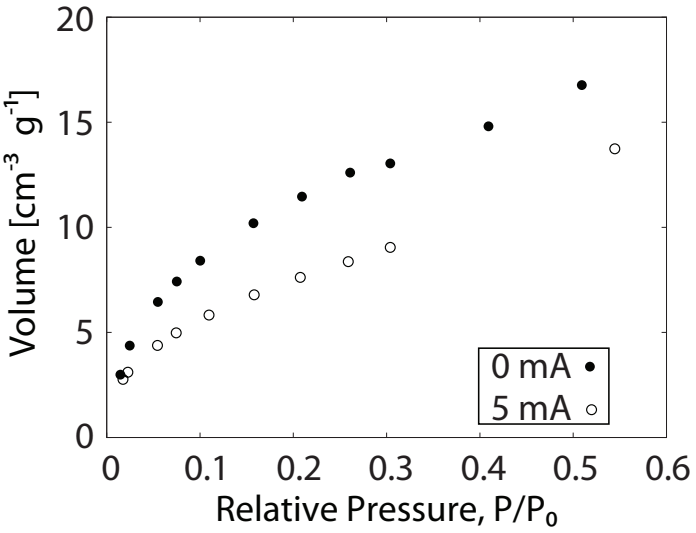

Figure B.6. *Adsorption isotherms of tantalum oxide films grown unassisted and with 5 mA Ar-assistance.*

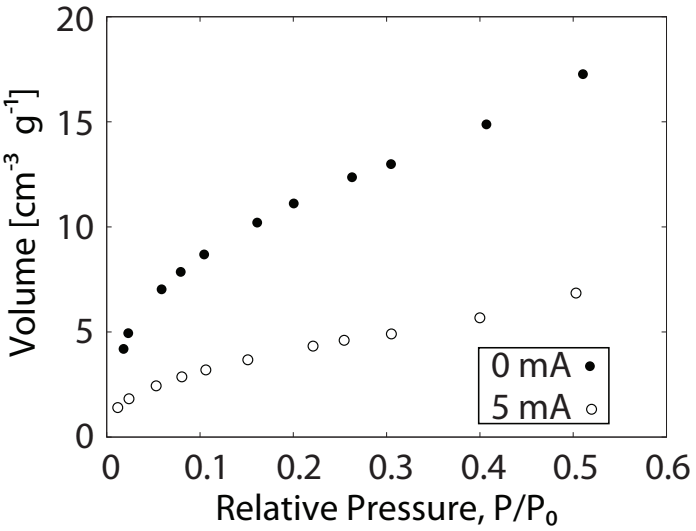

Figure B.7. *Adsorption isotherms of yttrium oxide films grown unassisted and with 5 mA Ar-assistance.*

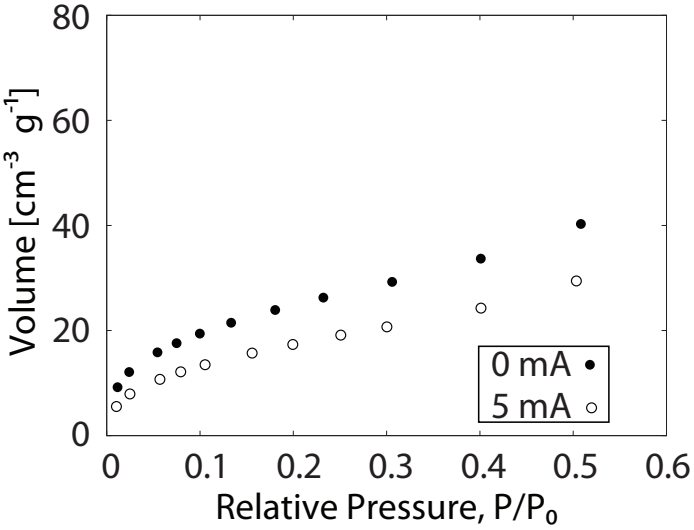

Figure B.8. *Adsorption isotherms of zirconium oxide films grown unassisted and with 5 mA Ar-assistance.*

Appendix C

SEM Images of Slanted Post GLAD Films

C.1 SEM Images of Slanted Post GLAD Films

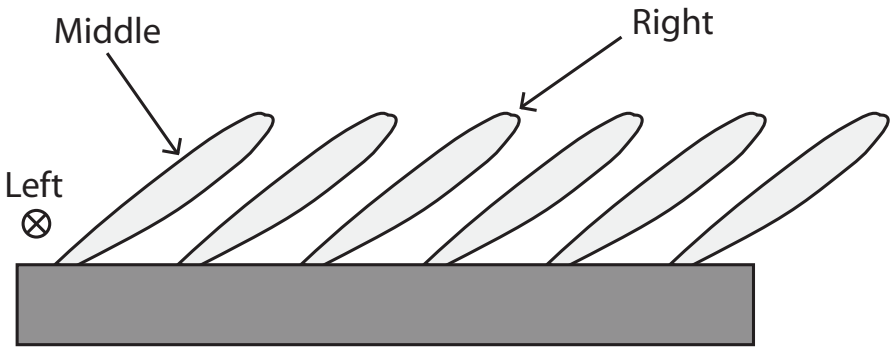

Figure C.1. *SEM imaging directions for the SEM images presented in this appendix.*

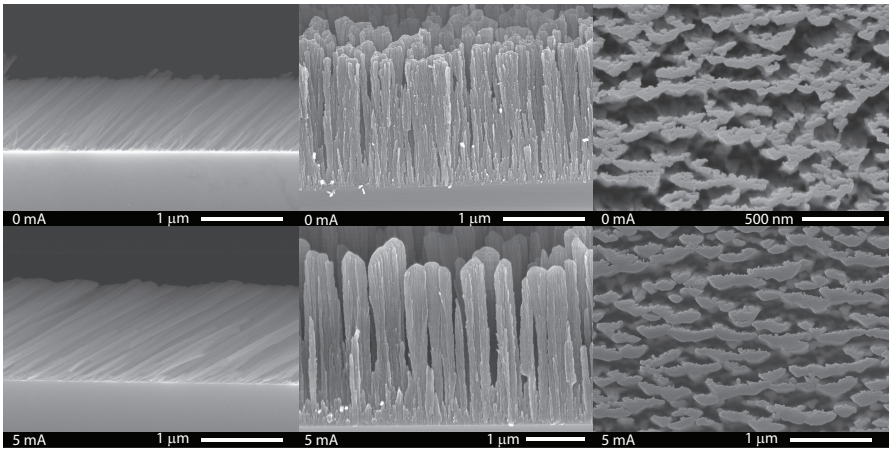

Figure C.2. *SEM images of aluminum oxide slanted post GLAD films grown unassisted (Top) and with 5 mA Ar-assistance (Bottom). SEM imaging directions are shown in Fig. C.1.*

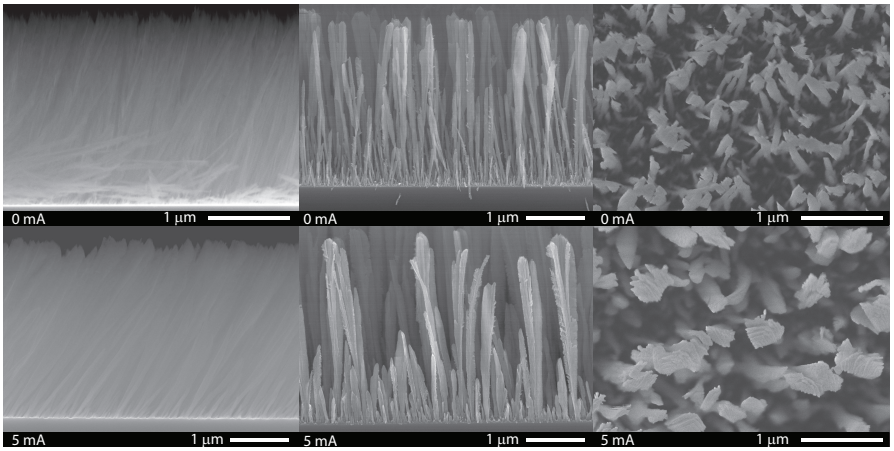

Figure C.3. *SEM images of calcium fluoride slanted post GLAD films grown unassisted (Top) and with 5 mA Ar-assistance (Bottom). SEM imaging directions are shown in Fig. C.1.*

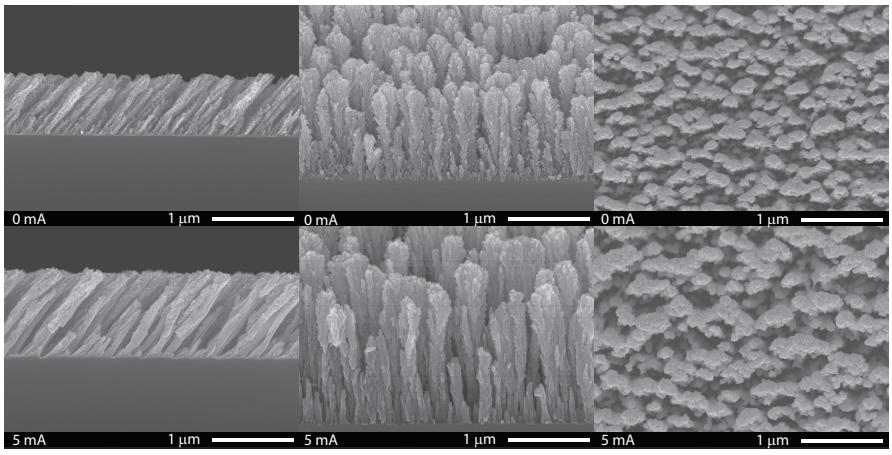

Figure C.4. *SEM images of indium tin oxide slanted post GLAD films grown unassisted (Top) and with 5 mA Ar-assistance (Bottom). SEM imaging directions are shown in Fig. C.1.*

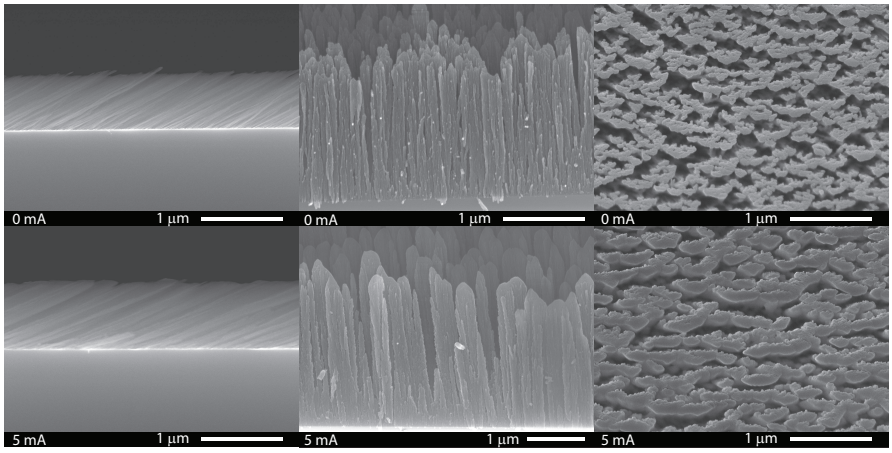

Figure C.5. *SEM images of magnesium fluoride slanted post GLAD films grown unassisted (Top) and with 5 mA Ar-assistance (Bottom). SEM imaging directions are shown in Fig. C.1.*

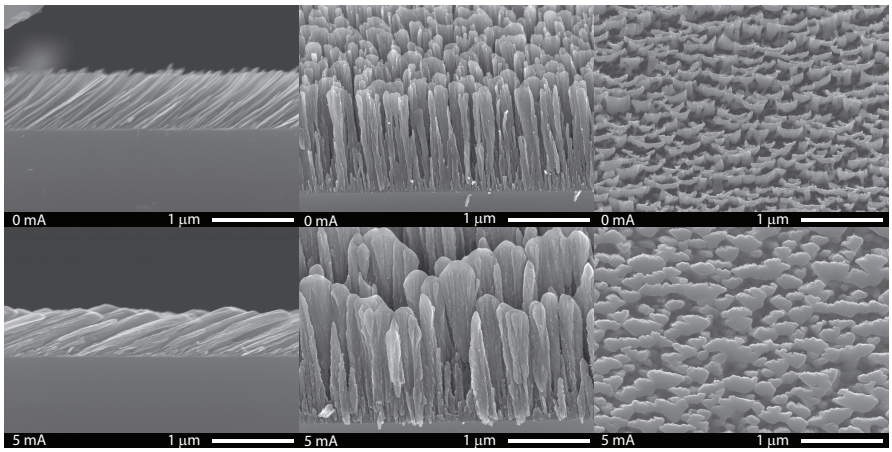

Figure C.6. *SEM images of niobium oxide slanted post GLAD films grown unassisted (Top) and with 5 mA Ar-assistance (Bottom). SEM imaging directions are shown in Fig. C.1.*

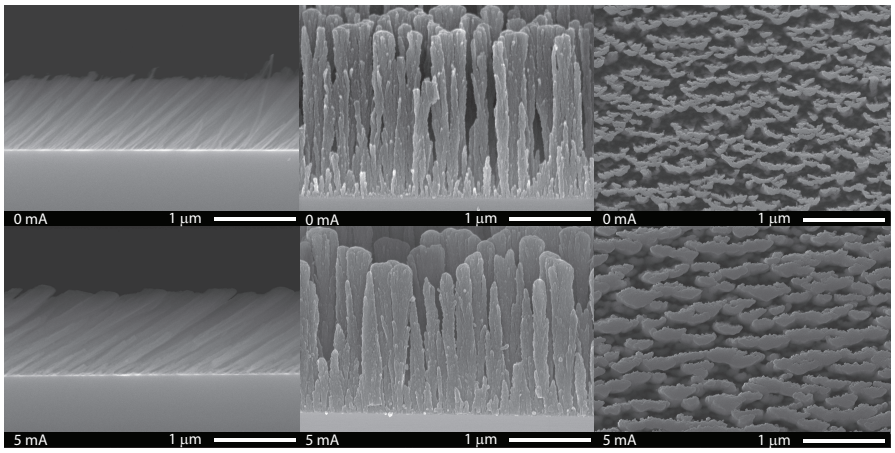

Figure C.7. *SEM images of silicon monoxide slanted post GLAD films grown unassisted (Top) and with 5 mA Ar-assistance (Bottom). SEM imaging directions are shown in Fig. C.1.*

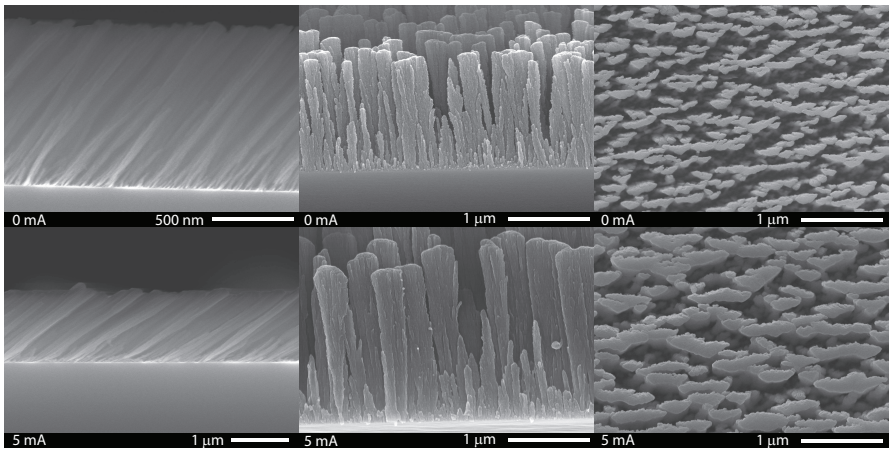

Figure C.8. *SEM images of silicon dioxide slanted post GLAD films grown unassisted (Top) and with 5 mA Ar-assistance (Bottom). SEM imaging directions are shown in Fig. C.1.*

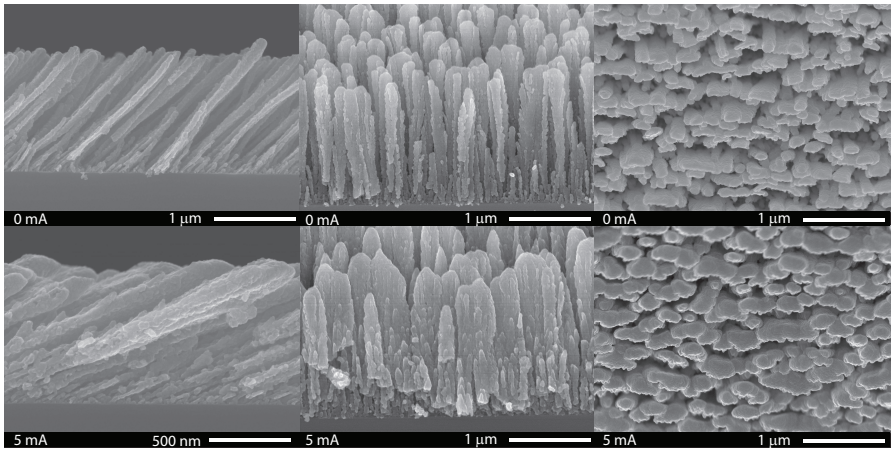

Figure C.9. *SEM images of tin oxide slanted post GLAD films grown unassisted (Top) and with 5 mA Ar-assistance (Bottom). SEM imaging directions are shown in Fig. C.1.*

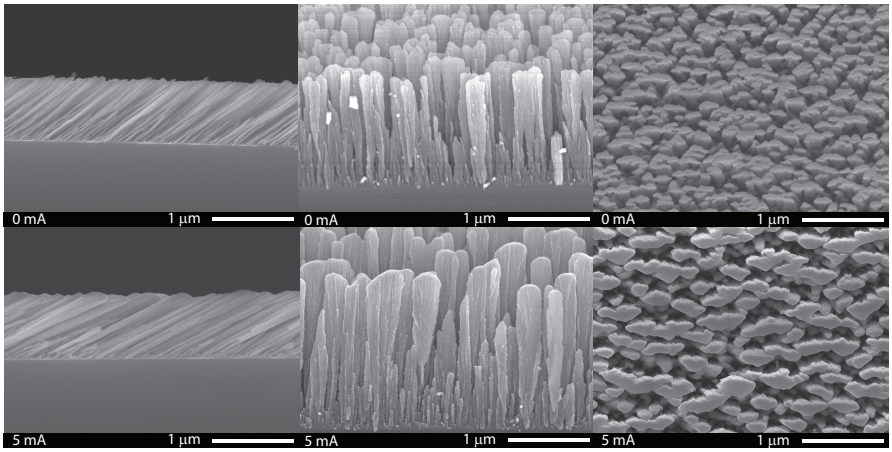

Figure C.10. *SEM images of tantalum oxide slanted post GLAD films grown unassisted (Top) and with 5 mA Ar-assistance (Bottom). SEM imaging directions are shown in Fig. C.1.*

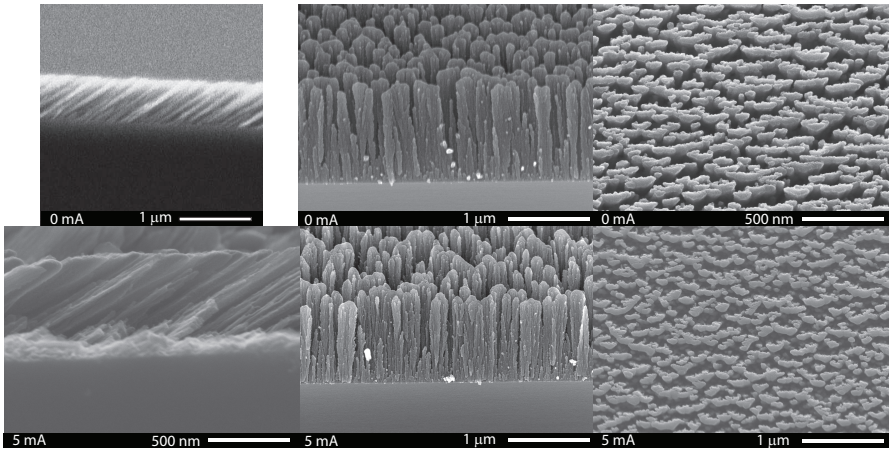

Figure C.11. *SEM images of titanium dioxide slanted post GLAD films grown unassisted (Top) and with 5 mA Ar-assistance (Bottom). SEM imaging directions are shown in Fig. C.1.*

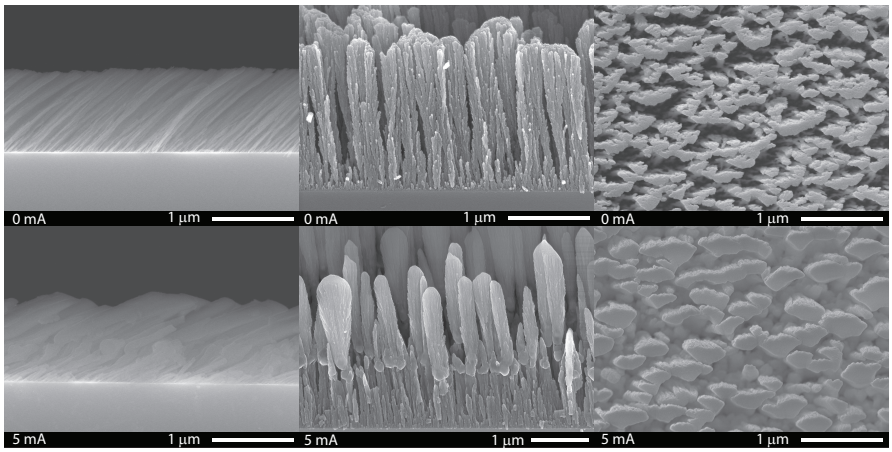

Figure C.12. *SEM images of yttrium oxide slanted post GLAD films grown unassisted (Top) and with 5 mA Ar-assistance (Bottom). SEM imaging directions are shown in Fig. C.1.*

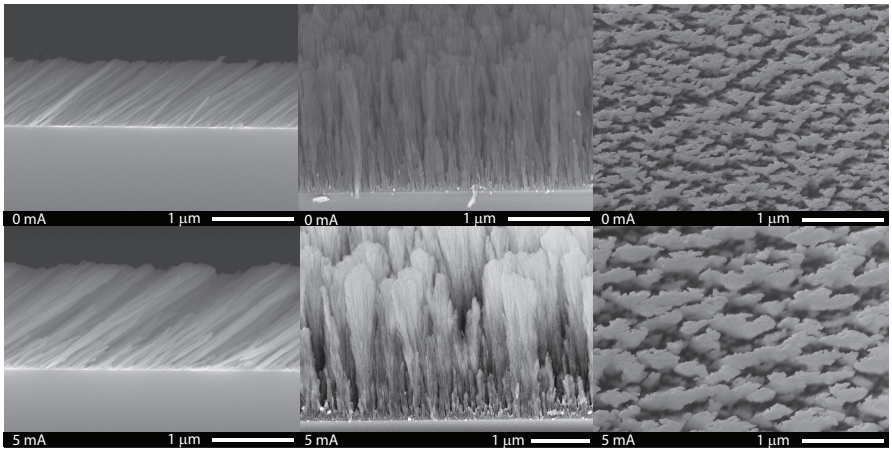

Figure C.13. *SEM images of zirconium oxide slanted post GLAD films grown unassisted (Top) and with 5 mA Ar-assistance (Bottom). SEM imaging directions are shown in Fig. C.1.*